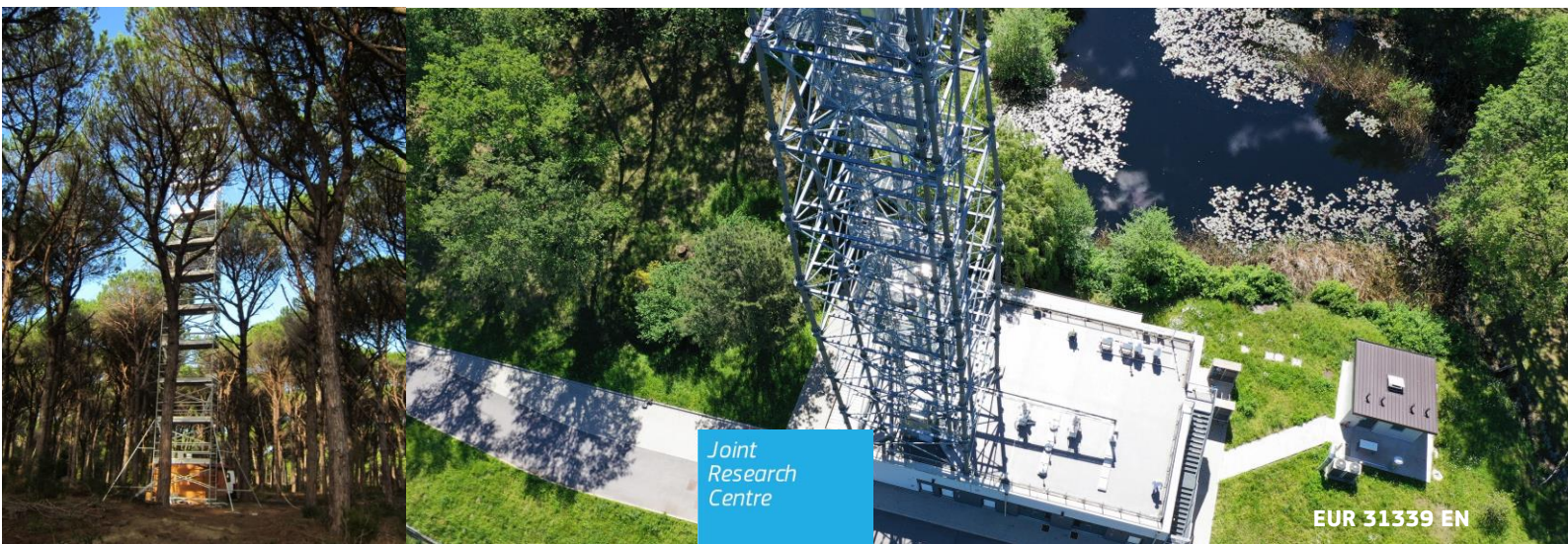European
Commission

JRC TECHNICAL REPORT

The European Commission Atmospheric Observatory

2021 Report

Putaud, J.P., Arriga, N., Borowiak, A., Cavalli, F., Dell'Acqua, A., Duerr, M., Jensen, N.R., Lagler, F., Manca, G., Martins Dos Santos, S., Matteucci, M., Passarella, R., Pedroni, V.

2023

Joint
Research
Centre

EUR 31339 EN

How to cite this report: Putaud, J.P., Arriga, N., Borowiak, A., Cavalli, F., Dell'Acqua, A., Duerr, M., Jensen, N.R., Lagler, F., Manca, G., Martins Dos Santos, S., Matteucci, M., Passarella, R., Pedroni, V., *The European Commission Atmospheric Observatory: 2021 report*, Publications Office of the European Union, Luxembourg, 2023 JRC131651.

Contents

Abstract

The mission of the European Commission Atmospheric Observatory is to benchmark the impact of European policies and international conventions on air pollution and climate forcing at critical locations.

At the JRC-Ispra site, located in one of the most polluted area of Europe, we measure greenhouse gas concentrations (CO_2, CH_4), radon (^{222}Rn) activity, short-lived gaseous and particulate pollutant concentrations (CO, SO_2, NO, NO_2, O_3, NMHCs, NH_3, $PM_{2.5}$ and its main ionic and carbonaceous constituents), atmospheric particle micro-physical characteristics (number concentration and size distribution) and optical properties (light scattering absorption and extinction coefficients in-situ, light scattering and extinction vertical profiles remotely), and eutrophying and acidifying species (sulphate, nitrate, ammonium) wet deposition.

Vegetation ⇆ atmosphere exchanges (CO_2, H_2O and heat) are measured at our Mediterranean Forest Flux Station of San Rossore (climate sensitive ecosystem), backed up by meteorological and pedological measurements.

Several COVID-19 epidemic waves affected human mobility in 2021, but no effect on CO_2 concentrations could be detected. The low NO, NO_2, SO_2, PM and high O_3 levels we observed cannot simply be attributed to COVID impacts before a direct link is demonstrated.

Preliminary data suggest that the Mediterranean pine tree forest was a larger net sink for CO_2 in 2021 compared to previous years.

All data can be downloaded from the JRC Data Catalogue or open data banks.

Fig. 1. Location of the Atmospheric Observatory sites in Ispra and San Rossore (top), and of the temporary EMEP-GAW site, the former greenhouse gas laboratory, and the new Atmospheric Observatory, built on the spot of the historical EMEP-GAW station on the JRC-Ispra site (bottom). The temporary site and the GHG laboratory are no longer operated since July 2017 and 2018, respectively.
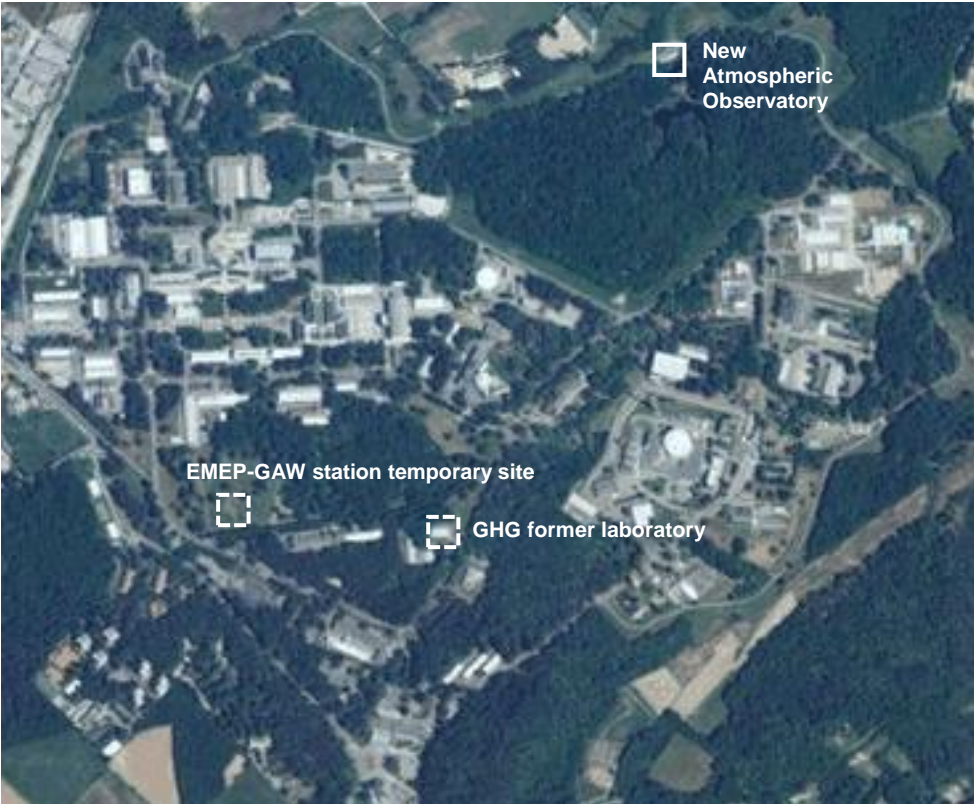
Source: background from Google Earth

1 Introduction

The mission of the European Commission Atmospheric Observatory (formerly called ABC-IS) is to measure changes in atmospheric variables to obtain data that are essential for the conception, development, implementation and monitoring of the impact of European policies and International conventions on air pollution and climate change. Measurements include greenhouse gas concentrations, forest ⇆ atmosphere fluxes, and concentrations of pollutants in the gas phase, particulate matter and precipitations, as well as aerosol micro-physical and optical properties. Atmospheric measurements are performed at the JRC-Ispra site (Fig. 1), and forest ⇆ atmosphere fluxes are performed at the typical Mediterranean site of San Rossore. The scope of the Observatory is to establish real world interactions between air pollution, climate change and the biosphere, highlighting possible trade-offs and synergies between air pollution and climate change policies. Possible interactions include the role of pollutants in climate forcing, the impact of climate change and air pollution on CO_2 uptake by vegetation, the effect of biogenic emission on air pollution and climate forcing, etc…

The Observatory is part of the spread European research infrastructures ICOS (Integrated Carbon Observation System) and ACTRIS (Aerosol, Clouds, and Trace Gases Research Infrastrucuture). Measurements are performed under international monitoring programs like EMEP (Co-operative program for monitoring and evaluation of the long range transmission of air pollutants in Europe of the UN-ECE *Convention on Long-Range Transboundary Air Pollution* CLRTAP) and GAW (the Global Atmosphere Watch program of the World Meteorological Organization). The Observatory infrastructure has also been used in competitive projects (e.g. ACTRIS-2, InGOS).

The participation of the Observatory in international networks involves the organisation of inter-laboratory comparisons and the development of standard methods within the European Reference Laboratory for Air Pollution (ERLAP) of the JRC Air and Climate Unit.

We report here about the annual activities of the 3 components of the Atmospheric Observatory, i.e., greenhouse gas concentration monitoring from the tall tower in Ispra (Section 3), air pollution characterisation (at surface level and by remote sensing) at the same site in Ispra (Section 4), and forest ⇆ atmosphere exchange flux observation at the Mediterranean forest in San Rossore (Section 5). The data obtained in 2021 are presented in the context of data obtained during previous years.

2 Quality management system

The European Commission Atmospheric Observatory is a research infrastructure operated by JRC's *Directorate for Energy, Transport and Climate*.

We achieved ISO 9001 certification in 2010 and re-certification in 2013, in 2016 and in 2019, all done by external audits. The certification is valid also for the year 2021 (ISO 9001 is mainly about project management).

In addition to ISO 9001, JRC Ispra also achieved in 2010 the ISO 14001 certificate (ISO 14001 is mainly about environmental issues). In 2017, an external audit for re-certification took successfully place at JRC-Ispra (achieving again the ISO 14001 (EMAS) certificate): The certificate is also valid for the year 2021.

Finally, JRC Ispra is also certified with OHSAS-18001/ISO-45001 since 2018 (mainly about health and safety). In 2021, an external audit for re-certification took successfully place at JRC-Ispra (ISO 45001).

Quality management information and documentation relative to the Air and Climate Unit (JRC-C5) can be retrieved from the QMS (Quality management system) space accessible to JRC staff only in the seven documents listed here (latest versions):

QMS_DIR_C_C5_Quality_Unit_Management_Manual_v15_0_in_ares.pdf
QMS_C5_MANPROJ_PROJ_Laboratory_Management_v14_0_in_ares.pdf
QMS_C5_MANPROJ_PROJ_Model_Management_v14_0_in_ares.pdf
QMS_C5_MANPROJ_PROJ_Informatics_Management_v14_0_in_ares.pdf
QMS_C5_MANPROJ_PROJ_Knowledge_Management_v14_0_in_ares.pdf
QMS_C5_MANPROJ_PROJ_Review_Verification_Validation_Approval_v10_0_in_ares.pdf
QMS_C5_MANPROJ_PROJ_Administration_Implementation_v9_0_in_ares.pdf

More specifically, the QMS for the EC Atmospheric Observatory includes standard operational procedures (SOP's); information about calibrations, standards used and maintenance; instrument lifecycle sheets and log-books; manuals for the instruments; *etc*.

Further quality assurance and quality control information can be found in the Section. 4.3 of this report.

Fig. 2. The JRC Atmospheric Observatory: the 100m tower (left) and the laboratory equipment (right) for GHG concentration measurements (Building 77r).

Source: JRC, 2021

3 Greenhouse gas concentration monitoring at the JRC-Ispra site

3.1 Location

JRC is operating a greenhouse gas (GHG) monitoring station at Ispra site since 2007. This station is currently the only low altitude measurement site for GHGs near the Po Valley. The unique location of the station at the South-Eastern border of Lake Maggiore in a semi-rural area at the North-Western edge of the Po Valley allows sampling of highly polluted air masses from the Po Valley during meteorological conditions with southerly flow, contrasted by situations with northerly winds bringing relatively clean air to the site. A high-resolution modelling study analysed in detail the sensitivity of the atmospheric concentrations at the monitoring station [*Bergamaschi and Brunner, 2015*]. The sensitivity usually shows a significant diurnal cycle, during night dominated by the area 40-60 km around the station, while daytime footprints are much larger, typically dominated by distances of more than 60 km. During summer daytime, the radius R_{50} (at which the cumulative surface sensitivity reaches 50% of the total sensitivity) is about 187 km on average. Furthermore, the diurnal cycle in local wind direction due to the regional mountain - lake/valley wind system leads to a significant diurnal cycle of the sensitivity (north-west vs. south-east), especially during summertime.

The main cities around the station are Varese, 20 km east of the station, Novara, 40 km south, Gallarate - Busto Arsizio, about 20 km southeast, and Milan, 60 km south-east of the station. The JRC GHG station has been setup in 2007 in building 5 (Fig. 1) of the JRC Ispra site premises (45.807°N, 8.631°E, 223 m asl) and it has been operated at that location continuously until beginning of July 2018. This station has been discontinued afterwards. In 2016 a new GHG station inside the JRC premises (building 77r, 45.8147°N, 8.6360°E, 210 m asl) has been set-up. The new station includes a 100m tower on top of the station building (Fig. 2), with platforms every 20 m. At the end of 2016 the new station has been equipped with a GHG instrument and sampling system with multiple sampling lines at 40, 60, and 100m.

3.2 Measurement programme

The new GHG station is a component of the European Commission Atmospheric Observatory together with the JRC-Ispra EMEP-GAW station, which started in 1985 (Putaud et al., 2022), and the flux measurement tower in the forest of San Rossore. Moreover, the station is contributing to the Integrated Carbon Observation System (ICOS) research infrastructure (https://www.icos-cp.eu/) and it has been labelled as ICOS class-2 atmosphere station on 30/11/2018.

Continuous measurement of CO_2, CH_4 and meteorological variables are performed in compliance with ICOS guidelines (which includes rigorous standardization of instrumentation, sampling, calibration, QA/QC and centralized data processing). The GHG and meteorological observations are complemented by measurements of carbon monoxide (CO), which serves as tracer for fossil fuel CO_2 emissions and radon (^{222}Rn), which serves as tracer for atmospheric transport. Moreover, continuous measurement of ammonia (NH_3), to be used as tracer for methane emissions, started in March 2020.

Fig. 3. Sampling, conditioning and distribution system diagram for the GHG measurements at the Atmospheric Observatory, Ispra.
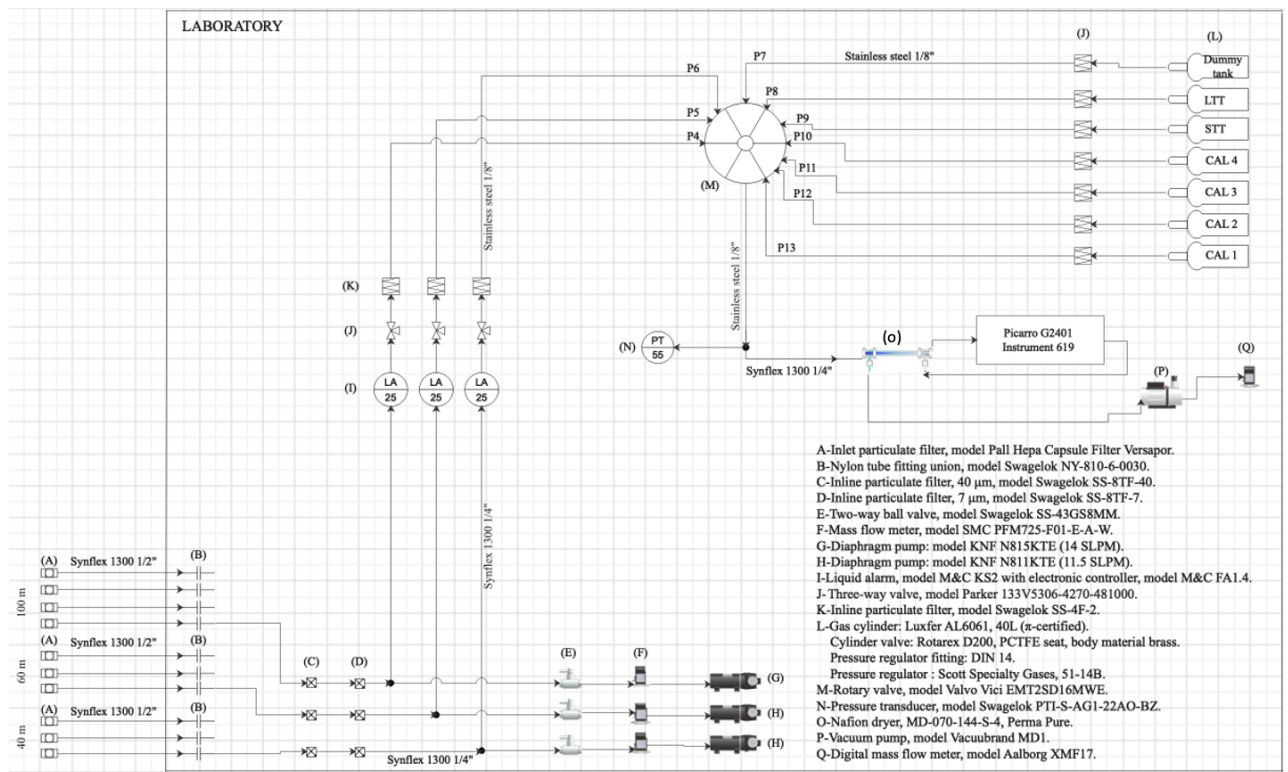
Source: JRC, 2021

Table 1. Measurement sequence of the GHG analyser Picarro G2401. This cycle is repeated continuously every hour.

Sampling Level	Sampling duration (minutes)
100 m	15 (first 5 min rejected)
60 m	15 (first 5 min rejected)
100 m	15 (first 5 min rejected)
40 m	15 (first 5 min rejected)

Source: JRC, 2021

3.3 Instrumentation at the Atmospheric Observatory (Building 77r)

3.3.1 Sampling

Air samples for GHG and CO measurement are collected at different levels on the tower (40m, 60m, 100m) using ½" Synflex tubes at a flow rate of ~10 L min^{-1}. Each sampling line is provided with a KNF diaphragm pump (KNF N811 KTE or KNF N815 KTE) and three different particulate filters: a Pall Hepa Capsule Versapor filter at the inlet, and two filters with nominal pore sizes of 40 µm and 7 µm (model Swagelok SS-8TF-40 and SS-8TF-7, respectively).

A small air flow (around 0.2 L min^{-1}) is diverted from the main line toward the Picarro G2401 instrument using a dedicated vacuum pump (model Vacuubrand, MD1) located downstream to the analyser. A liquid water alarm is in place to prevent any liquid water reaching the analyser. Water vapour in the air sample is partially removed through a Nafion membrane consisting of a Perma Pure tube (model MD-070-144-S-4) used in the "reflux mode" as shown on the figure 2. This drying setup does not require an additional pump for a Picarro G2401 as the Picarro downstream vacuum pump can be used for sampling through the Nafion and for the purge counter flow. The Nafion tube has been installed on 22 May 2020 (Fig. 3).

3.3.2 Analyses

3.3.2.1 Cavity Ring-Down Spectrometer Picarro G2401 *(S/N 2326-CFKADS2193)*

The GHG laboratory at the Atmospheric Observatory is equipped with a Picarro G2401 Cavity Ring-Down Spectrometer (CRDS) that measures concentrations of CO_2, CH_4, CO and H_2O with a time resolution of 5 seconds. Concentrations are measured at three levels on the tower: 40 m, 60 m and 100 m above ground level (fig. 2) following the ICOS technical specifications for class-2 atmosphere stations (https://box.lsce.ipsl.fr/index.php/s/uvnKhrEinB2Adw9?path=%2FSpecifications). A rotary valve, model Valco Vici EMT2SD16MWE, allows to select the tower level to be analysed.

The Picarro G2401 instrument directly controls this valve in order to sample the three levels sequentially within one hour. Measurement sequence is showed in Table 1.

3.3.2.2 Radon analyser ANSTO (custom built)

GHG observations are complemented by measurements of ^{222}Rn that started in December 2016. ^{222}Radon activity concentrations in Bq m^{-3} have been monitored semi-continuously (30 minute time integration) applying an ANSTO dual-flow loop two-filter detector (Zahorowski et al., 2004).

Air sample is taken from a separate inlet at 100 m above ground by using a blower (Becker, model SV 8.130/1-01). A 500 L decay tank is placed in the inlet line to allow for the decay of Thoron (^{220}Rn with a half-life of 55.6 s) before reaching the ^{222}Radon monitor. The ANSTO ^{222}Radon monitor has been calibrated once a month using a commercial passive ^{226}Radium source from Pylon Electronic Inc. (Canada) inside the calibration unit with an activity of 21.99 kBq, which corresponds to a ^{222}Radon delivery rate of 2.77 Bq min^{-1} . The lower detection limit is 0.02 Bq m^{-3} for a 30% precision (relative counting error). The total measurement uncertainty is estimated to be <5% for ambient ^{222}Radon activities at Ispra.

Fig. 4. Time series of continuous CO₂, CH₄ and CO ambient measurements at the Atmospheric Observatory, sampled at three different heights (40m, 60m, 100m), between December 2016 and December 2022. Concentrations are reported as hourly mean values of dry air mole fractions. Furthermore, CO₂, CH₄, and CO flask measurements from the background station Mace Head (MHD) on the West coast of Ireland are also included (Lan et al., 2022a and 2022b; Petron et al., 2021).
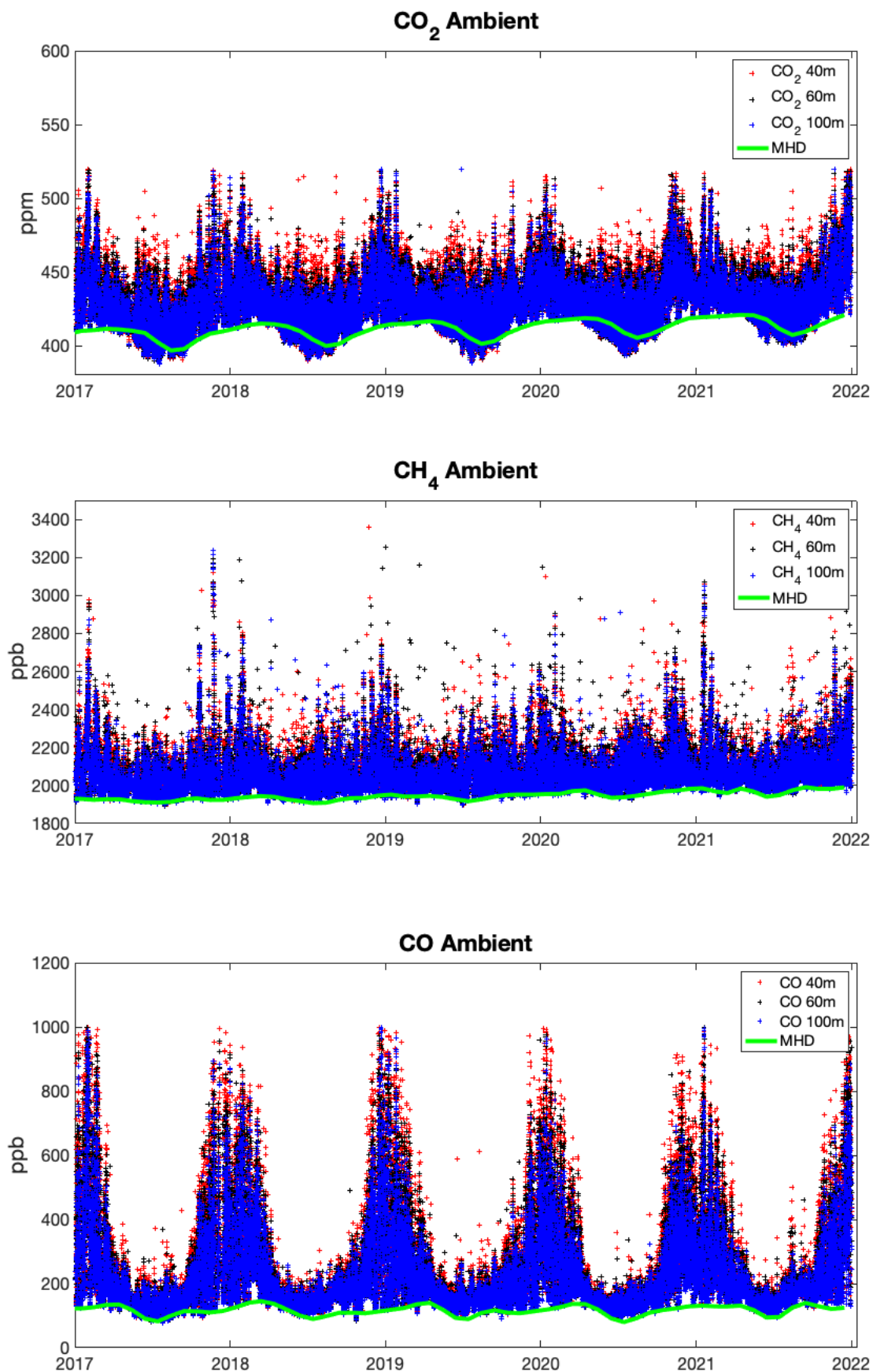
Source: JRC, 2022

3.4   Overview of measurement results

Fig. 4 shows the measurements of CH_4 and CO_2 at the Atmospheric Observatory (building 77r) at three different heights above ground (100m, 60m and 40m) between December 2016 and December 2021. Monthly mean baseline data from Mace Head station is also plotted to illustrate the Atlantic background mixing ratios.

Carbon dioxide concentrations show a typical seasonal pattern largely controlled by fossil fuel emissions and seasonal fluxes of carbon between the atmosphere and terrestrial ecosystems. During fall and winter seasons, when trees and plants begin to lose their leaves and decay, there is a net release of carbon dioxide into the atmosphere, mixing with emissions from anthropogenic sources. This allows concentrations to climb all winter, reaching a peak by early spring. During spring and summer months, plants absorb a substantial amount of carbon dioxide through photosynthesis, thus removing it from the atmosphere.

Atmospheric mixing ratios of methane do not show any evident seasonal variations. However, the time series shows a large variability mainly related to the methane emission from the local dairy cow farms.

Hourly values of carbon monoxide measured at 40m, 60m and 100m from December 2016 till December 2021 are showed in Fig. 4. CO has a large season variability with very high value in autumn-winter, and low values in spring-summer.

Fig. 5**Fig. 5** shows hourly mean [222]Radon activity concentrations measured in building 77r at 100m level between December 2016 and December 2021. [222]Radon activity concentrations show large diurnal and seasonal variations, mainly due to the diurnal and seasonal variations of the boundary layer height (Koffi et al., 2016). A decreasing trend of the diurnal and seasonal variability of radon concentration is evident. Some tests performed in September 2022 revealed a hardware issue with the high-voltage power supply of the photomultiplier tube making the detector less sensitive to changes in radon concentration.

Fig. 5. [222]Rn measurements at Atmospheric Observatory (Building 77r). The figure shows the time series of hourly mean [222]Radon activity, collected at 100m height, between December 2016 and November 2021.

Source: JRC, 2022

10
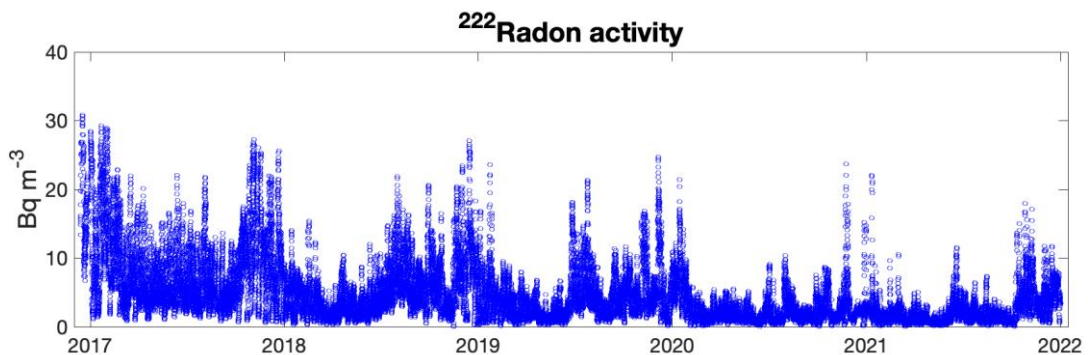
Fig. 6. Trends in atmospheric GHG concentrations at the Atmospheric Observatory. Top panel: CO_2; lower panel: CH_4. The figures show daily average values at 100m, using only daytime measurements (between 11:00 and 16:00 UTC). Solid red line: Fit to daily data based on NOAA fitting procedure (Thoning et al., 1989); dashed red line: trend derived from fitting procedure.
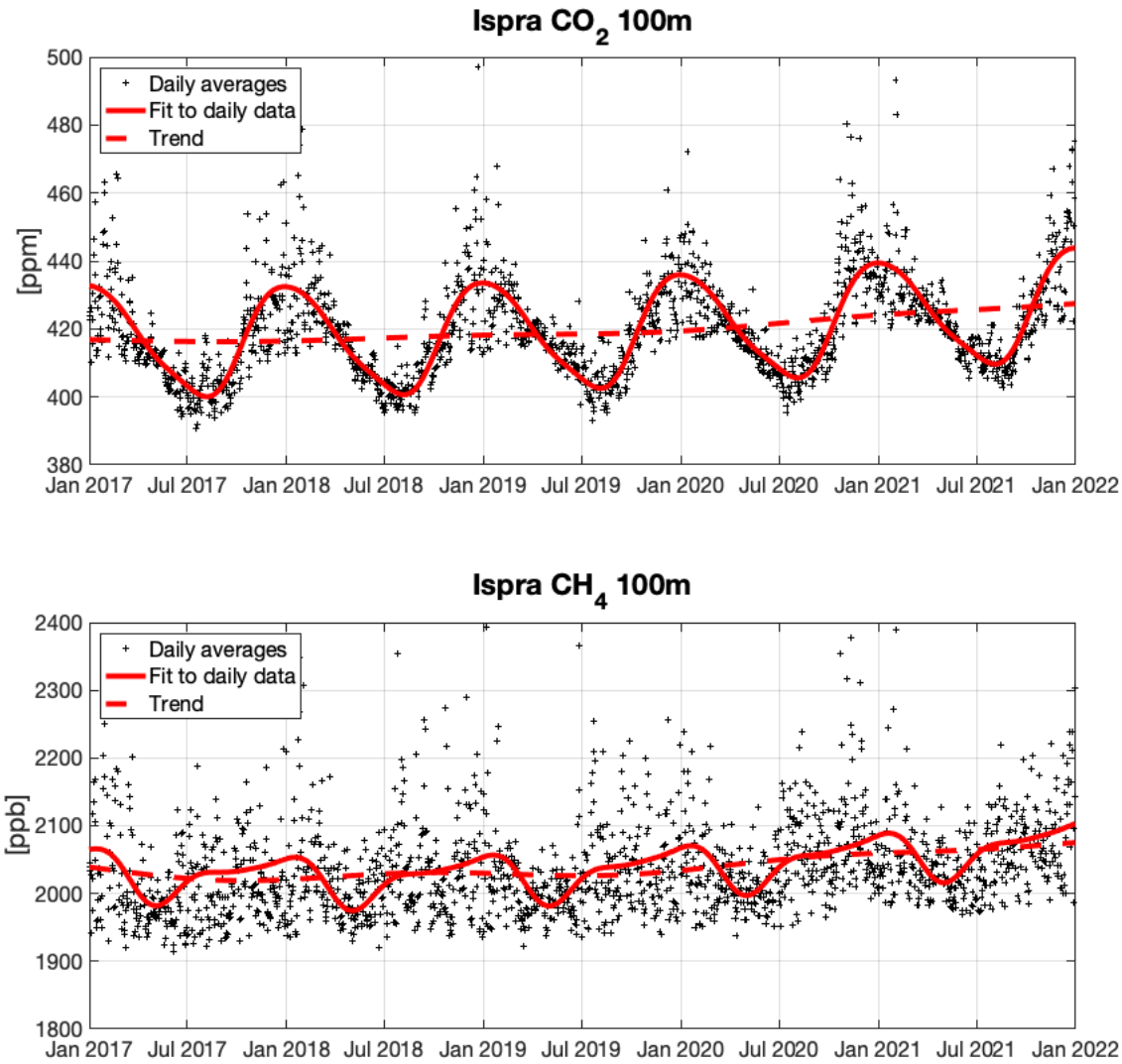
Source: JRC, 2022

Fig. 6 shows the time series of daily average CO_2 and CH_4 dry air mole fractions at 100m, using only daytime measurements (between 11:00 and 16:00 UTC). In order to further analyse the trends and seasonal variations we applied the NOAA fitting procedure (Thoning et al., 1989).

For CO_2, we derive an average trend of +2.11 ppm yr^{-1} between 2017 and 2021, compared to a global trend of +2.38 ppm yr^{-1} (https://www.esrl.noaa.gov/gmd/ccgg/trends/gl_gr.html).

For CH_4 we derive an average trend of +7.2 ppb yr^{-1} between 2017 and 2021, that is lower than the observed global CH_4 trend of +11.7 ppb yr^{-1} during the same period (www.esrl.noaa.gov/gmd/ccgg/trends_ch4/).

Fig. 7. Most recent map of the EMEP stations across Europe (2020) taken from the Chemical co-ordinating Centre ([CCC](#)).
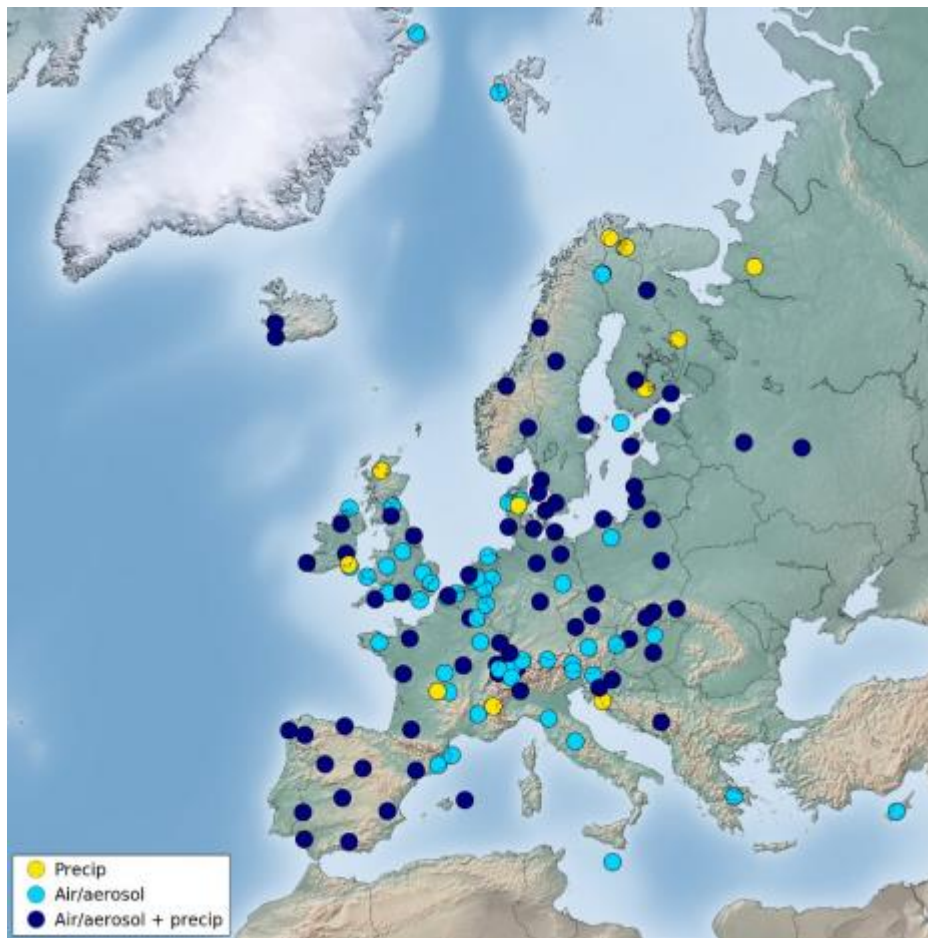
Source: EMEP-CCC [report 1/2022](#).

4 Short-lived atmospheric species at the JRC-Ispra site

4.1 Introduction

4.1.1 Location

Air pollution has been monitored since 1985 at the Atmospheric Observatory (45°48.881'N, 8°38.165'E, 209 m a.s.l.) located by the Northern fence of the JRC-Ispra site (see Fig. 1), situated in a semi-rural area at the NW edge of the Po valley in Italy. From the end of March 2013 until June 2017, the measurement of short-lived atmospheric species (Table 2) was performed at a provisional site (45°48.438'N, 8°37.582'E, 217 m a.s.l.), due to the reconstruction of the laboratory at the historical site (Fig. 1). Gaseous pollutant measurements actually continued at the provisional site until December 2017 for comparison.

The nearest cities are Varese (20 km east), Novara (40 km south), Gallarate – Busto Arsizio (about 20 km south-east) and the Milan conurbation (60 km south-east). Busy roads and highways link these urban centres. There are 7 industrial point sources located within 50 km of Ispra (all in the south-southeast sector) emitting between 300 and 2700 tons of CO_2 per day (industry.eea.europa.eu, 2019 data). The closest (5 km SE) also emits 1.4 t of CO per day. Others (located between 33 and 43 km S-SE) emit all together 3.2 tons of CO, 4.6 NO_2 equivalent tons of NO_x, and 5.2 tons of SO_2 per day.

4.1.2 Underpinning programmes

4.1.2.1 The EMEP programme (*http://www.emep.int/*)

Currently, about 50 countries and the European Community have ratified the Convention **CLRTAP**, whose EMEP is the monitoring and modelling supporting programme. Lists of participating institutions and monitoring stations (Fig. 7) can be found at: *http://www.nilu.no/projects/ccc/network/index.html*

The set-up and running of the JRC-Ispra EMEP station resulted from a proposal of the Directorate General for Environment of the European Commission in Brussels, in agreement with the Joint Research Centre, following the Council Resolution **N° 81/462/EEC**, article 9, to support the implementation of the EMEP programme.

The JRC-Ispra station has operated on a regular basis in the extended EMEP measurement programme since November 1985. Data are transmitted yearly to the EMEP Chemical Co-ordinating Centre (CCC) for data control and statistical evaluation, and available from the EBAS data bank (Emep Database, *http://ebas.nilu.no/*).

4.1.2.2. The GAW programme (*http://www.wmo.int/web/arep/gaw/gaw_home.html*)

WMO's Global Atmosphere Watch (GAW) was established in 1989 with the scope of providing information on the physico-chemical composition of the atmosphere. These data provide a basis to improve our understanding of both atmospheric changes and atmosphere-biosphere interactions. GAW is one of WMO's most important contributions to the study of environmental issues, with about 80 countries participating in GAW's measurement programme. Since December 1999, the JRC-Ispra station is also part of the GAW coordinated network of regional stations. Data contributing to the GAW programme are also available via EBAS.

4.1.2.3. The institutional programme (*http:/ec.europa.eu/jrc/en/research-topic/air-quality*)

Since 2002, the measurement programme of the air pollution monitoring station of JRC-Ispra has gradually been focused on short-lived climate forcers such as tropospheric ozone and aerosols and their precursors (Fig. 8). Concretely, more sensitive gas monitors were introduced, as well as a set of new measurements providing aerosol variables that are linked to radiative forcing. The observatory has contributed to the deliverable 202104 "COVID Impact on Air Pollutants" as listed in the 2021 JRC institutional project work plan ("Zero Air Pollution" Portfoglio, "Prov-MO" project, Deliverable 15).

The Atmospheric Observatory is also used for research and development purposes. Regarding particulate organic and elemental carbon, techniques developed by the Air and Climate unit in Ispra have been implemented and validated by international atmospheric research projects (EUSAAR, ACTRIS), recommended in the EMEP sampling and analytical procedure manual and adopted by the European Committee for Standardisation (CEN) as a standard method (EN16909:2017).

Fig. 8. Atmospheric short-lived species measurements performed at the JRC-Ispra atmospheric observatory since 1985.

Source: JRC, 2022
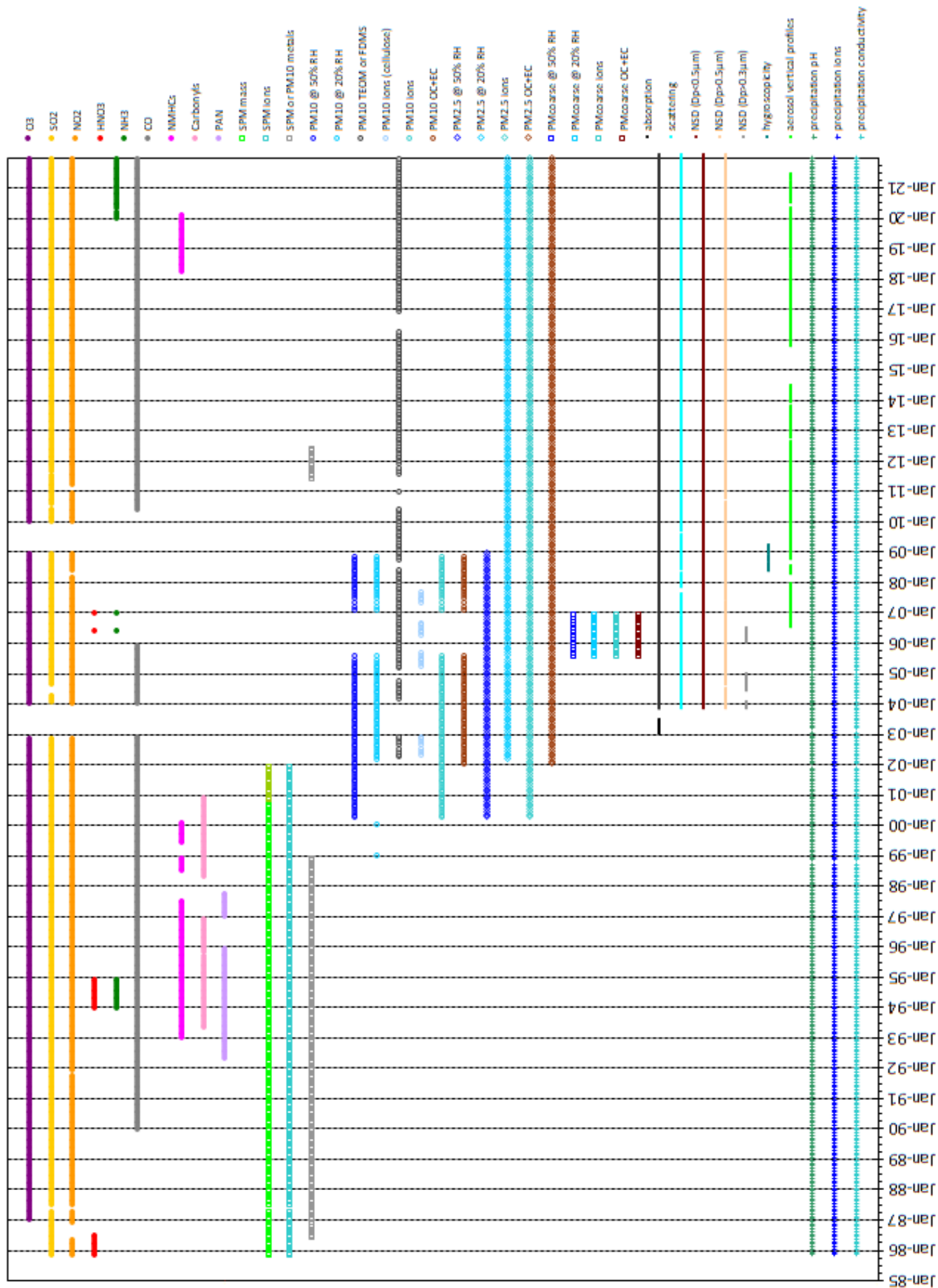
Currently, preliminary air pollution data obtained at the JRC-Ispra are visible and downloadable in real time from *http://abc-is.jrc.ec.europa.eu*. All validated data obtained at the JRC-Ispra station under the EMEP and the GAW programme, and other past and current international projects (EUSAAR, ACTRIS) can be retrieved from the EBAS database (*http://ebas.nilu.no/*), selecting "Ispra" as station of interest.

Additional information about the JRC-Ispra air monitoring station and other stations from the EMEP network can also be found in the following papers: Van Dingenen et al., 2004; Putaud et al., 2004; Mira-Salama et al., 2008; Putaud et al., 2010; Putaud et al., 2014; Cavalli et al.,2016; Kalabokas et al., 2020; Putaud et al., 2021.

Table 2. Variables related to short-lived pollutants and radiative forcers measured in 2021

METEOROLOGY	Pressure, temperature, humidity, wind, solar radiation
GAS PHASE	SO_2, NO_2, NO, NO_x, O_3, CO, NH_3
PARTICULATE PHASE	$PM_{2.5}$ mass, Cl^-, NO_3^-, SO_4^{2-}, Na^+, NH_4^+, K^+, Mg^{2+}, Ca^{2+}, OC, and EC contents Particle number size distribution (10 nm – 10 μm) Aerosol light absorption, scattering, back-scattering and extinction coefficients Altitude-resolved aerosol light back-scattering and extinction
WET DEPOSITION	Cl^-, NO_3^-, SO_4^{2-}, Na^+, NH_4^+, K^+, Mg^{2+}, Ca^{2+} pH, conductivity

Source: JRC, 2022

Fig. 9. Short-lived pollutants and climate forcers: data coverage for year 2021 (no NMHC data).
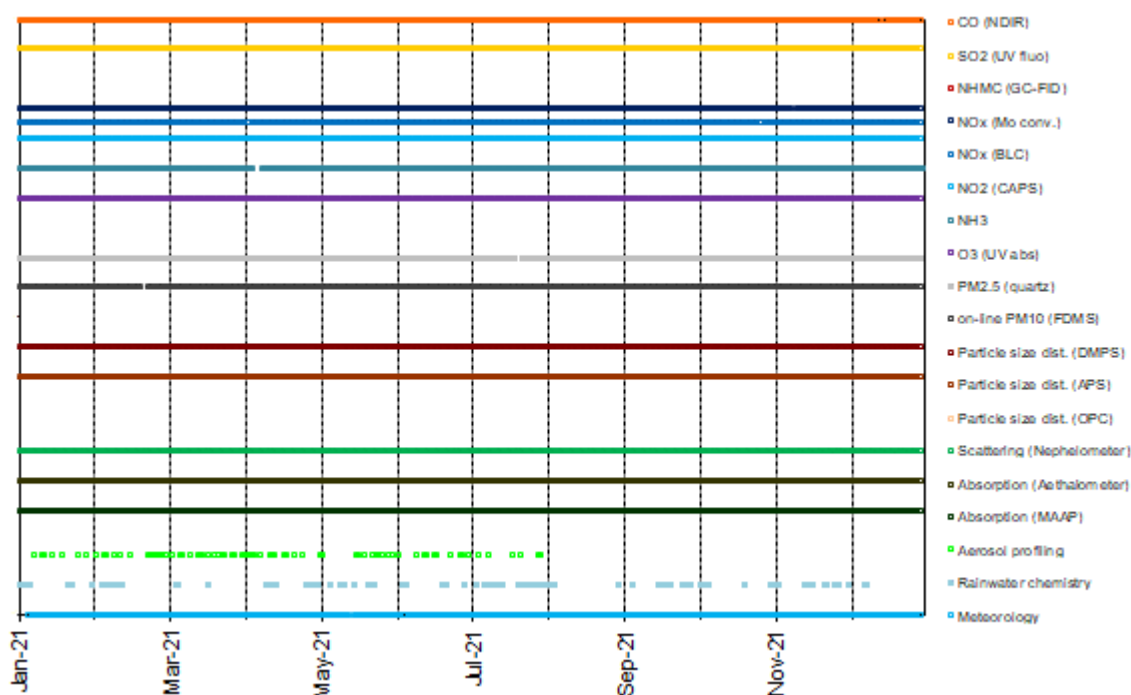
Source: JRC, 2022

4.2   Measurements and data processing

4.2.1   Air pollutant and short-lived radiative forcer measurements at Ispra in 2021

Since 1985, the JRC-Ispra air monitoring station programme has evolved significantly (Fig. 8). Measurements were carried out at the Atmospheric Observatory from July 2017. The measurements performed in 2021 are listed in Table 2, and Fig. 9 shows the data coverage.

Meteorological variables measurements were discontinued from 1 to 3 January, from 5 to 7 June, and for six shorter periods in 2021 (97% data coverage), mainly due to failures in the data acquisition system. Data gaps were filled by data taken from other weather stations of the JRC-Ispra site (rp.jrc.cec.eu.int/raman/, re.jrc.ec.europa.eu/meteo/).

SO_2, NOx and CO were measured quite continuously during the year 2021, with only a few hours missing due to automatic zero/span checks and annual maintenance (data coverage ≥99%). No valid non-methane hydrocarbon (NMHC) data were produced in 2021, due to sample trapping technical issues which could not be solved easily by the instrument supplier.

NH_3 was measured at 10 and 100 m above the ground for the whole year but from 6 to 8 April (99% data coverage) due to a crash of the instrument control software.

Daily particulate matter ($PM_{2.5}$) samples were collected and analysed for $PM_{2.5}$ mass (at 20% RH), main ions, OC (organic carbon) and EC (elemental carbon), for the whole of 2021 except for 4 days due to sampler malfunctioning (99% data coverage).

On-line PM_{10} measurements (FDMS-TEOM, Filter Dynamics Measurement System – Tapered Element Oscillating Microbalance) were carried out for the whole of 2021, except from 20 to 21 February for maintenance.

There were no significant gaps (>99% coverage) in the measurements of particle number size distributions (10 nm < D_p < 800 nm and 0.7 µm< D_p < 10µm), light scattering and light absorption coefficients in 2021.

The Raman LiDAR was operated according to the EARLINET schedule (Monday at solar noon ±1 hr, at sunset -2,+3hr, Thursday at sunset -2,+3hr, and during the ESA satellites Calipso and Aeolus overpasses (± 1hr), weather and staff availability permitting, till the end of July 2021. From this date, the laser power was below the value needed to take measurements and LiDAR measurement were discontinued.

Precipitation was collected throughout the year and analysed for pH, conductivity, and main ions (collected water volume permitting). Five significant precipitation events (1.2 to 8.6 mm) were missed in 2021.

4.2.2 Measurement techniques

4.2.2.1 On-line monitoring

<u>Meteorological Variables</u>

Meteorological data and solar radiation were measured directly at the EMEP station with the instrumentation described below.

WXT530 (S/N P1340407): until 9 Nov. 2022
WXT530 (S/N N2120878): from 9 Nov. 2022

Two WXT530 weather transmitters from Vaisala recorded the six weather variables temperature, pressure, relative humidity, precipitation and wind speed and direction from the top of a 10 m high mast at the provisional station, and from a 2 m mast on the terrace of the new observatory since Oct. 2017.

The wind data measurements utilise three equally spaced ultrasonic transducers that determine the wind speed and direction from the time it takes for ultrasound to travel from one transducer to the two others. Precipitation rate is measured with a piezoelectric sensor that detects the impact of individual raindrops and thus infers the accumulated rainfall. For the pressure, temperature and humidity measurements, separate sensors employing high precision RC oscillators are used.

Kipp and Zonen, SMP 11-V (S/N 167256): whole year

To determine the total solar radiation, a Kipp and Zonen CMP11 Pyranometer has been installed in 2015, which measures the irradiance (in W/m^2) on a plane surface from direct solar radiation and diffuse radiation incident from the hemisphere above the device. The CMP11 that was installed on the top of the container (3 m above ground) was replaced by the SMP11 on the terrace of the new observatory in Oct. 2017. The measurement principle is based on a thermal detector. The radiant energy is absorbed by a black disc and the heat generated flows through a thermal resistance to a heat sink. The temperature difference across the thermal resistance is then converted into a voltage and precisely measured. The CMP11 features a fast response time of 12 s, a small non stability of +/-0.5 % and a small non linearity of +/-0.2 %.

<u>Gas Phase Air Pollutants</u>

Sampling

SO_2, NO, NO_x, O_3, and CO have been measured at the new Atmospheric Observatory (at the same place as the historical site) since June 2017, and only there since January 2018.

The sampling line at the Atmospheric Observatory (inlet about 5 m above ground) consists of an inlet made of a stainless steel cylindrical cap (to prevent rain and bugs to enter the line), outside a stainless steel tube (diameter = about 4 cm), inside a glass tube (diameter = about 2.7 cm) and a glass manifold with eight ¼" connectors. This inlet is flushed by an about 45 L min^{-1} flow with a fan-coil (*measured 2 times per year with a gas-counter made by RITTER, sn. 11456, and online controlled with a flow sensor*). Each instrument samples from the tube with its own pump through a 0.25 inch Teflon line and a 5 µm pore size 47 mm diameter Teflon filter (to eliminate particles from the sampled air). See also Fig. 10.

Continuous NMHCs and NH_3 measurements were resumed in April 2018 and February 2020, respectively.

NMHCs are sampled an inlet identical to the one used for the other gaseous pollutant.

NH_3 is sampled alternatively (15 min sequences, first 10 minutes discarded) at 10 and 100 m above the ground through a ¼" PTFE tube with a flow rate of ~12 L min^{-1}, and through a ½" Synflex tube at a flow rate of ~11 L min^{-1}, respectively, using vacuum pumps (model KNF N 820 FT.18). A 5 µm pore size 47 mm diameter PTFE filter with is installed on the 10m line inlet. The 100 m sampling line includes two different particulate filters: A Pall Hepa Capsule Versapor filter at the 100m line inlet and a 7 µm nominal pore size filter (model Swagelok SS-8TF-7) at the end. A small air flow (around 0.2 L min^{-1}) is diverted from the main line toward the Picarro G2103 analyzer using a dedicated vacuum pump (model Vacuubrand, MD1) located downstream to the analyser.

The sampling flow rate for each gaseous pollutant analyser is indicated in Table 3.

For more details about the instruments here in chapter 4.2.2.1, see the manuals available at:
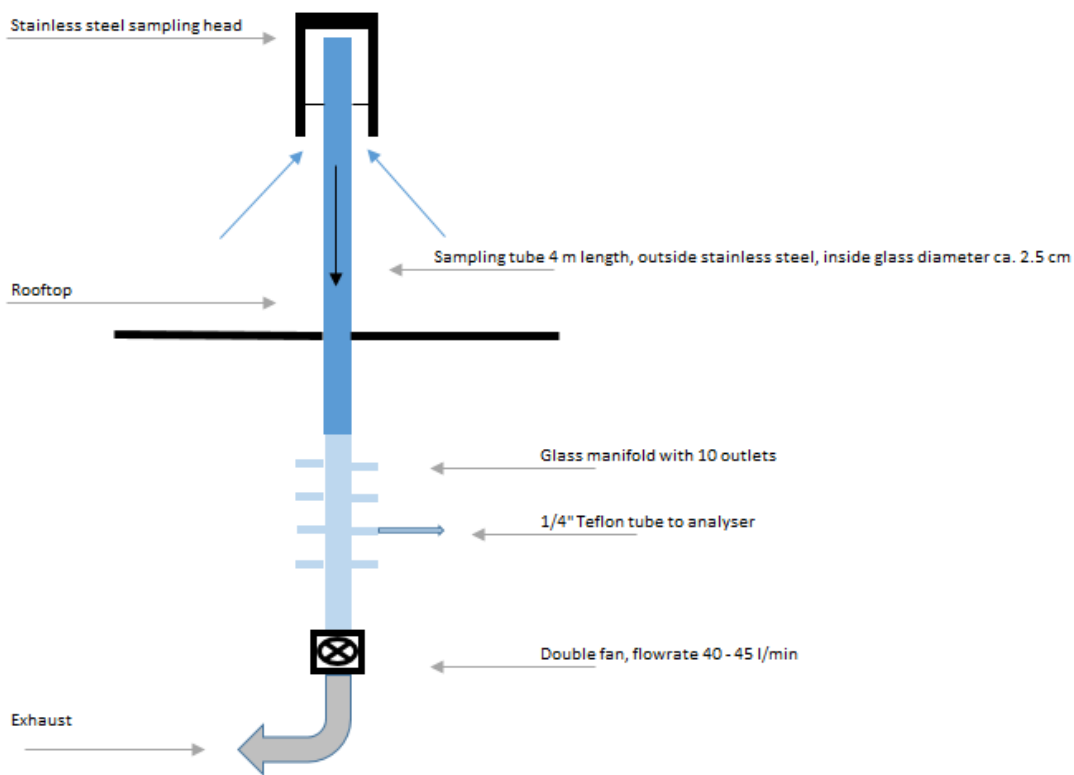\\s-jrcnubenacl1p.jrc.it\JRC.C.5_LargeFacilities\ABC-IS\Quality_management\Manuals

Table 3. *Sampling flow rates for the various gaseous analytes.*

Compounds	Flow rates (L min^{-1})
SO_2	0.5
NO, NO_x	1.0/1.3
O_3	0.7
CO	1.5
NMHC	0.04
NH_3	0.2

Source: JRC, 2021

Fig. 10. Sampling inlet system for the gaseous air pollutant at the mobile lab. Inlet for the measurements is about 5 m above ground.

Stainless steel sampling head

Sampling tube 4 m length, outside stainless steel, inside glass diameter ca. 2.5 cm

Rooftop

Glass manifold with 10 outlets

1/4" Teflon tube to analyser

Double fan, flowrate 40 - 45 l/min

Exhaust

Source: JRC, 2021

SO_2: UV Fluorescent SO_2 Analyser

Thermo 43iTLE   (S/N 1021443379): from 7 July 2021
                 (S/N 0724324323): until 7 July 2021

At first, the air flow is scrubbed to eliminate aromatic hydrocarbons. The sample is then directed to a chamber where it is irradiated at 214 nm (UV), a wavelength where SO_2 molecules absorb. The fluorescence signal emitted by the excited SO_2 molecules going back to the ground state is filtered between 300 and 400 nm (specific of SO_2) and amplified by a photomultiplier tube. A microprocessor receives the electrical zero and fluorescence reaction intensity signals and calculates SO_2 based on a linear calibration curve.

Calibration was performed with a certified SO_2 standard at a known concentration in air (around 40 ppb, Air Liquide). Zero check was done, using a zero air gas cylinder from Air Liquide, Alphagaz 1, CnHm < 0.5 ppm).

The specificity of the trace level Thermo instrument (TEI 43i-TLE) is that it uses a pulsed lamp. The 43i-TLE's detection limit is 0.05 ppbv (about 0.13 µg m^{-3}) over 300 second averaging time, according to the technical specifications.

For more details about the instruments, manuals are available at
\\s-jrcnubenacl1p.jrc.it\JRC.C.5_LargeFacilities\ABC-IS\Quality_management\Manuals.

NO + NO$_x$: Chemiluminescent Nitrogen Oxides Analyser (NO$_2$=NO$_x$-NO)

Thermo 42iTL   (S/N 936539473): whole year.

This nitrogen oxide analyser is based on the principle that nitric oxide (NO) and ozone react to produce excited NO$_2$ molecules, which emit infrared photons when going back to lower energy states:

$$NO + O_3 \rightarrow [NO_2]^* + O_2 \rightarrow NO_2 + O_2 + hv$$
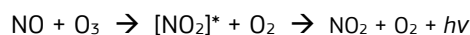
A stream of purified air (dried with a Nafion Dryer for 42iTL) passing through a silent discharge ozonator generates the ozone concentration needed for the chemiluminescent reaction. The specific luminescence signal intensity is therefore proportional to the NO concentration. A photomultiplier tube amplifies this signal.

NO$_2$ is detected as NO after reduction in a molybdenum (Mo) converter heated at about 325 °C.

The ambient air sample is drawn into the analyser, flows through a capillary, and then to a valve, which routes the sample either straight to the reaction chamber (NO detection), or through the converter and then to the reaction chamber (NO$_x$ detection). The calculated NO and NO$_x$ concentrations are stored and used to calculate NO$_2$ concentrations (NO$_2$ = NO$_x$ - NO), assuming that only NO$_2$ is reduced in the Mo converter. Detection limit was evaluated as 0.03 ppbv for NO and 0.05 ppbv for NOx (own evaluations)

Calibration was performed using a zero air gas cylinder (Air Liquide, Alphagaz 1, CnHm<0.5 ppm) and a certified NO span gas (around 85 ppb NO in N$_2$, Air Liquide).

For more details about the instruments, the manuals are available at
\\s-jrcnubenacl1p.jrc.it\JRC.C.5_LargeFacilities\ABC-IS\Quality_management\Manuals

NO + NO$_x$ - BLC: Chemiluminescent Nitrogen Oxides Analyser (NO$_2$=NO$_x$-NO)

Thermo 42iTL   (S/N 710820808): whole year.

This nitrogen oxide analyser is based on the same principle with the only difference that NO$_2$ is detected as NO after passing a converter with two solid state light sources (blue light convertor). This technique allows a more selective measurement of NO$_2$. Converter efficiency is evaluated or checked during 3-month calibrations and NO$_2$ data corrected accordingly afterwards.

NO$_2$: Cavity attenuated phase shift (CAPS) Nitrogen Dioxide Analyzer

Aerodyne CAPS NO2   (S/N: 114002)

The CAPS NO$_2$ monitor measures nitrogen dioxide directly by absorption of light at 450 nm. Thanks to the direct measurement it can be considered 'interferent – free' with a linear response. A laptop runs the analyser-software and stores the measured data. Once a day data are transferred automatically to UBIS4 database.

Baseline of the analyser is measured and corrected once per hour with NO$_2$ free air and the calibration is checked every three months.

Detection limit is <0.1 ppbv according to technical specifications.

O$_3$:   UV Photometric Ambient Analyser

Thermo 49i   (S/N CM09360104): until 23 June 2021
                              (S/N 1150120006): from 23 June 2021

The UV photometer determines ozone concentrations by measuring the absorption of O$_3$ molecules at a wavelength of 254 nm (UV light) in the absorption cell, followed by the use of Beer-Lambert law. The concentration of ozone is related to the magnitude of the absorption. The reference gas, generated by scrubbing ambient air, passes into one of the two absorption cells to establish a zero light intensity reading, I$_0$. Then the sample passes through the other absorption cell to establish a sample light intensity reading, I. This cycle is reproduced with inverted cells. The average ratio R=I/I$_0$ between 4 consecutive readings is directly related to the ozone concentration in the air

sample through the Beer-Lambert law. Calibration is performed using externally generated zero air and external span gas. Zero air is produced by a JPAC zero air generator supplying a TEI 49C-PS transportable primary standard ozone calibrator (S/N 56676-309) to generate zero air and Span gas normally in the range 50 - 100 ppb. The TEI 49C-PS is calibrated/check by ERLAP (European Reference Laboratory of Air Pollution) against a NIST Standard Reference Photometer. A Nafion Dryer system is connected to the O_3 instrument. Detection limit was evaluated as 0.3 ppbv (type approval).

For more details about the instruments, the manual is available on
\\s-jrcnubenacl1p.jrc.it\JRC.C.5_LargeFacilities\ABC-IS\Quality_management\Manuals

CO: Non-Dispersive Infrared Absorption CO Analyser

Horiba AMPA-370   (S/N: VM92B6WA): whole year

In 2021, carbon monoxide (CO) has been continuously monitored using a commercial Horiba AMPA-370 CO monitor based on the principle of non-dispersive infrared absorption (NDIR). The Horiba APMA-370 uses solenoid valve cross flow modulation applying the same air for both the sample and the reference, instead of the conventional technique to apply an optical chopper to obtain modulation signals. With this method the reference air is generated by passing the sample air over a heated oxidation catalyst to selectively remove CO which is then directly compared to the signal of the untreated sample air at a 1 Hz frequency. The result is a very low zero-drift and stable signal over long periods of time.

To reduce the interference from water vapour to about 1% the sample air was dried to a constant low relative humidity level of around 30% applying a Nafion dryer (Permapure MD-070-24P) in the inlet stream. The detection limit of the Horiba AMPA-370 is ~30 ppbv for a 1-minute sampling interval.

Non-Methane Hydrocarbons (NMHC): Gas chromatograph with Flame Ionisation Detection

Agilent Technology, 7890A GC-System (S/N: CN13021054): whole year

Markes International, Series 2 Unity Trap system (S/N: GB00U21897): idem

In 2021, about 30 NMHCs were measured using an on-line with GC-FID (Gas Chromatography – Flame Ionization Detection), associated with a cold 'trap' system and thermal desorption.

Outside ambient air in drawn through a glass inlet tube located about 6 m above ground level (Building 77r) via a glass line with a 25 mm inner diameter and 4 m long borosilicate tube at a flow rate of about 1.5 m s^{-1} (see also Fig. 10). The residence time for the sampled air in the tubes before arriving to the manifold is about 2-3 s. The air sample is drawn from the manifold to the sampling tube through a Nafion dryer at a flow rate of about 40 ml min^{-1}. The residence time in the Teflon line (about 2 m long and with an inner diameter of about 1 mm) is about 2 s. The Nafion dryer uses N_2 as a counter flow ("nominal" counter flow rate: 250 ml min^{-1}). NMHCs are collected below 0 °C in the cold trap (U-T503F-2S) suitable for ozone precursors from acetylene to trimethylbenzene and freons. The cold trap is desorbed to a sorbent tube (P/N U-T4WMT) containing three materials (Tenax TA backed by Carbograph 1TDTM backed by Carboxen 1000TM) each separated and supported by unsilanised glass wool plugs, optimised for focusing on compounds ranging from C2 to C24. This sorbent is normally stable for years, and should normally not be exchanged every year. Collected NMHCs are thermally desorbed at about 100°C (using also a split tube) and injected through a heated valve to the GC. The sample tube and the cold trap then cool down and are purged with Helium at some ml min^{-1} for about 10 min.

Desorbed NMHCs are carried to the splitter by the He carrier gas. The sample is injected in parallel in a polar column and a nonpolar column where NMHCs are separated. GC's thermal protocols begin at 30°C and terminates at about 100 °C within about 30 min. A flame ionizing detector (FID) is used to quantify the C atoms of each NMHC species. At the end of the analytical protocol, the oven temperature gets down to 30 °C after about 10 min. The whole process (sampling + analyses) takes about 60 min.

Because of problems with the 'trap-system' resulting in a to low signal, there are no valid data available for the year 2021 (after interventions by the technician from 'SRA Instruments' the system was working fine again in Jan. 2022).

NH$_3$: Cavity Ring-Down Spectrometer (CRDS)

Picarro G2103 (S/N: 3543- AHDS2154)

The new CRDS instrument for measurement of NH$_3$ and H$_2$O (model Picarro G2103) was installed in the GHG laboratory in February 2020. At the heart of the apparatus, an optical cavity is brought into resonance with a laser light source, allowing an intra-cavity optical field to build up. The light source is then abruptly turned off and the

intra-cavity power decay ("ring down") time constant is measured by monitoring the intensity of the light at 6548.6 cm^{-1} and 6548.8 cm^{-1} (ca. 1527 nm). Direct and indirect cross-interference from water vapour on NH_3 measurements are corrected for.

NH_3 concentration is measured at 10m and 100m above ground level with a time resolution of 1 second. A rotary valve (model Valco Vici EMT2SD16MWE) allows to select the tower level to be analysed. The instrument directly controls this valve in order to sample the two levels sequentially for twice 15 minutes within one hour.

Calibrating the Picarro G2103 detector with NH_3 standards is challenging. However, the analyzer is measuring also CO_2 that has an absorption spectra adjacent to ammonia, making it an excellent surrogate gas for the validation of accuracy and linearity (span validation) of Picarro G2103 for NH_3 measurements. In order to perform this span validation four standard cylinders with CO_2 concentration ranging between 379 ppm and 471 ppm have been used. Each standard was injected for 30 minutes and analyzed three times (three cycles). A linear regression between assigned CO_2 concentrations and measured values has been calculated for each cycle. If the slope of the linear regression is in the range 0.95 – 1.05, then the standard calibration constant of the instrument does not need any change. This test was executed once in 2021. The span validation has been executed on January 2021 and the slope of the regression was 0.99.

Atmospheric Particles

Sampling Conditions

Since 2008, all instruments for the physical characterisation of aerosols (Multi-Angle Absorption Photometer, Aethalometer, Nephelometer, Aerodynamic Particle Sizer, Differential Mobility Particle Sizer) sample isokinetically from an Aluminium inlet pipe (diameter = 15 cm, length of horizontal part ~280 cm and vertical part ~220 cm) described in Jensen et al., 2010. The Tapered Element Oscillating Micro-balance (FDMS-TEOMs) uses its own inlet systems. The MAAP samples from the main inlet through Nafion dryers at a flow rate of 480 L hr^{-1} since March 2016.

Fig. 11. Particle number size distribution observed at both ends of the horizontal part of the aerosol manifold (Dec. 2017).
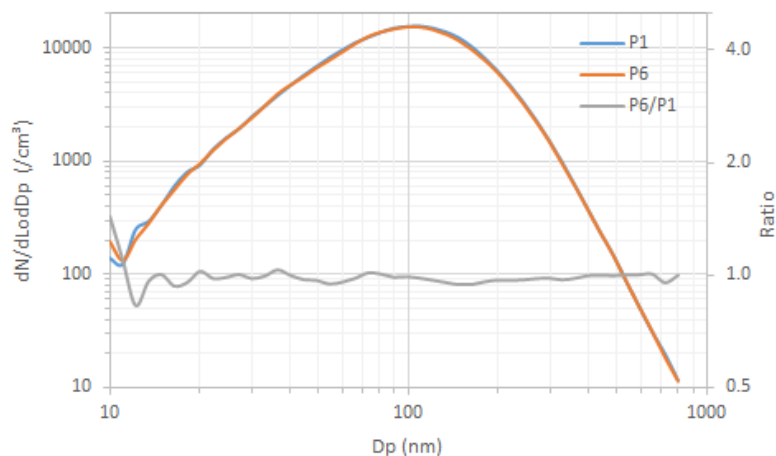
Source: JRC, 2017

The size dependent particle losses along the pipe radius were determined by measuring the ambient aerosol size distribution with two Differential Mobility Particle Sizers (DMPS) at the sampling points P0 (close to the inlet) and P2 (close to the end of the pipe) for different radial positions relative to the tube centre (0, 40 and 52 mm) at P2 (Gruening et al., 2009). Data show a small loss of particles towards the rim of the tube can be observed, but it stays below 15 %. The bigger deviation for particles smaller than 20 nm is again a result of very small particle number concentrations in this diameter range and thus rather big counting errors. Particle losses in the aerosol manifold installed at the new Atmospheric Observatory have been measured using two inter-calibrated DMPS sampling close to the inlet (P1) and close to the outlet (P6) of the horizontal part of the manifold (Fig. 11). Losses at P6 compared to P1 were < 6% for all particle sizes between 20 and 800 nm (average 2%), which indicates no significant biases for the measurement of particle light absorption and scattering coefficient in the vicinity of P6.

PM$_{10}$ Mass Concentration: Tapered Element Oscillating Mass balance (TEOM®), Series 1400a
Thermo TEOM FDMS 1405-F (S/N 240401712)

The TEOM 1405 Monitor is composed of two major components, the sample inlet assembly and the TEOM 1405 unit. The user enters the system parameters into the TEOM 1405 unit using a color touchscreen that is located on the front of the unit. Additionally, the system is furnished with software for personal computers (a PC with an updated version of Windows XP is required to allow the user to download data and update instrument firmware. The instrument does not require a dedicated computer to function in the field.

The sensor unit contains a mass measurement hardware system that monitors Particles that continuously accumulate on the system's exchangeable TEOM filters. By maintaining a flow rate of 3 l/min through the particulate channel, and measuring the total mass accumulated on the TEOM filter, the device can calculate the mass concentration in near real time.

The Series 1400a TEOM monitor incorporates an inertial balance patented by Rupprecht & Patashnick, now Thermo Scientific. It measures the mass collected on an exchangeable filter cartridge by monitoring the frequency changes of a tapered element. The sample flow passes through the filter, where particulate matter is collected, and then continues through the hollow tapered element on its way to an electronic flow control system and vacuum pump. As more mass collects on the exchangeable filter, the tube's natural frequency of oscillation decreases. A *direct* relationship exists between the tube's change in frequency and mass on the filter. The TEOM mass transducer does not require recalibration because it is designed and constructed from non-fatiguing materials.

The instrument set-up includes a Sampling Equilibration System (SES) that allows a water strip-out without sample warm up by means of Nafion Dryers. In this way the air flow RH is reduced to < 30%, when TEOM operates at 30°C only. The Filter Dynamic Measurement System (FDMS) is based on measuring changes of the TEOM filter mass when sampling alternatively ambient and filtered air. The changes in the TEOM filter mass while sampling filtered air is attributed to sampling (positive or negative) artefacts, and is used to correct changes in the TEOM filter mass observed while sampling ambient air.

In June 2021 a general maintenance to the TEOM *(S/N 240401712)* was performed by our staff. The maintenance included the filters replacement.

Particle Number Size Distribution: Differential Mobility Particle Sizer (DMPS)
DMPS A, DMA serial no. 158, DMPS CPC 3772 TSI s/n 3772133103, Total Counting CPC 3772 TSI s/n 70847419, bipolar charger ^{85}Kr 10 mCi (s/n 004/17) since December 2017.

The Differential Mobility Particle Sizer consists of a custom-made medium size (inner diameter 50 mm, outer diameter 67 mm and length 280 mm) Vienna-type Differential Mobility Analyser (DMA) and a Condensation Particle Counter (CPC), TSI 3772. Its setup follows the ACTRIS specifications for DMPS systems.

DMAs use the fact that electrically charged particles move in an electric field according to their electrical mobility. Electrical mobility depends mainly on particle size and electrical charge. Atmospheric particles are brought in the bipolar charge equilibrium in the bipolar diffusion charger (Eckert & Ziegler neutraliser with 370 MBq): a radioactive source (^{85}Kr) ionises the surrounding atmosphere into positive and negative ions. Particles carrying a high charge can discharge by capturing ions of opposite polarity. After a very short time, particles reach a charged equilibrium such that the aerosol carries the bipolar Fuchs-Boltzman charge distribution. A computer programme sets stepwise the voltage between the 2 DMA's electrodes (from 10 to 11500 V). Negatively charged particles are so selected according to their mobility. After a certain waiting time, the CPC measures the number concentration for each mobility bin. The result is a particle mobility distribution. The number size distribution is calculated from the mobility distribution by an inversion routine (from Stratmann and Wiedensohler, 1996) based on the bipolar charge distribution and the size dependent DMA transfer function. The DMPS measures aerosol particles in the range 10 - 800 nm with a 12-min cycle. It records data using 45 size channels for high-resolution size information. This submicrometer particle sizer system is capable of measuring concentrations in the range from 1 to 2.4 x 10^6 particles cm^{-3}. Instrumental parameters that are necessary for data evaluation such as flow rates, relative humidity, ambient pressure and temperature are measured and saved as well.

The CPC detection efficiency curve and the particle diffusion losses in the system are taken into account at the data processing stage.

Accessories include:

- FUG High voltage cassette power supplies Series HCN7E – 12500 Volts.
- Rotary vacuum pump vane-type (sampling aerosol at 1 LPM)
- Controlled blower (circulating dry sheath air)
- Nafion dryers for the sheath and sample air streams, implemented since October 2009.

- Mass flow meter and pressure transducer (to measure sheath air and sample flows).

Particle Number Size Distribution: Aerodynamic Particle Sizer (APS)

APS TSI 3321 (S/N 70535014): whole year

The APS 3321 is a time-of-flight spectrometer that measures the velocity of particles in an accelerating air flow through a nozzle.

Ambient air is sampled at 1 L min^{-1}, sheath air at 4 L min^{-1}. In the instrument, particles are confined to the centre-line of an accelerating flow by sheath air. They then pass through two broadly focused laser beams, scattering light as they do so. Side-scattered light is collected by an elliptical mirror that focuses the collected light onto a solid-state photodetector, which converts the light pulses to electrical pulses. By electronically timing the gap between the peaks of the pulses, the velocity can be calculated for each individual particle.

Velocity information is stored in 1024 time-of-flight bins. Using a polystyrene latex (PSL) sphere calibration, which is stored in non-volatile memory, the APS Model 3321 converts each time-of-flight measurement to an aerodynamic particle diameter. For convenience, this particle size is binned into 52 channels (on a logarithmic scale).

The particle range spanned by the APS is 0.5 - 20 μm in both aerodynamic size and light-scattering signal. Particles are also detected in the 0.3 to 0.5 μm range using light-scattering alone, and are binned together in one channel. The APS is also capable of storing correlated light-scattering-signal. *dN/dLogDp* data are averaged over 10 min.

Particle Light Scattering and Backscattering Coefficients

Integrating Nephelometer TSI 3563 (S/N 1081): whole year

The integrating nephelometer is a high-sensitivity device capable of measuring the scattering properties of aerosol particles. The nephelometer measures the light scattered by the aerosol and then subtracts the light scattered by the walls of the measurement chamber, light scattered by the gas, and electronic noise inherent in the detectors.

In 2021, dried ambient air was sampled at flow rates ranging from 6.0 to 6.2 L min^{-1}.

The three-colour detection version of TSI nephelometer detects scattered light intensity at three wavelengths (450, 550, and 700 nm). Normally the scattered light is integrated over an angular range of 7–170° from the forward direction, but with the addition of the backscatter shutter feature to the Nephelometer, this range can be adjusted to either 7–170° or 90–170° to give total scatter and backscatter signals. A 75 Watt quartz-halogen white lamp, with a built-in elliptical reflector, provides illumination for the aerosol. The reflector focuses the light onto one end of an optical pipe where the light is carried into the internal cavity of the instrument. The optical pipe is used to thermally isolate the lamp from the sensing volume. The output end of the optical light pipe is an opal glass diffuser that acts as a *quasi*-cosine (Lambertian) light source. Within the measuring volume, the first aperture on the detection side of the instrument limits the light integration to angles greater than 7°, measured from the horizontal at the opal glass. On the other side, a shadow plate limits the light to angles less than 170°. The measurement volume is defined by the intersection of this light with a viewing volume cone defined by the second and fourth aperture plates on the detection side of the instrument. The fourth aperture plate incorporates a lens to collimate the light scattered by aerosol particles so that it can be split into separate wavelengths. The nephelometer uses a reference chopper to calibrate scattered signals. The chopper makes a full rotation 23 times per second. The chopper consists of three separate areas labelled "signal", "dark", and "calibrate". The "signal" section simply allows all light to pass through unaltered. The "dark" section is a very black background that blocks all light. This section provides a measurement of the photomultiplier tube (PMT) background noise. The third section is directly illuminated to provide a measure of lamp stability over time. To reduce the lamp intensity to a level that will not saturate the photomultiplier tubes, the "calibrate" section incorporates a neutral density filter that blocks approximately 99.9 % of the incident light. To subtract the light scattered by the gas portion of the aerosol, a high-efficiency particulate air (HEPA) filter is switched in line with the inlet for 300 s every day at 08:00 UTC. This allows compensation for changes in the background scattering of the nephelometer, and in gas composition that will affect Rayleigh scattering of air molecules with time. When the HEPA filter is not in line with the inlet, a small amount of filtered air leaks through the light trap to keep the apertures and light trap free of particles. A smaller HEPA filter allows a small amount of clean air to leak into the sensor end of the chamber between the lens and second aperture. This keeps the lens clean and confines the aerosol light scatter to the measurement volume only.

Nephelometer data are corrected for angular non-idealities and truncation errors according to Anderson and Ogren, 1998. A Nafion dryer has been installed (18.11.2009) at the inlet to measure light scattering by dry aerosols. Internal RH ranged between 0 and 40 % for 97% of the time in 2021 (average 19%, 99th percentile 35%) with 274 measurement hours above 40% on July - August (up to 52% RH) though. At 40% RH, aerosol scattering would

be on average increased by about 15% compared to 0% RH in Ispra (Adam et al., 2012). However, aerosol particle scattering coefficients presented in this report are **not** corrected for RH effects, except when specified.

Particle Light Extinction and Scattering Coefficients

Cavity Attenuated Phase Shift (CAPS) single scattering albedo monitor
Aerodyne CAPS PM$_{SSA}$ (S/N 318005): whole year

This Cavity Attenuated Phase Shift monitor (CAPS PM$_{SSA}$) operates both as an optical extinction spectrometer and as an integrating nephelometer.

Extinction: One channel measures with a vacuum photodiode detector the average time spent by the square wave modulated light produced by a LED (630 nm) within the sample cell. Being equipped with two high reflectivity mirrors (R ≥ 0.9998), the optical path length in the cell is about 1-2 km. In the absence of particles, the photon lifetime within the cell is on the order of several µs, a magnitude which can readily be measured with high accuracy. This average time decreases as the particle concentration increases.

Scattering: an integrating volume is incorporated into the extinction measurement cell. This integrating volume maximizes the collection of scattered light at the photomultiplier tube (2nd channel) which views scattered light from the optical cell at 90° angles to the optical beam. The second is to minimize the light collection bias with respect to scattering angle. The white coating on the surface of the sphere provides a near perfect Lambertian surface (photons scatter at random angles which bear no relationship to the initial angle of incidence). Because the integrating volume is not perfect (its reflectance is not 98% and there are finite openings in the volume to allow the optical beam to enter and exit), a truncation correction (which is a function of particle diameter) must be applied.

Particle Light Absorption Coefficient

Aethalometer Magee AE-31 'A' (S/N 740:0609): whole year
(S/N 4080303): whole year

The principle of the Aethalometer is to measure the attenuation of a beam of light transmitted through a filter, while the filter is continuously collecting an aerosol sample. Suction is provided by an internally-mounted pump. Attenuation measurements are made at successive regular intervals of a time-base period. The objectives of the Aethalometer hardware and software systems are as follows:

(a) to collect the aerosol sample with as few losses as possible on a suitable filter material;

(b) to measure the optical attenuation of the collected aerosol deposit as accurately as possible;

(c) to calculate the rate of increase of the equivalent black carbon (EBC) component of the aerosol deposit and to interpret this as an EBC concentration in the air stream;

(d) to display and record the data, and to perform necessary instrument control and diagnostic functions.

The optical attenuation of the aerosol deposit on the filter is measured by detecting the intensity of light transmitted through the spot on the filter. In the AE-31, light sources emitting at different wavelengths (370, 470, 520, 590, 660, 880 and 950 nm) are also installed in the source assembly. The light shines through the lucite aerosol inlet onto the aerosol deposit spot on the filter. The filter rests on a stainless steel mesh grid, through which the pumping suction is applied. Light penetrating the diffuse mat of filter fibres can also pass through the spaces in the support mesh. This light is then detected by a photodiode placed directly underneath the filter support mesh. As the EBC content of the aerosol spot increases, the amount of light detected by the photodiode will diminish.

For better accuracy, additional measurements are necessary: the amount of light penetrating the combination of filter and support mesh is relatively small, and a correction is needed for the 'dark response signal' of the overall system. This is the electronics' output when the lamps are off: typically, it may be a fraction of a percent of the response when the lamps are on. To eliminate the effect of the dark response, we take 'zero' readings of the system response with the lamps turned off, and subtract this 'zero' level from the response when the lamps are on.

The other measurement necessary is a 'reference beam' measurement to correct for any small changes in the light intensity output of the source. This is achieved by a second photodiode placed under a different portion of the filter that is not collecting the aerosol, on the left-hand side where the fresh tape enters. This area is illuminated by the same lamps. If the light intensity output of the lamps changes slightly, the response of this detector is used to correct mathematically the 'sensing' signal. The reference signal is also corrected for the dark response 'zero' as described above.

The algorithm in the software (see below) can account for changes in the lamp intensity output by always using the ratio quantity [Sensing]/[Reference]. As the filter deposit accumulates, this ratio will diminish.

In practice, the algorithm can account for lamp intensity fluctuations to first order, but we find a residual effect when operating at the highest sensitivities. To minimise this effect and to realise the full potential of the instrument, it is desirable for the lamps' light output intensity to remain as constant as possible from one cycle to the next, even though the lamps are turned on and off again. The software monitors the repeatability of the reference signal, and issues a warning message if the fluctuations are considered unacceptable. When operating properly, the system can achieve a reference beam repeatability of better than 1 part in 10000 from one cycle to the next. The electronics circuit board converts the optical signals directly from small photocurrents into digital data, and passes it to the computer for calculation. A mass flow meter monitors the sampled air flow rate. These data and the result of the EBC calculation are written to disk and displayed on the front panel of the instrument.

Aethalometer data can be corrected for the shadowing effect and for multiple-scattering in the filter to derive the aerosol absorption coefficient (Arnott et al., 2005) with a correction factor C = 3.60, 3.65, and 3.95 for 470, 520 and 660 nm, respectively. Note that ACTRIS provisionally recommends the use of a constant conversion factor C_0 = 3.5 for all wavelengths (Mueller, 2015).

Multi Angle Absorption Photometer (S/N 2310): whole year

A Multi Angle Absorption Photometer (MAAP) model 5012 from Thermo Scientific was installed at the EMEP station in September 2008 and provides equivalent black carbon concentrations (EBC) and aerosol absorption (*a*) data at a nominal wavelength of 670 nm. Note that during a EUSAAR workshop (www.eusaar.org) in 2007 it has been observed that the operating wavelength of all MAAP instruments present at that workshop was 637 nm with a line width of 18 nm (full width at half maximum). The operating wavelength of our MAAP instrument (S/N 2310) has not been measured yet, but it is assumed to light at 637 nm as observed in other instruments of the same model.

The MAAP is based on the principle of aerosol-related light absorption and the corresponding atmospheric equivalent black carbon (EBC) mass concentration. Model 5012 uses a multi angle absorption photometer to analyse the modification of scattering and absorption in the forward and backward hemisphere of a glass-fibre filter caused by deposited particles. The internal data inversion algorithm of the instrument is based on a radiation transfer model and explicitly takes into account multiple scattering processes inside the deposited aerosol and between the aerosol layer and the filter matrix (see Petzold et al., 2004).

The sample air is drawn into the MAAP and aerosols are deposited onto the glass fibre filter tape. The filter tape accumulates the aerosol sample until a threshold value is reached, then the tape is automatically advanced. Inside the detection chamber (Fig. 12), a red light emitting diode is aimed towards the deposited aerosol and filter tape matrix. The light transmitted into the forward hemisphere and reflected into the back hemisphere is measured by a total of five photo-detectors. During sample accumulation, the light intensities at the different photo-detectors change compared to a clean filter spot. The reduction of light transmission, change in reflection intensities under different angles and the air sample volume are continuously measured during the sample period. With these data and using its proprietary radiation transfer scheme, the MAAP calculates the equivalent black carbon concentration (EBC) as the instruments measurement result.

Using the specific absorption cross section σ_{BC} = 6.6 m^2/g of equivalent black carbon at the operation wavelength (nominally 670 nm), the aerosol absorption (*a*) at that wavelength can be readily calculated as:

$$\alpha = EBC \times \sigma_{BC}$$

<div align="right">Eq. 1</div>

Fig. 12. MAAP detection chamber (sketch from the instrument manual).
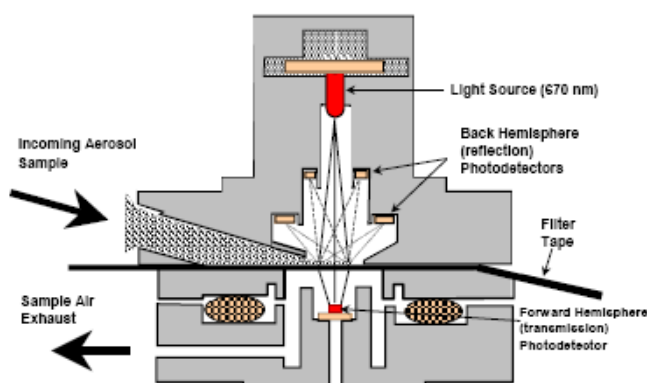
Source: THERMO Scientific

Range-Resolved Aerosol Light Backscattering and Extinction

Raymetrics Aerosol Raman Lidar (S/N 400-1-12, QUANTEL Brilliant B Laser and cooler S/N 120059004 and S/N 120034401, LICEL Transient Recorder & Hi Voltage Supply S/N BS3245 and BS3245b, industrial PC S/N TPL-1571H-D3AE)

LiDAR measurements are based on the time-resolved detection of the backscattered signal of a short laser pulse that is sent to the atmosphere (for an introduction see Weitkamp, 2005). Using the speed of light, time is converted to the altitude where the backscattering takes place. Using the particle-free range of the atmosphere for calibration (where Rayleigh scattering from the air molecules is known), aerosol backscattering and extinction coefficients as well as aerosol optical thickness can be derived using the LIDAR equation. The received power P of the detector is therein given as a function of distance and wavelength by *Eq. 2*:

$$P(R, \lambda) = P_0 \, {c\tau}/{2} \, A \, \eta \, \frac{O(R)}{R^2} \, \beta(R, \lambda) \exp\left(-2\int_0^R \alpha(r, \lambda) dr\right)$$

Eq. 2

with P_0: Power of the laser pulse, c: speed of light, τ: laser pulse length, A: area of the telescope, η: system efficiency, R: distance, O: overlap function (between laser beam and receiving optics field of view), λ: wavelength, β: backscatter coefficient, α: absorption coefficient.

The instrument itself was installed on October 8-11th, 2012, and accessories (including radar) on December 11-13, 2012. This lidar emits at 3 wavelengths from IR to UV (1064 nm, polarised-532 nm, 355 nm) and records at 5 wavelengths, namely the emission wavelengths and two vibrational Raman channels at 387 and 607 nm. Measurements at 1064 nm, 532 nm, and 355 nm provide aerosol backscatter profiles, while measurements at 687 nm, and 387 nm provide aerosol extinction profiles during the dark hours of the day. The depolarisation of the 532 nm light beam is also measured. After the re-installation of the laser in Nov. 2015, the instrument has been run with a 5 min integration time according to the ACTRIS schedule (2 to 5 hr slots covering noon on Mondays and sunset on Mondays and Thursdays), and during the Calipso satellite overpasses (about once every 8 days at 01:40 or 12:30 UTC). The emission window was removed when the LiDAR was placed in a dedicated shelter on 28 May 2018. Data are inverted using the online Single Calculus Chain developed by EARLINET, after pre-processing to cope with new requirements for submitting data to the ACTRIS-EARLINET data bank.

4.2.2.2 Sampling and off-line analyses

<u>Particulate Matter</u>

Particle sampler: Partisol 2025 S/N 2025B216790401
Micro-balance: MC5 S/N 50208287
Ion Chromatographs: ICS 2000 S/N 07101404 and 07101405
OC-EC analyser: Sunset Lab OCEC analyser S/N 173.

$PM_{2.5}$ was continuously sampled at 16.7 L min^{-1} on quartz fibre filters with a Partisol sampler equipped with a carbon honeycomb denuder. The sampled area is 39 mm Ø. Filters were from PALL Life Sciences (type TISSUEQUARTZ 2500QAT-UP). Filter changes occurred daily at 08:00 UTC.

Filters were weighed at 20 % RH before and after sampling with a microbalance Sartorius MC5 placed in a controlled (dried or moisture added and scrubbed) atmosphere glove box. They were stored at 4°C until analysis.

Main ions (Cl^-, NO_3^-, SO_4^{2-}, $C_2O_4^{2-}$, Na^+, NH_4^+, K^+, Mg^{2+}, Ca^{2+}) were analysed by ion chromatography with electrochemical eluent suppression (ICS2000) after extraction of the soluble species from an aliquot of 16 mm Ø in 10 ml of 18.2 MOhm cm resistivity water (Millipore mQ).

Organic and elemental carbon (OC+EC) were analysed using a Sunset Dual-optical Lab Thermal-Optical Carbon Aerosol Analyser (S/N 173-5). $PM_{2.5}$ samples were analysed using the EUSAAR-2 thermal protocol according to EN 16909. It has been developed to minimise biases inherent to thermo-optical analysis of OC and EC (Cavalli et al., 2010), and is described in Table 4 below.

<u>Wet-only deposition</u>

Precipitation sampler: <u>Eigenbrodt</u> Model NSA 181/KS S/N 3312 (whole year).
Conductimeter and pH-meter: Sartorius Professional Meter PP-50 S/N 16350322.
Ion Chromatographs: ICS 2000 S/N 07101404 and 07101405

For precipitation collection, two wet-only samplers were used that automatically collect the rainfall in a 1 L polyethylene container. The collection surface is 550 cm^2. 24-hr integrated precipitation samples (if any) are col-

Fig. 13. Set-up of the Data Acquisition System in the Aerosol Physics Laboratory
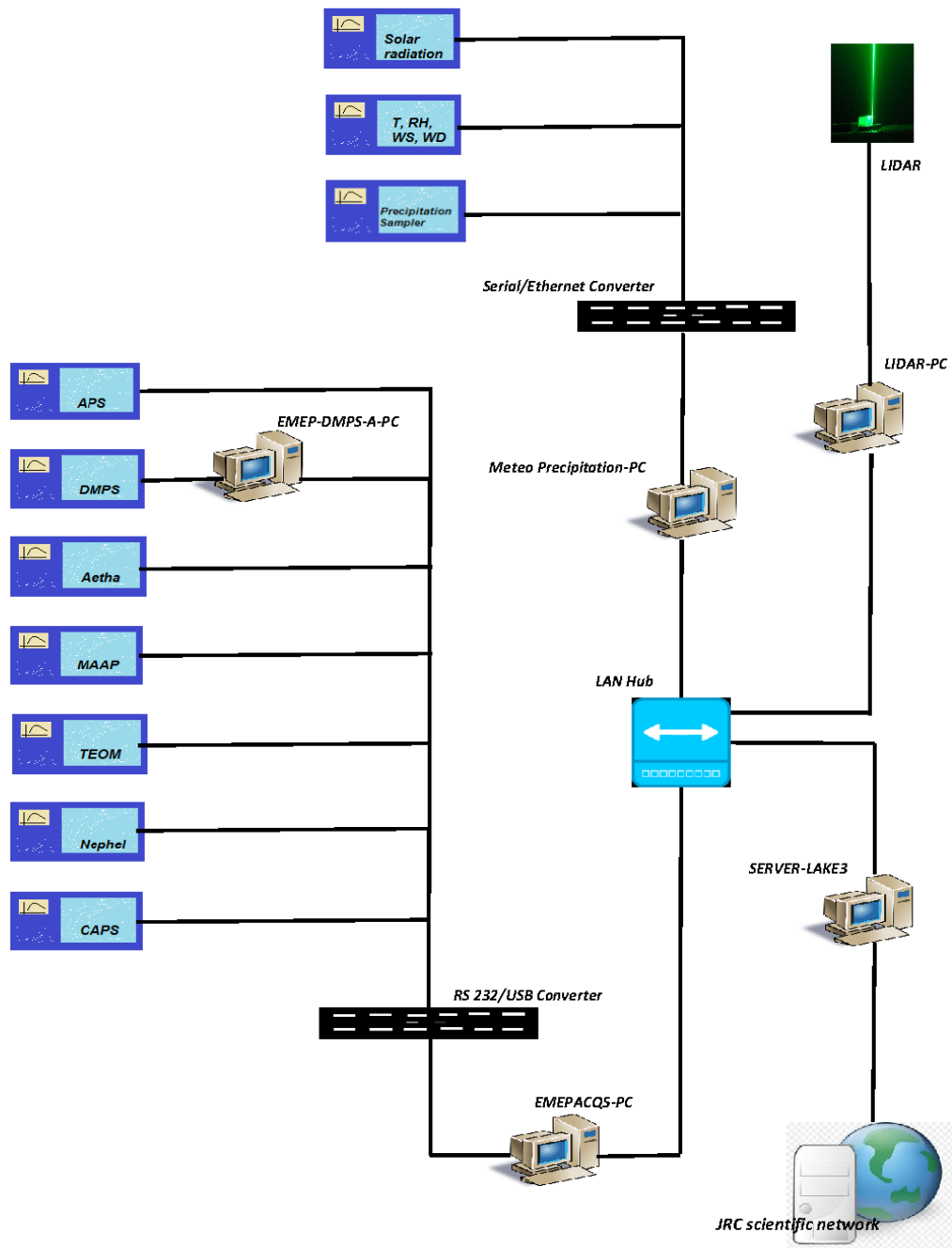
Source: JRC, 2022

lected every day starting at 8:00 UTC. All collected precipitation samples were stored at 4 °C until analyses (ca. every 3 months). Analyses include the determinations of pH and conductivity at 25 °C and principal ion concentrations (Cl^-, NO_3^-, SO_4^{2-}, Na^+, NH_4^+, K^+, Mg^{2+}, Ca^{2+}) by ion chromatography with electrochemical eluent suppression.

Table 4. Parameters of the EUSAAR-2 analytical protocol

Fraction Name	Plateau Temperature (°C)	Duration (s)	Carrier Gas
OC 1	200	120	He 100%
OC 2	300	150	He 100%
OC 3	450	180	He 100%
OC 4	650	180	He 100%
cool down		30	He 100%
EC1	500	120	$He:O_2$ 98:2
EC2	550	120	$He:O_2$ 98:2
EC3	700	70	$He:O_2$ 98:2
EC4	850	110	$He:O_2$ 98:2

Source: JRC, 2015

4.2.3   On-line data acquisition system/data management

4.2.3.1. Data acquisition for aerosol and meteorological variables

The JRC air pollution observatory Data Acquisition System (DAS) is a specifically tailored set of hardware and software developed for the Air and Climate unit to operate instruments, acquire both analogue and digital output from instruments and store pre-processed measurement data into a database for further off-line evaluation. The DAS operated and controlled the instrumentation during 2021. The new FDMS-TEOM 1405-F was inserted in the DAS in 2018. The new CAPS was inserted in the DAS in October 2019.

Since March 2018, the software environment of the DAS is Labview 2016 v16.0 (32 – bit) from National Instruments and the database engine for data storage is Microsoft SQL Server v18.4. The data acquisition computer was also upgraded to Windows 10.

The DAS is designed to continuously run the following tasks:

- Start of the data acquisition at a defined time (must be full hour);
- Choose the instruments that have to be handled;
- Define the database path where data will be stored primary in LAKE3 and secondary locally on the acquisition machine;
- Define the period (10 minutes currently used) for storing averaged data, this is the data acquisition cycle time;
- Obtain data (every 10 seconds currently set) for all selected instruments within the data acquisition cycle:
    - Send commands to query instruments for data or keep listening to the ports for instruments that have self-defined output timing (Aethalometer and DMPS);
    - Scan instruments outputs to pick out the necessary data;
- Calculate average values and standard deviations for the cycle period;
- Query instruments for diagnostic data (when available), once every 10 minutes;
    - Store all data in a database with the timestamp of their respective measurement for Aethalometer and DMPS
    - And with the DAS time stamp for all other instruments.

The following instruments are managed with the DAS (Fig. 13), using 3 computers (currently called EMEP DMPS-A, Emepacq5 and MeteoPrecipitation):

- EMEP DMPS-A:
    - Number size distribution for particles diameter <0.800 μm
- Emepacq5:
    - Number size distribution for particles diameter >0.500 μm, APS
    - PM10 mass concentration, TEOM FDMS
    - Aerosol light absorption, Aethalometer

Fig. 14. Set-up of the Data Acquisition System in the Reactive Gases Laboratory
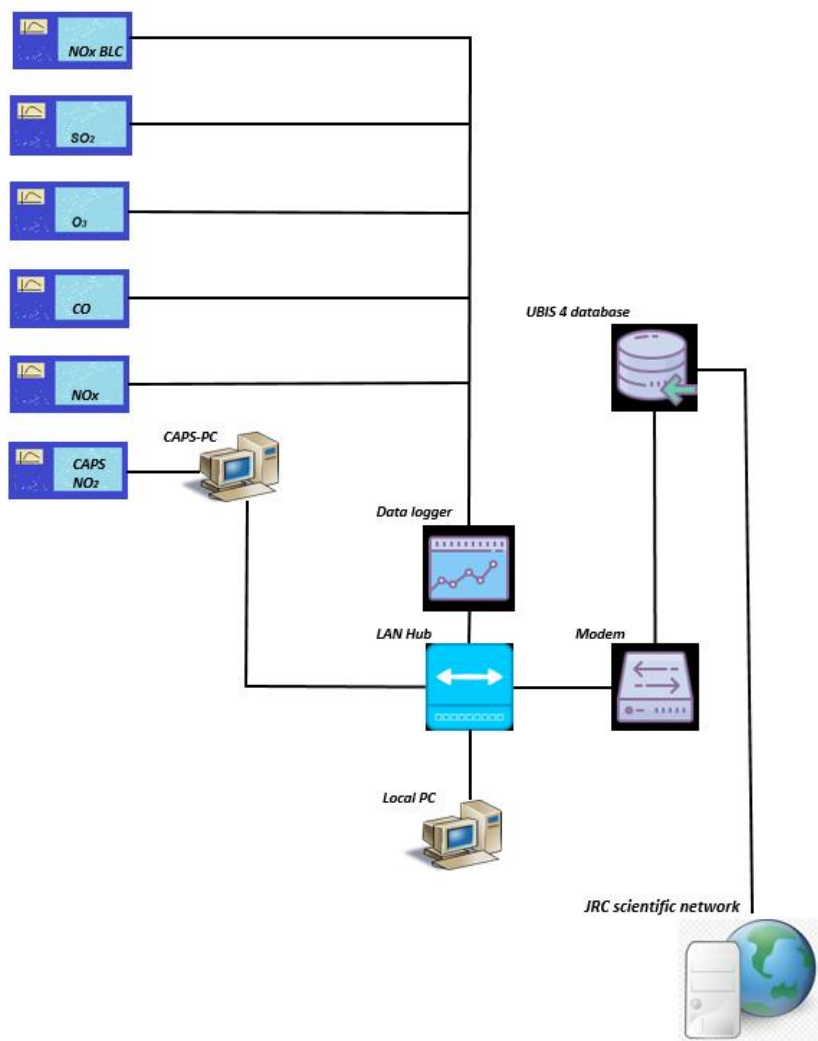
Source: JRC, 2019

Fig. 15. New Graphic user interface of the EMEP-GAW station data evaluation software, used to reprocess the CAPS-SSA data, from October 2019.
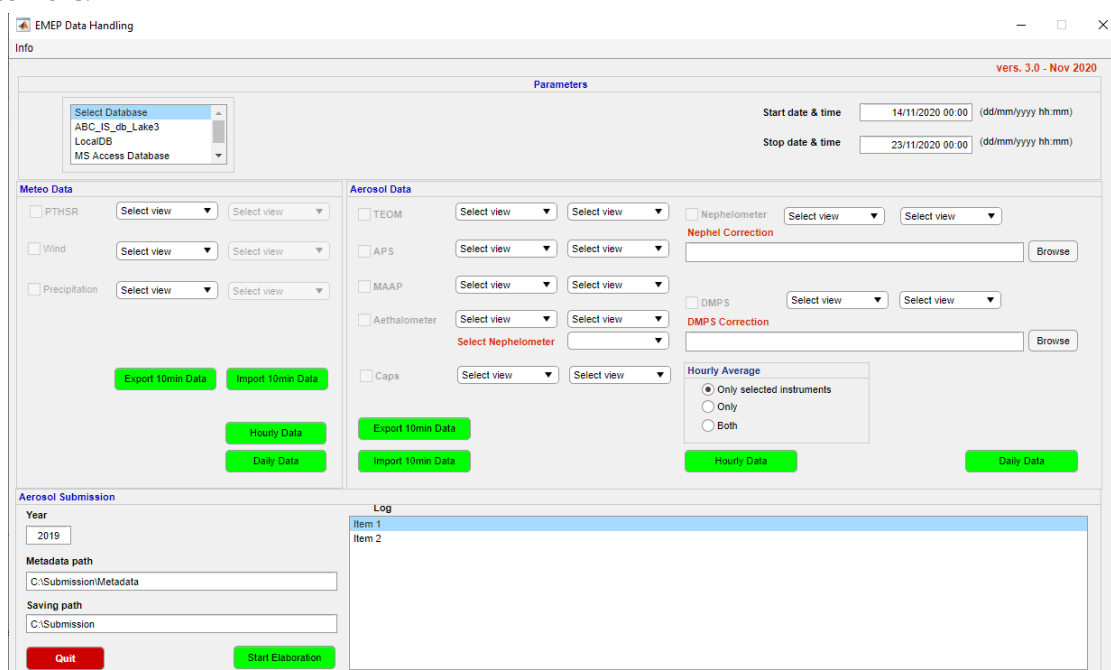
Source: JRC, 2020

- Aerosol light absorption, MAAP
- Aerosol light scattering, Nephelometer
- Aerosol light extinction and scattering, CAPS$_{SSA}$

- MeteoPrecipitation:
- Solar radiation
- Weather transmitter (temperature, pressure, relative humidity, wind speed and direction, precipitation)
- Precipitation data

The data acquired are stored in a Microsoft SQL Server database (DB) on the central database **abc-is_db** hosted on the pc **Lake3.** If the local network is not available, data are stored in a local database on the acquisition pc itself. Each pc also has software for the synchronisation of **abc-is_db** with **local db.**

The acquisition time is manually synchronised for all PCs and is kept at UTC, without adjustment for summer/winter time. Data are collected in a data base called **abc-is_db** that runs on the **acquisition DB server Lake3.**

The station web site (https://abc-is.jrc.ec.europa.eu/), runs over three machines, the acquisition DB server Lake3, the production DB server and the Web server in the DMZ (demilitarized zone).

Lake3 receives the data from the laboratory network container and performs a real time Data Base Replica of the relevant data on the production DB server.

The production Web server hosts the site https://abc-is.jrc.ec.europa.eu and makes the data in the production DB server available on the internet. In the web site the projects to which ABC-IS contributes and contact persons can also be retrieved.

The Life cycle data sheets are currently in the network share driver Laboratories, the data in this network storage is backup protected.

4.2.3.2. Data acquisition for reactive gases

All analysers measuring reactive gases connect via serial or analogue signals to a data logger and data are transmitted via router to a database operated by AIP (UBIS4). Online access to the database allows data verification, correction, reporting and/or downloading. Further, the database launches automatic daily zero/span checks (Fig. 14).

4.2.4   Data evaluation

The structured data evaluation system (EMEP_Main.m) with a graphic user interface (Fig. 15) has been used with Matlab Release R2016a (www.mathworks.com) as the programming environment.
The data evaluation is now done with the "EMEP_Data_Handling L0 to L2" v. 1.9.9.8 - Nov 2017. Not evaluated 10 min data (flagged 3) is now exported to several excel sheets.
After a preliminary data analysis, these data are flagged according to the flags listed below. These files including flags are then imported into the database (level 1 data, 10 min corrected). Finally, the hourly and the daily data averages are calculated taking into account the flagging.

0	1	2	3	5	6	7	9
Good data – used	Good data – not used	Calibration	Not yet evaluated	Questionable	Local contamination	Erroneous data	No data

To check these data and to exclude outliers for all other measurements, a visual inspection of the 10 min data is performed.
All database connections are implemented via ODBC calls (Open DataBase Connectivity) to the corresponding Microsoft SQL Server v13.0.1742.0.
Daily averages (8:00 < t ≤ 8:00 +1 day) of all variables and parameters stored in the hourly averages database can be calculated and are subsequently stored in a separate Microsoft SQL Server v13.0.1742.0 database. The CAPS-SSA Data Evaluation with Matlab has been performed since 16 October 2019.

Fig. 16. EMEP inter-laboratory comparisons for rainwater analyses (1987-2021): JRC-Ispra results.
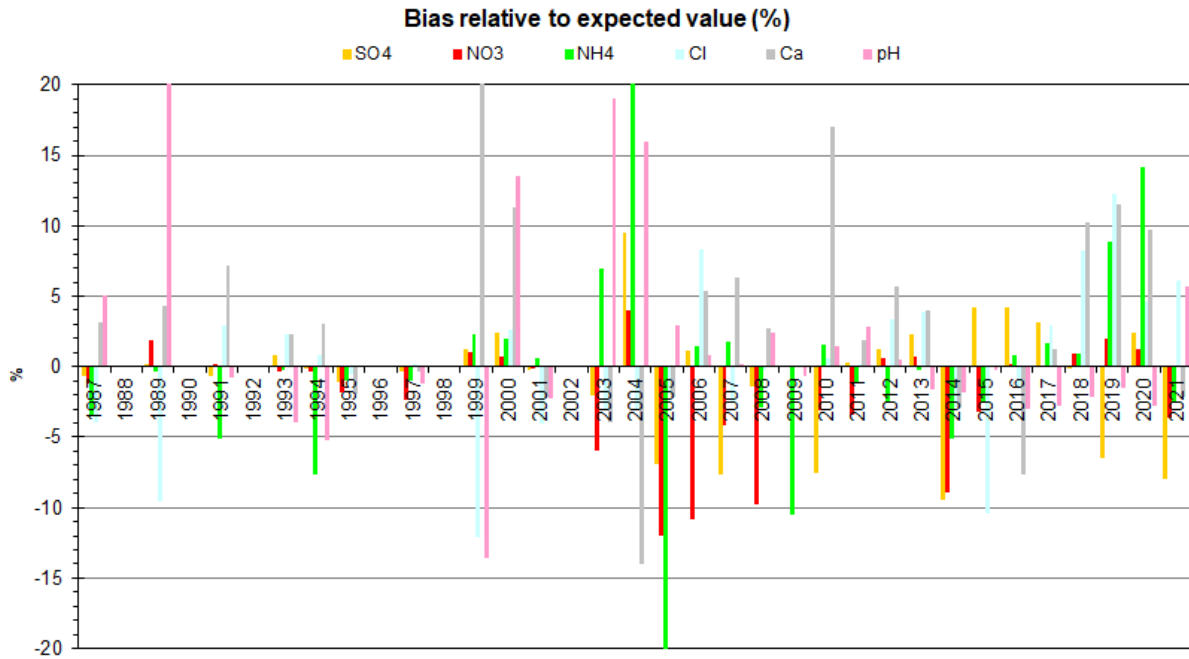
Source: JRC, 2022

Fig. 17. JRC-Ispra instrument's (#30) performance for the determination of (top) total carbon (TC) and (bottom) elemental carbon (EC/TC ratio) during the ACTRIS inter-laboratory comparison OCEC-2021-1.

Source: JRC, 2022

33
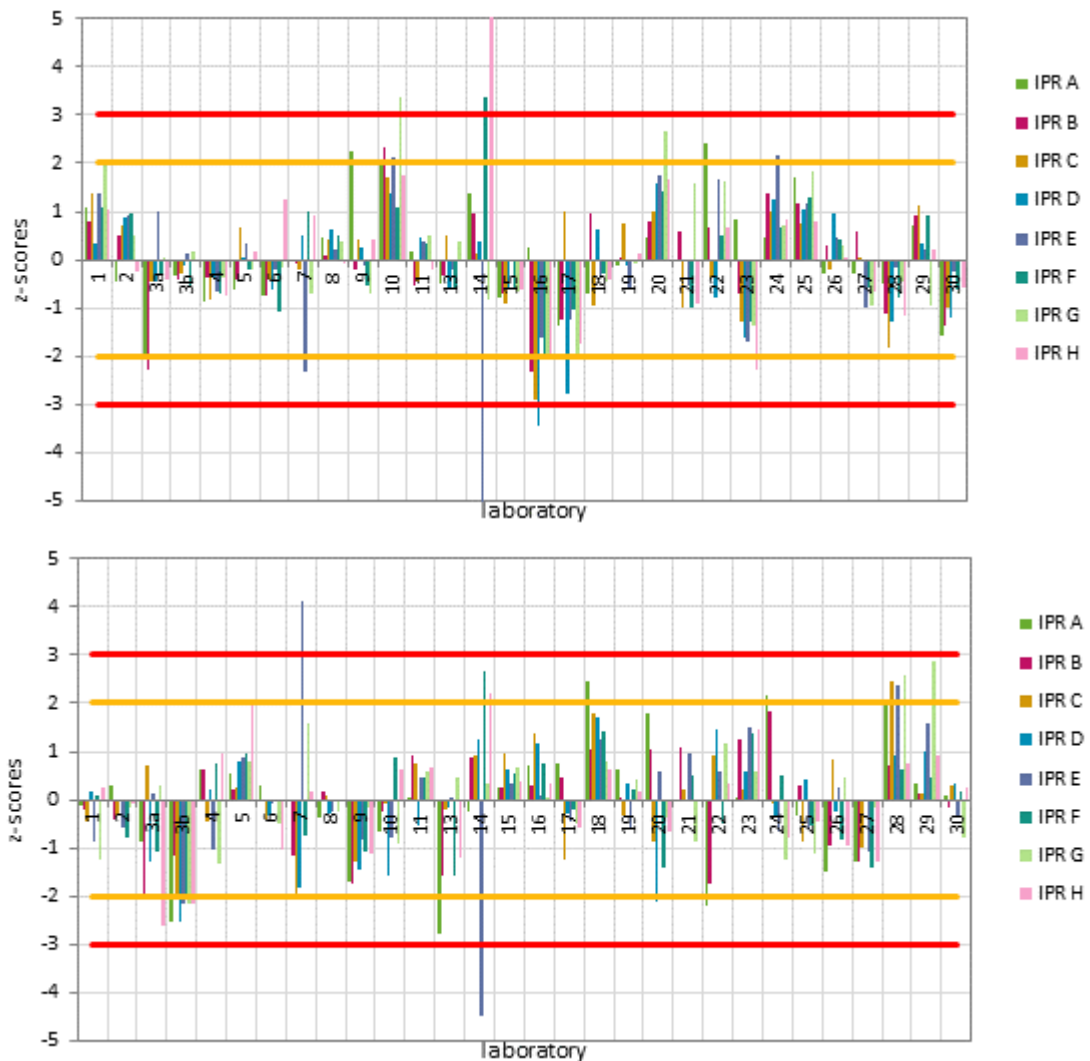
4.3   Quality assurance

At JRC level the quality system is based on the Total Quality Management philosophy, the implementation of which started at the Air and Climate Unit in December 1999. We have been working under ISO 9001 and ISO 14001 since 2010 (more information can be found in the chapter "Quality management system").

The JRC-Ispra station for atmospheric research did not renew the accreditation for the monitoring of SO_2, NO, NO_2 and O_3 under EN 45001 obtained in 1999 for lack of human resource. However, measurements and standardised operating procedures are based on recommendations of the EMEP manual (1995, revised 1996; 2001; 2002; 2014), WMO/GAW 227, ISO and CEN standards. In 2021 the gas phase monitors were verified daily by an automatic zero/span check. Furthermore, analysers were regularly controlled by the European Reference Laboratory for Air Pollution (ERLAP). This includes, next to annual preventive maintenance, calibration with traceable working standards (three times a year), linearity checks and gas phase titration (for NO_x), and the re-certification of working – standards with primary reference material (PRM) allowing full traceability to SI units. ERLAP's accreditation (ISO 17025) was achieved in 2013 and was confirmed in 2021.

For on-line aerosol measurements, ACTRIS Standard Operating Procedures and QA/QC requirements are followed. Those involve station audits, side by side instrument comparisons at the world calibration centre for aerosol physics (WCCAP) in Leipzig (DE), and specific QC measurements. The station was favourably audited by Dr. T. Tuch (WCCAP) on 22-24 March 2010 under the EUSAAR project (www.eusaar.net), as described in a specific report. JRC's integrating nephelometer (report-IN-2019-1-2) and absorption spectrometers (report-AP-2019-2-2 and report-AP-2019-2-3) successfully took part in side by side comparisons at the WCCAP in June 2019. The Condensation Particle Counters used as parts of our Differential Mobility Particle Sizer were also both successfully checked at the WCCAP in June 2019 (see report-MPSS-2019-3-4 at the ACTRIS-ECAC web site). Due to the COVID lockdowns and refurbishing of the WCCAP, there were no calibration workshops in 2020 - 2021.

The aerosol LiDAR was successfully audited and on-site compared with an ACTRIS reference instrument during the period 17 – 27 July 2018. The system alignment is checked for each measurement through its calibration in a particle–free region of the atmosphere. Quality check measurements are reported at least once a year to the ACTRIS Centre for Aerosol Remote Sensing (CARS), which produces a detailed report on the instrument performance. In 2021, QC measurements were performed on 28 February, and analysed by 25 March (syncandshare.lrz.de/folderstable).

Ion analysis quality was checked as part of the 39th annual EMEP inter-laboratory comparison (Fig. 16). In this exercise, all ion measurements in the rain water synthetic samples provided by NILU passed the quality test (S) but 2 SO_4^{2-} measurements (both 15% too low). The data quality objective within EMEP is ±10% accuracy or better for NO_3^- and SO_4^{2-} and ±15% accuracy or better for other components for each sample. Conversely, rain acidity and conductivity measurements were all too low (U) with deviations to the assigned values of about a factor of 2. Therefore, both the pH and conductivity probes were substituted.

The inter-laboratory comparison for organic and elemental carbon analyses organised under the project ACTRIS-IMP in 2021 indicates no significant bias for the determination of total carbon and elemental carbon compared to the robust average among the participants (Fig. 17).

Data quality is also checked whenever possible through comparison among various instruments, mass closure (for PM) and ion balance (for precipitation) exercises (see specific sections).

Fig. 18. Solar total radiation, precipitation amount, and temperature monthly values observed at the Atmospheric Observatory in Ispra in 2021, compared to the 1990-2010 period ± standard deviations.
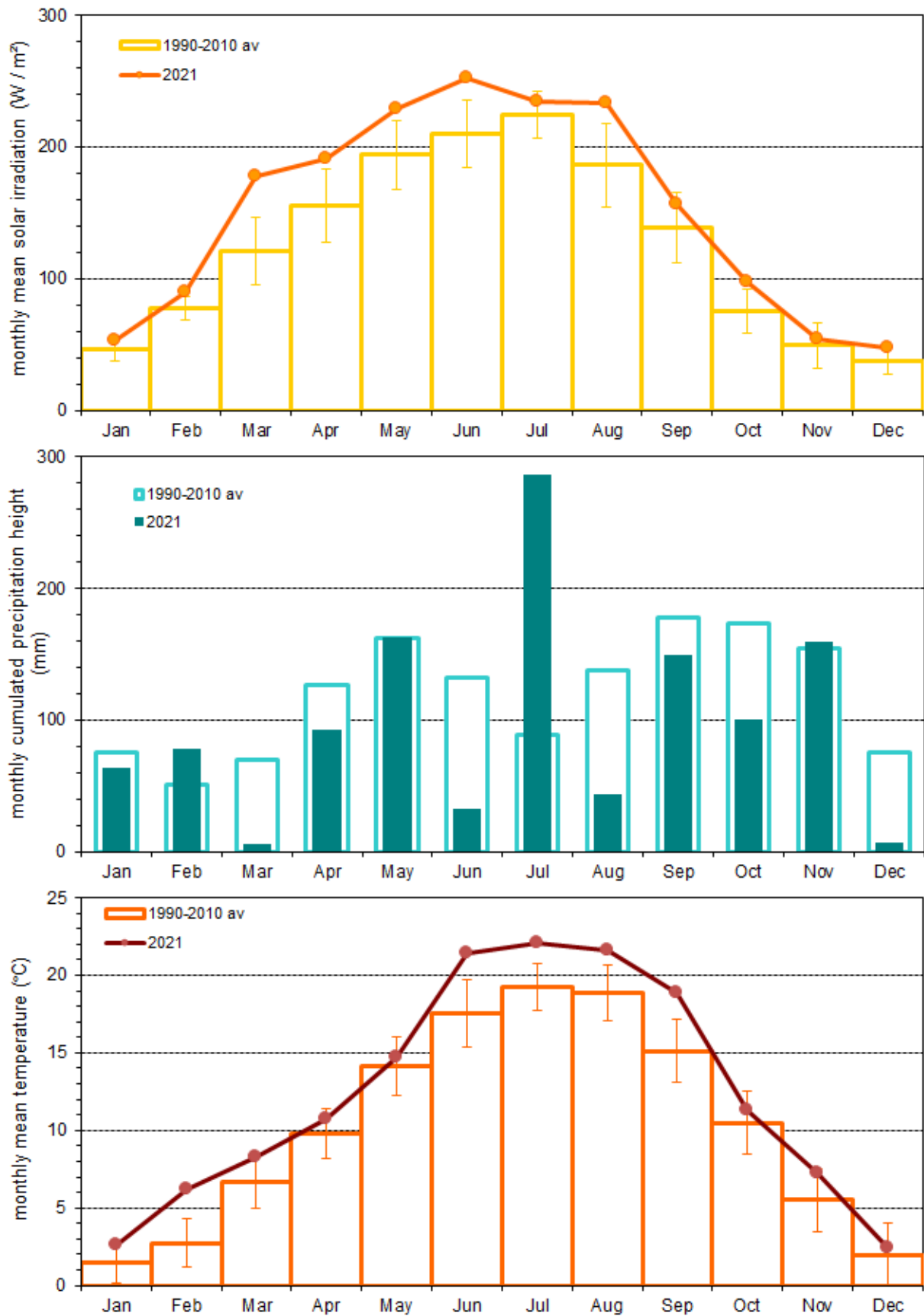
Source: JRC, 2022

4.4   Results for the year 2021

Year 2021 air pollution data have to be looked at considering weather conditions (Fig. 18) and human activity data, still possibly affected by COVID-19 epidemic waves. Comprehensive activity data are not fully available yet, but mobility data for the Piedmont and Lombardy regions can be used as an indicator (Ispra being located close to the border). The driving route request indices delivered by *Apple®* (covid19.apple.com/mobility) compare daily numbers of requests made on the Apple Maps application in a given area on any day with the number of requests made on 13 January 2020 in the same area (index 100). These data suggest reduced mobility across winter 2020 – 2021, and perhaps till June 2021, although indices as low as in March – April 2020 (lockdown) are never reported in 2021 (Fig. 19).

Fig. 19. Mobility data (driving route requests) from Apple® for Piedmont and Lombardy in 2020 -2021. Index 100 corresponds to 13 January 2020 data.
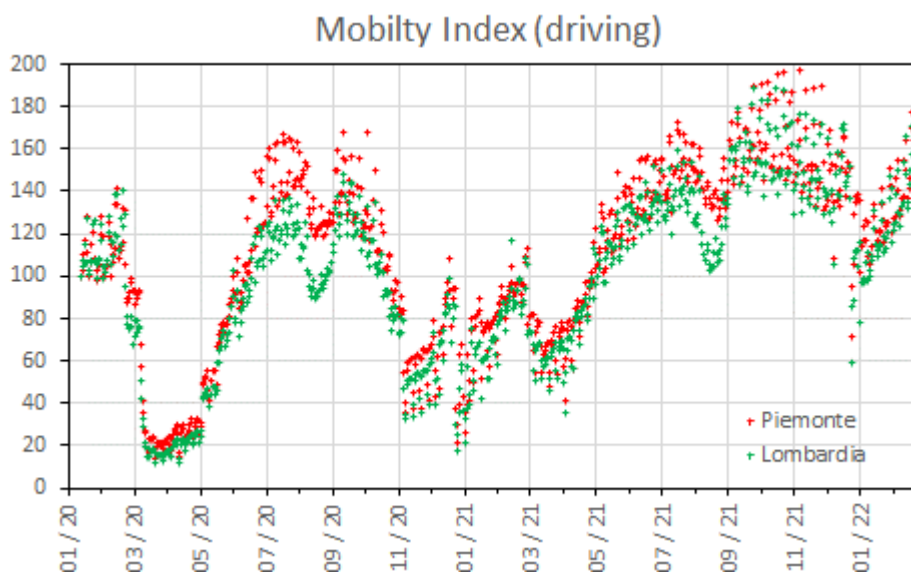
Source: Apple® 2022, data analysis: JRC, 2022

4.4.1   Meteorology

Meteorological data (Fig. 18) were acquired using a Pyranometer (solar radiation) and a weather transmitter (T, P, RH, precipitation) located at 9 m above the ground at the Atmospheric Observatory, respectively. Meteorological data cover the whole of 2021 except for 2 main gaps (1-3 January, 6 June) filled with data from JRC Building 51.

The monthly mean solar radiation was significantly greater than average roughly from March to August. February and warm months (June to September) were also significantly warmer in 2021 compared to the reference period (1990 – 2010). March, June, August and December were particularly dry, while July was exceptionally wet. The total yearly rainfall was 1180 mm, i.e. quite less than the 1990-2010 average (1423 mm).

Fig. 20. Seasonal variations of the 24 hr averaged concentrations of SO_2, CO, NO_2, NO, O_3 and NO_x in 2021 (thin lines) and 1990-2010 monthly averages (thick lines: yellow=SO_2, blue=CO, green=NO_2, orange=O_3). Concentrations are in EMEP standard conditions (1013 hPa, 293K).
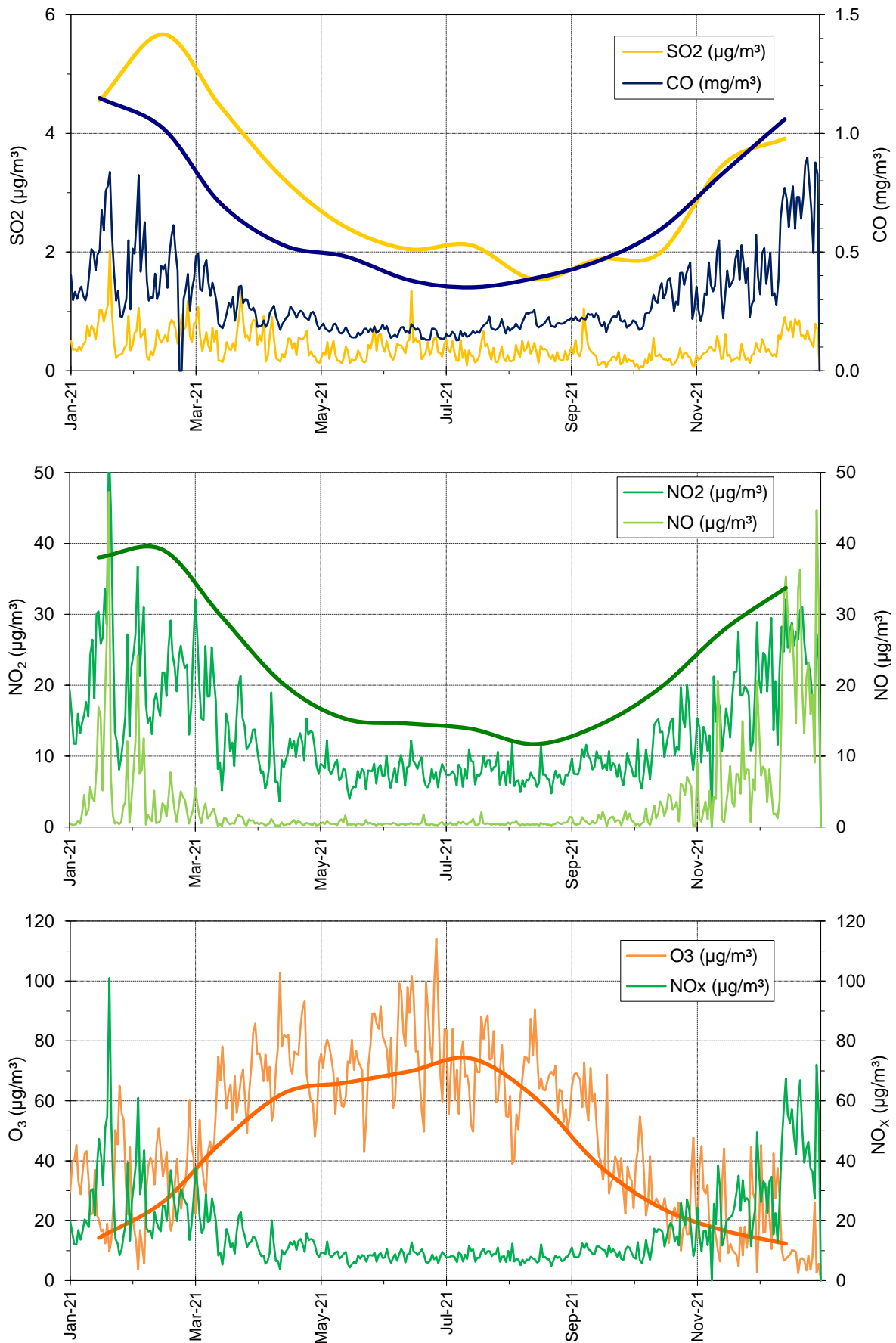
Source: JRC, 2022

4.4.2   Gas phase air pollutants

SO_2, CO, NOx and O_3 were measured continuously at the Atmospheric Observatory during the year 2021, with no significant gap (data coverage ≥ 99%). Expanded uncertainties for the measured concentrations were calculated to be 3.7% + 0.7 ppb for SO_2, 7.2% + 0.07 ppm for CO, 8.5% + 0.5 ppb for NO, 6.2% +1.8 ppb for NO_2 and 4.4% +0.7 ppb for O_3, which is in line with the *European Directive 2008/50/EC* (less than 15 % at the limit value). To render the time series more representative of regional background conditions, hourly SO_2, CO, NOx and O_3 data were flagged for local contamination (about 1% of all valid data points), and daily averages were computed excluding the data points for which local contamination was identified.

In 2021, the seasonal variations in SO_2, NO, NO_2, NO_x and O_3 were similar to those observed over the 1990-2010 period (Fig. 20). Concentrations are generally highest during wintertime for primary pollutants (SO_2, CO, NO_x), and in summertime for O_3. Higher concentrations of SO_2, CO, NO_x in winter result mainly from a lesser dispersion of pollutant during cold months (low boundary layer height and stagnant conditions), whereas the high concentration of O_3 during summer is due to enhanced photochemical production.

SO_2 concentrations (average = 0.4 μg/m³) were in 2021 the smallest ever observed, about 20% less than in 2020, 40 % less than across 2017-2019, and 7 times less compared to the reference period (1990-2010).

Daily mean CO concentrations ranged from 0.13 to 0.9 mg m^{-3} (0.1 – 0.8 ppmv), which are typical values at a regional background station like the Atmospheric Observatory in Ispra. CO annual average was 4 % less than in 2020, and less than half the values observed in the 1990-2000's.

NO concentrations (average = 3.5 μg m^{-3}) were 9 % less than in 2020, and 10 % less than in 2017-2019. In 2021, data filtering for local contamination affected the NO annual mean concentration by -0.4 μg m^{-3}.

NO_2 concentrations (annual average = 13 μg m^{-3}) were the lowest ever observed (1 % less than in 2020) They were 20 % less than across 2017-2019 and 40% less than across 1990-2010.

These data show that annual mean concentrations of gaseous primary pollutants were slightly to significantly less than in 2020, during which some polluting activities were reduced due to the COVID-19 measures in March-April and November - December. Low gaseous primary pollutant concentrations observed in 2021 could also reflect reduced human activities related to COVID-19 epidemic waves in January – April 2021.

NH_3 daily mean concentrations (Fig. 21) ranged between 1.2 and 17 μg m^{-3} (1.7 to 24 ppb) and between 0.6 and 11 μg m^{-3} (0.8 to 16 ppb) at 10 m and 100 m above ground level, respectively. Annual means were 4.7 and 3.5 μg m^{-3} at 10 m and 100 m above ground level, respectively, i.e. 10-20% greater than in 2020, during which measurements were performed from July to December only.

Fig. 21. Seasonal variations of the 24 hr averaged concentrations of NH_3 at 10 m and 100 m above ground level in 2021. Concentrations are in EMEP standard conditions (1013 hPa, 293K).
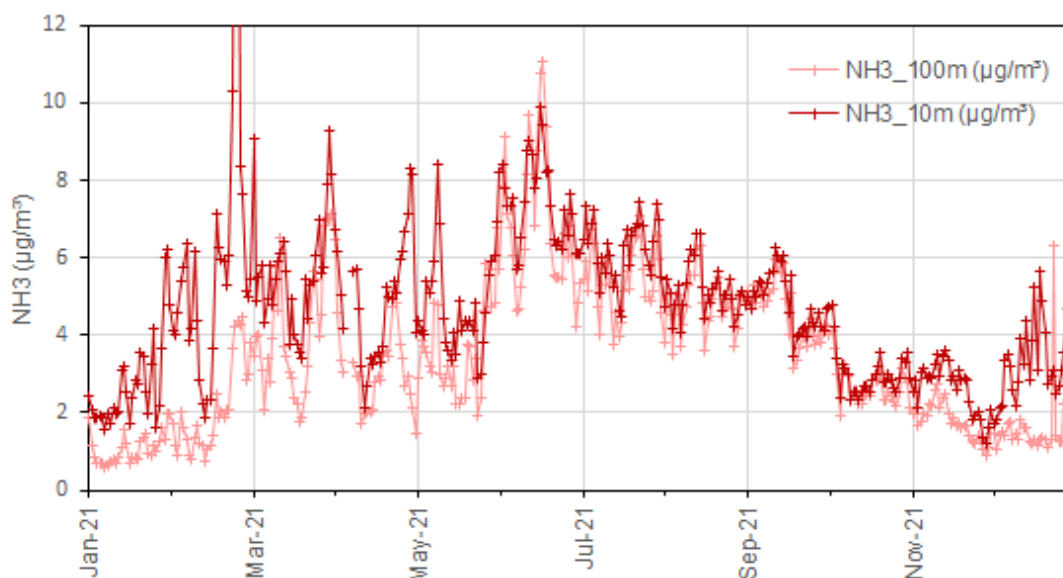
Source: JRC, 2022

Fig. 22. AOT 40 (ppb h), SOMO35 (ppb day) and number of exceedances of the 1hr-averaged 180 μg/m³ threshold in 2021 (bars). Lines show values for the reference period 1990-2010.
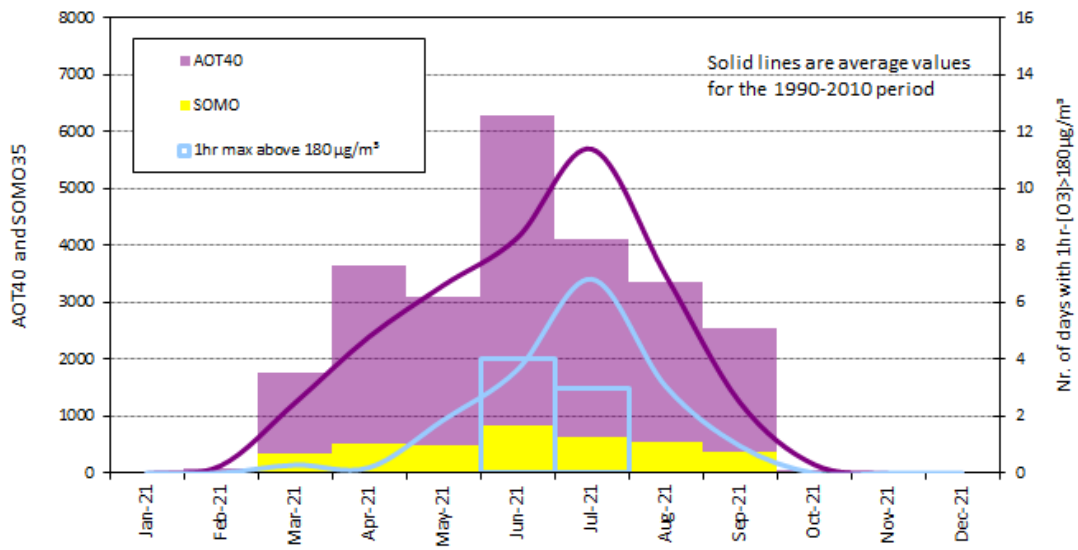
Source: JRC, 2022

Fig. 23. 24hr-integrated PM$_{2.5}$ mass concentrations from off-line gravimetric measurements at 20% RH and chemical determination of main constituents in 2021.
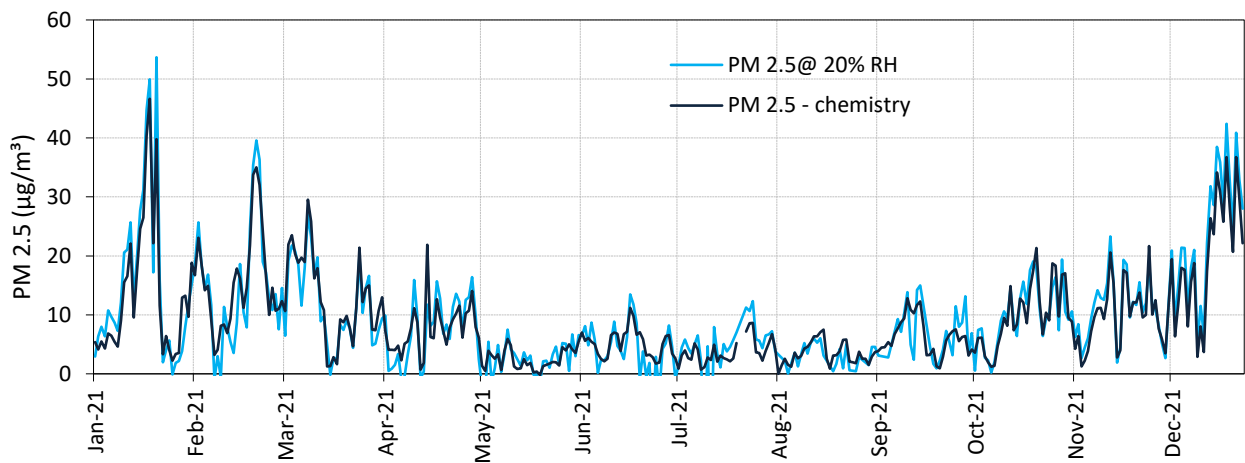
Source: JRC, 2022

Fig. 24. Regressions between the gravimetric PM$_{2.5}$ measurements at 20 % RH and the sum of PM$_{2.5}$ chemical constituents (left), and the FDMS-TEOM PM10 measurements (right) in 2021. Orange symbols correspond to desert dust outbreaks.
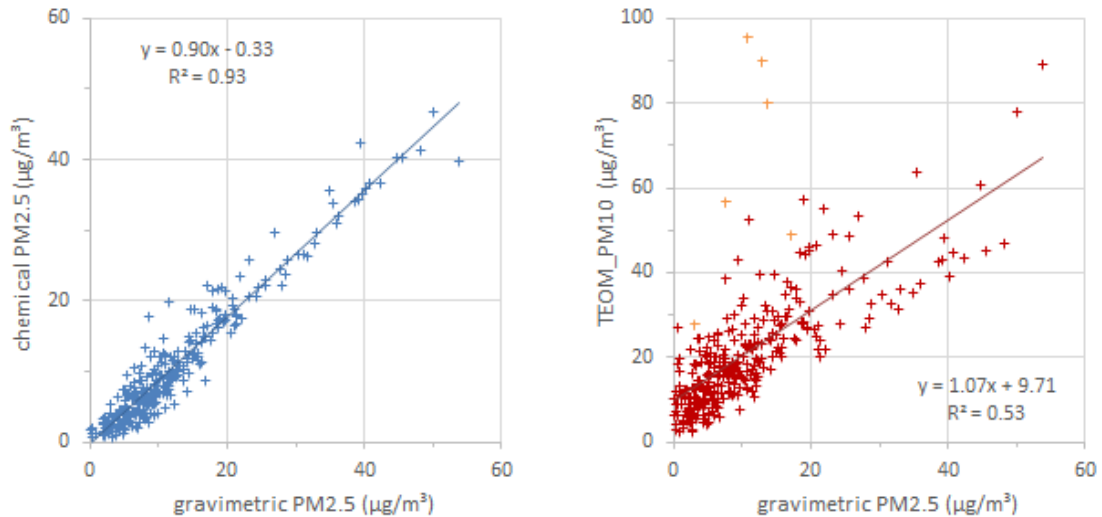
Source: JRC, 2022

Due to the exceptionally good O_3 data coverage in 2021 (99.7%, not 1 single full day missing), O_3 indices were calculated from measurement data only (no gap filling). The annual mean O_3 concentration in 2021 (49 µg m^{-3}, 25 ppb) was 7% greater than in 2020, and 6% less than in 2017-2019, still in line with the relatively high O_3 concentrations observed since the early 2010's. Fig. 22 shows that high annual O_3 indices in 2021 were mainly due to exceptionally high O_3 levels in June, and to a lesser extent in April. High mean solar radiation and temperature in June probably played a role.

The vegetation exposure to above the ozone threshold of 40 ppb (AOT 40 = Accumulated dose of ozone Over a Threshold of 40 ppb, usually used for "crops exposure to ozone") was 24970 ppb h (Fig. 22), i.e. 0.7% more than in 2020, 25 % less than across 2017-2019, but very similar to the 2010's average value.

For quantification of the health impacts (population exposure), the World Health Organisation uses the SOMO35 indicator (Sum of Ozone Means over 35 ppb, where "means" stands for maximum 8-hour mean over day), i.e. the accumulated ozone concentrations dose over a threshold of 35 ppb (WHO, 2008). In 2021, SOMO35 was 3790 ppb day (Fig. 22), again 0.7% less than in 2020, and also 28% lower than in 2017-2019 (5290 ppb day on average) but similar to the mean 2010s' value (3910 ppb day).

We observed 7 extreme O_3 concentration events (>180 µg m^{-3} over 1 hour) in 2021, to be compared with 1, 4, 11, and 0 extreme events in 2020, 2019, 2018, and 2017, respectively. The value 180 µg m^{-3} over 1 hour corresponds to the threshold above which authorities have to inform the public (European Directive 2008/50/EC). During the reference period 1990-2010, the information level of 180 µg m^{-3} was exceeded 17 times per year on average. The other "protection of human health factor" mentioned by the European Directive 2008/50/EC (120 µg m^{-3} as maximum daily 8-hour average) was exceeded 48 times in 2021 (vs 68 times in 2020, 73 times in 2019, 117 times in 2018, and 5 times in 2017), leading to a 3-year average of 63 exceedances per year, well above the Air Quality Directive limit value (25 exceedances per year).

In short, O_3 concentrations were on average 7% greater in 2021 compared to 2020, but two main indicators (AOT 40 and SOMO 35) were almost unchanged. The number of exceedances of the 120 µg m^{-3} daily maximum was less in 2021 than in 2020, but the number of pollution peaks (above 180 µg m^{-3}) was much greater.

4.4.3 Particulate phase

4.4.3.1 Particulate matter mass concentrations

The equipment used to collect PM$_{2.5}$ was erroneously operated with a PM1 inlet from 1 May to 7 September 2021. Furthermore, the quartz fibre filters used for PM$_{2.5}$ sampling (Pallflex TissueQuartz 2500 QAT-UP) used from 2021 have much more fragile edges, probably related to the industrial process used to cut them. As a consequence, 54 gravimetric analysis results had to be discarded for inconsistency with other measurements. Therefore, PM$_{2.5}$ concentration statistics are not as robust as for previous years. In 2021, PM$_{2.5}$ gravimetric measurements at 20 % relative humidity (data coverage=81%) averaged 11.6 µg m^{-3} (Fig. 23). Corrections based on particle volume size distribution measurements (Section 4.4.3.4) would lead to an annual average of 12.1 µg m^{-3}. Both estimates are less than the 2020 average (13.5 µg m^{-3}), less than the 2017-2019 average (14.2 µg m^{-3}), and well below the European annual limit value of 25 µg m^{-3} to be reached by 2015 (European directive 2008/50/EC). Note that the 2021 annual value could be the lowest record since this measurement was started in 2002, but various technical issues occurring in 2021 could have biased downwards these measurements.

Gravimetric measurements of PM$_{2.5}$ mass at 20% RH and the sum of PM$_{2.5}$ mass constituents determined from chemical analyses are quite well correlated (Fig. 24). The slope (0.93) is the same as in 2019-2020, and the intercept (-0.33) is significantly negative, as observed in 2018 - 2020 but not for previous years.

The regression between PM$_{10}$ FDMS-TEOM and gravimetric PM$_{2.5}$ measurements for 2021 (Fig. 24) indicates a marginal correlation between these measurements, affected by the greater uncertainties in gravimetric analyses and by Saharan dust outbreaks (23-27 February, 20-21 June, 15-16 August) leading to most extreme points in the regression (orange symbols). The intercept of 9.7 µg/m³ suggests an offset in FDMS-TEOM measurements, negative sampling artefacts related to the quartz fibre filters used to collect PM$_{2.5}$, or a combination of both.

Fig. 25. 24-hr integrated concentrations of the main PM₂.₅ constituents in 2021, and the relative unaccounted fraction.
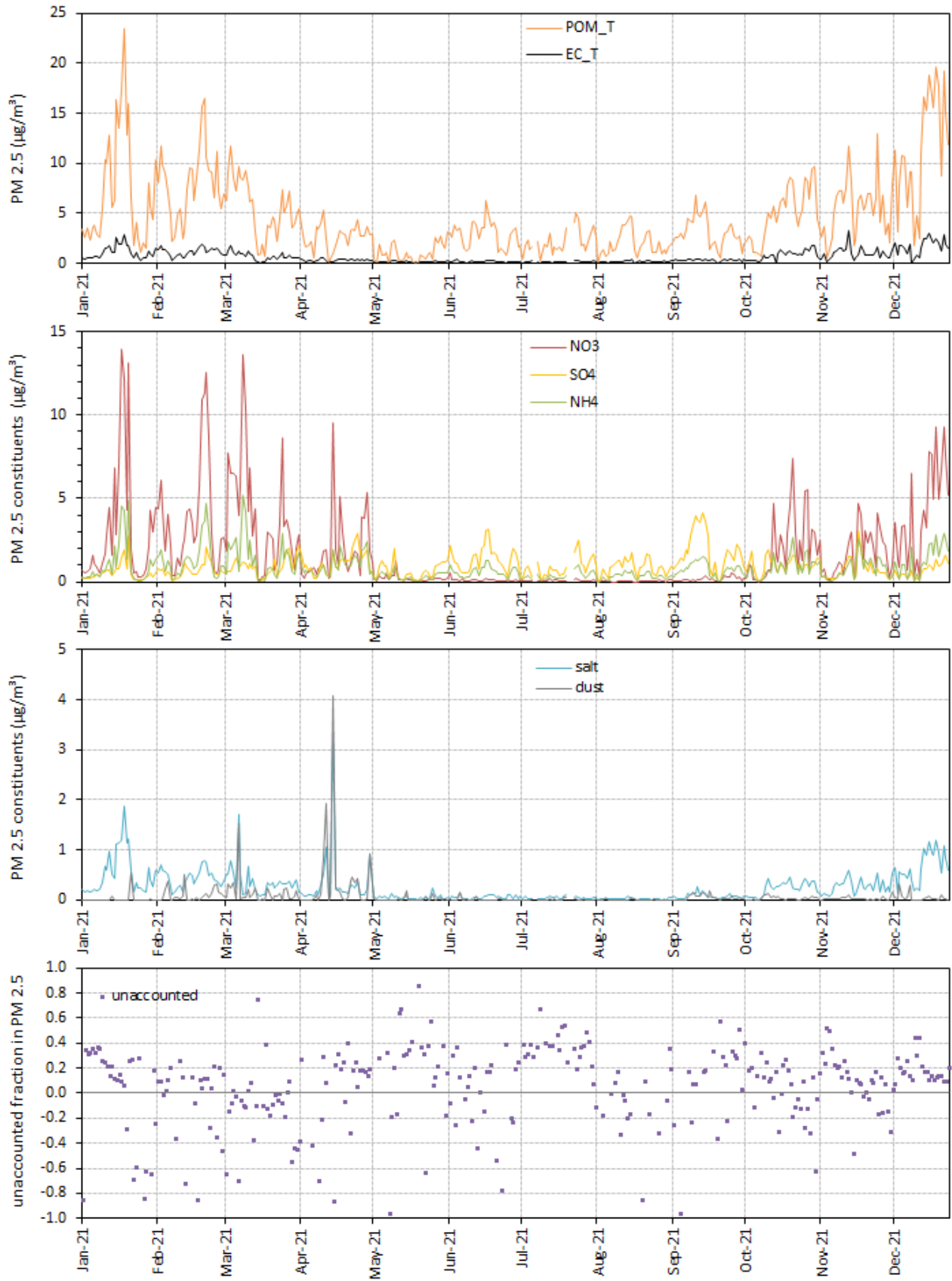
Source: *JRC, 2022*

In 2021, the annual data coverage for the FDMS-TEOM measurements of PM_{10} was 99%. The number of exceedances of the 24-hr limit value (50 μg m^{-3}) observed in 2021 (12) was less than in 2020 (26) and in 2017-2019 (28 on average), as well as below the limit value (35) indicated in the European directive 2008/50/EC, despite the contribution of 5 natural dust outbreaks.

The 2021 annual PM_{10} average (19.9 μg m^{-3}) was less than in 2020 (22.8 μg m^{-3}) and in 2017-2019 (24.9 μg m^{-3} on average), and well below the annual limit value (40 μg/m³) stated in the European directive 2008/50/EC.

4.4.3.2 $PM_{2.5}$ chemical composition

Main ions (Cl$^-$, NO$_3^-$, SO$_4^{2-}$, Na$^+$, NH$_4^+$, K$^+$, Mg^{2+}, and Ca^{2+}), OC and EC were determined from the quartz fibre filters collected for PM mass concentration measurements for the whole of 2021 (data coverage = 99%).

Fig. 25 shows the temporal variations in the $PM_{2.5}$ main components derived from these measurements. Particulate organic matter (POM) is calculated by multiplying OC (organic carbon) values by the 1.4 conversion factor to account for non-C atoms contained in POM (Russell et al., 2003). "Salts" include Na$^+$, K$^+$, Mg^{2+}, and Ca^{2+}. Dust is calculated from Ca^{2+} concentrations and the regression (slope = 4.5) found between ash and Ca^{2+} in the analyses of ash-less cellulose filters (Whatman 40) in previous years. Most components show seasonal variations with higher concentrations in autumn and winter, and lower concentrations in summer, like $PM_{2.5}$ mass concentration. This is mainly due to changes in pollutant horizontal and vertical dispersion, related to seasonal variations in meteorology (e.g. lower boundary layer in winter). The magnitude of the POM, NH$_4^+$ and NO$_3^-$ seasonal cycles may be enhanced due to equilibrium shifts towards the gas phase, and/or to enhanced losses (negative sampling artefact) from quartz fibre filters during warmer months. Indeed, historical data (May – Sept. 2013) show that the concentration of NH$_4$NO$_3$ in $PM_{2.5}$ determined from filters can be 1/5 of the concentration measured in the submicron aerosol with an Aerosol Chemical Speciation Monitor (see 2013 annual report).

NH$_4^+$ and NO$_3^-$ + SO$_4^{2-}$ were very well correlated as indicated by the regression shown in Fig. 26. This correlation results from the atmospheric reaction between NH$_3$ and the secondary pollutants H$_2$SO$_4$ and HNO$_3$ produced from the oxidation of SO$_2$ and NO$_x$, respectively. The ratio between NO$_3^-$ + SO$_4^{2-}$ and NH$_4^+$ was close to 1, which means that sufficient NH$_3$ was available in the atmosphere to neutralise both H$_2$SO$_4$ and HNO$_3$. These measurements suggest that on average $PM_{2.5}$ aerosol was not much acidic. NB: the 3 data points showing a large excess of nitrate plus sulfate do not correspond to desert dust outbreaks.

Fig. 26. SO$_4^{2-}$ + NO$_3^-$ vs. NH$_4^+$ (μeq/m³) in $PM_{2.5}$ for 2021
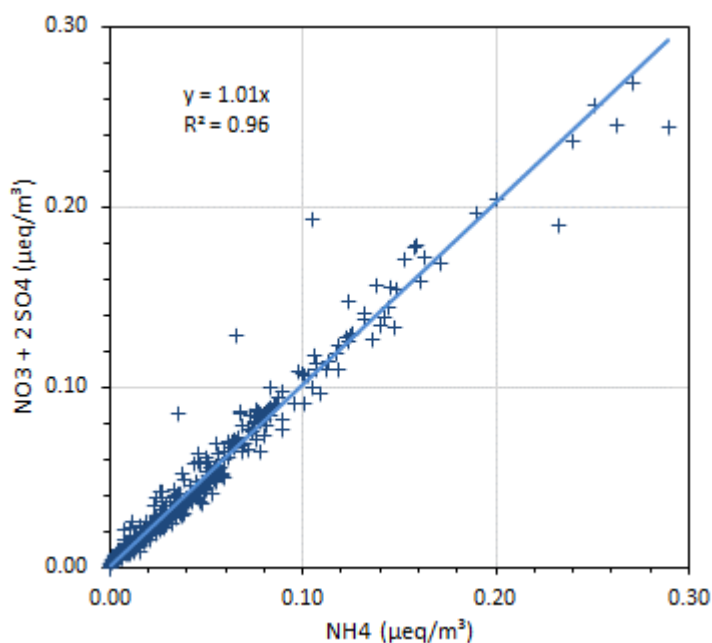
Source: JRC, 2022

Fig. 27. Average composition of PM$_{2.5}$ in 2021 for days on which PM$_{2.5}$ > 15 µg/m³ (top) and PM$_{2.5}$ < 10 µg/m³ (bottom), during cold months (Jan., Feb., Mar., Nov., Dec.) and warmer months (Apr. – Oct.).

Mean PM2.5 chemical composition for PM2.5 > 15 µg/m³

cold months, 65 days   warm months, 11 days

Mean PM2.5 chemical composition for PM2.5 < 10 µg/m³

cold months, 47 days   warm months, 112 days
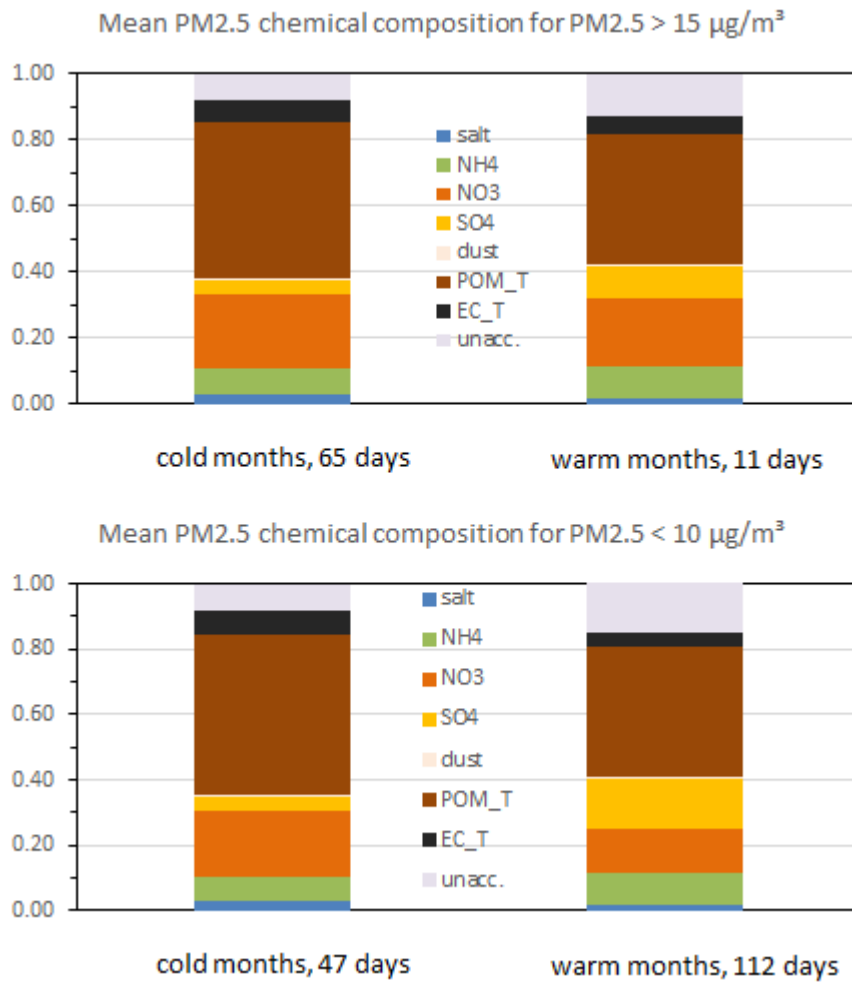
Source: JRC, 2022

4.4.3.3 Contribution of the main aerosol constituents to PM$_{2.5}$

The contributions of the main aerosol constituents to PM$_{2.5}$ are presented in Table 5 (annual averages) and in Fig. 27 (a) for days on which the future "24-hr limit value for PM$_{2.5}$ of 15 µg/m³ was exceeded" during the cold months (Jan., Feb., March, Nov. and Dec., 65 cases) and the warm months (Apr. to Oct, 11 cases) and (b) for days on which 24-hr integrated PM$_{2.5}$ concentration was below 10 µg/m³ during cold (47 cases) and warm months (112 cases). They may not always represent accurately the actual composition of particulate matter in the atmosphere (mainly due to possible negative sampling artefacts), but are useful to assess which components contributed to the PM$_{2.5}$ mass collected by quartz fibre filters downstream of a 20 cm-long carbon monolith denuder.

Over the whole year 2021, carbonaceous species accounted for 55% of PM$_{2.5}$ (EC: 7%, POM: 48%), and secondary inorganics for 34% (NH$_4$: 8%, NO$_3$: 14%, and SO$_4$: 12%). Note that in 2021 the unaccounted mass was 7%. In both the cold and the warm seasons, most polluted days are characterised by an important increase in NO$_3^-$ contribution. Considering low PM$_{2.5}$ concentration days, summertime is characterised by higher SO$_4^{2-}$ concentrations (faster SO$_2$ photochemical conversion) and lower NO$_3^-$ concentrations (equilibrium shifted towards the gas phase as temperatures increase). Dust and salts do not contribute significantly to the PM$_{2.5}$ mass.

Table 5. Annual mean concentrations and contributions of major PM$_{2.5}$ constituents in 2021

constituent	salts Cl$^-$, Na$^+$, K$^+$, Mg^{2+}, and Ca^{2+}	NH$_4^+$	NO$_3^-$	SO$_4^{2-}$	POM	EC	dust	unaccounted
Mean concentration (µg m^{-3})	0.3	0.9	1.8	1.0	4.9	0.7	0.1	
Mean contribution (%)	2.5	8.4	13.6	12.3	48.2	6.8	0.8	7.4

Source: JRC, 2022

Fig. 28. 24 hr – averaged particle number concentrations for Dp < 800 nm and Dp >500 nm in 2021.
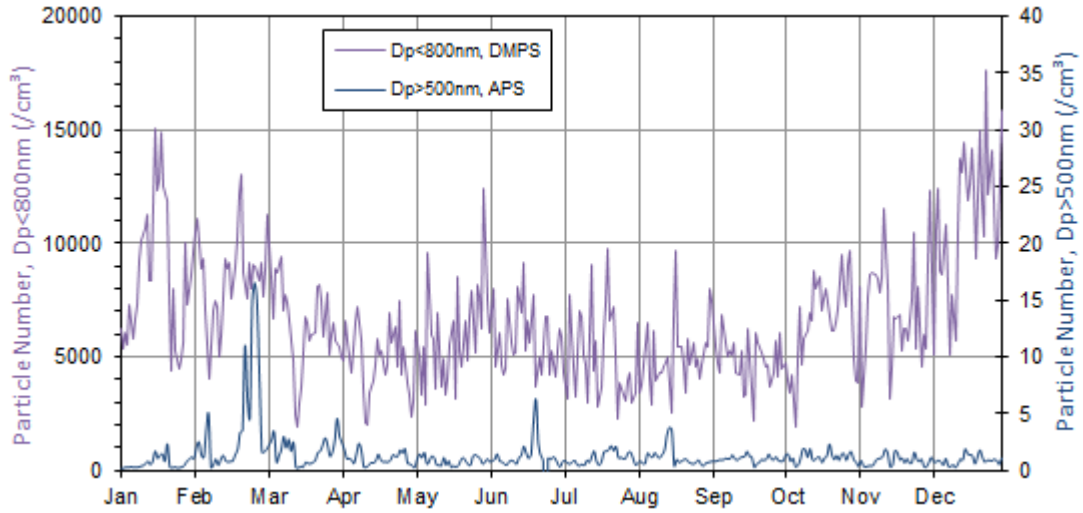
Source: JRC, 2022

Fig. 29. 24 hr – averaged particle geometric mean mobility diameter (from DMPS) and standard deviation in 2021
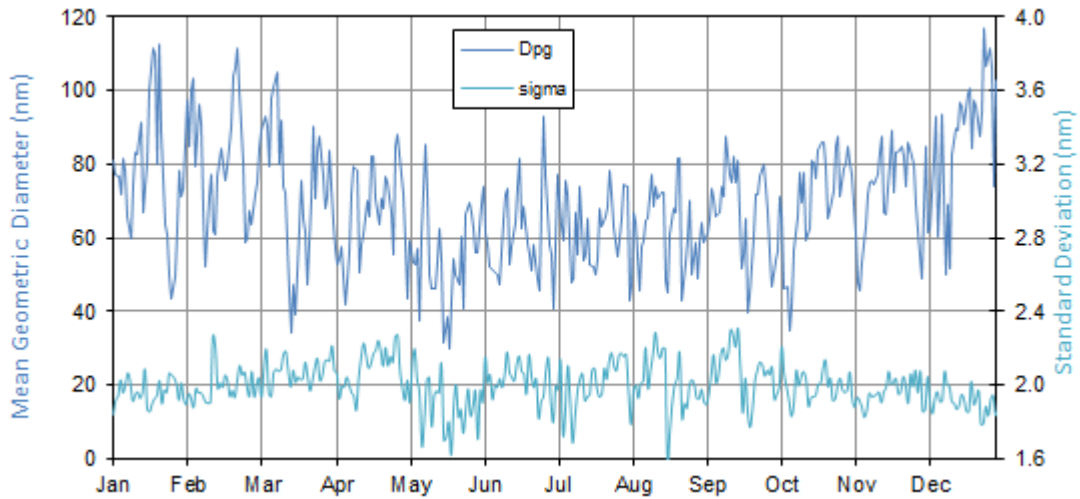
Source: JRC, 2022

Fig. 30. 24 hr – averaged particle volume concentrations for Dp< 800 nm and Dp > 800 nm in 2021.
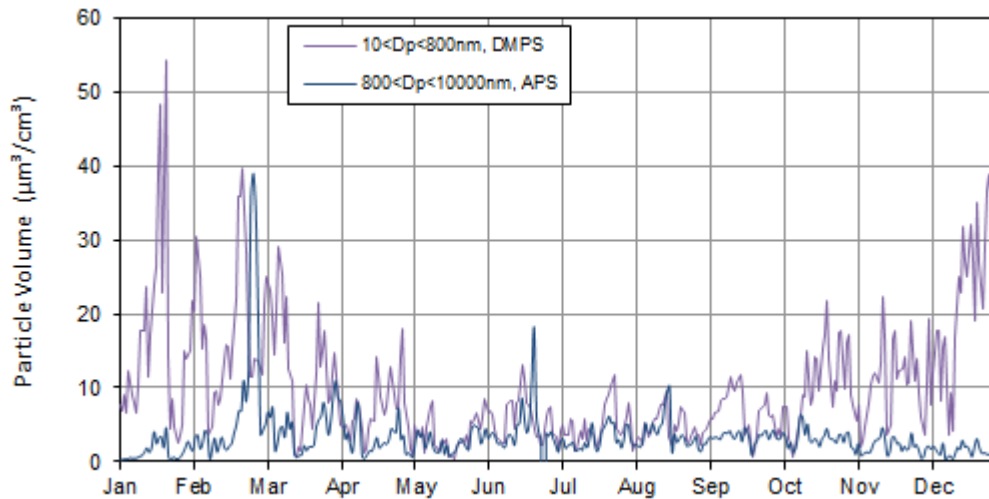
Source: JRC, 2022

4.4.3.4 Aerosol micro-physical properties

Measurements of the number size distribution of particles smaller than 800 nm in diameter were carried out using a Differential Mobility Particle Sizer continuously in 2021, with no major break (data coverage = 99.5%). The DMPS data presented here have been corrected for inlet diffusion losses and CPC efficiency.

Particle number concentrations averaged over 24 hr (from 08:00 to 08:00 UTC) ranged from 1890 to 17600 cm^{-3} (average: 6630 cm^{-3}). The annual mean and the maximum daily average particle number concentration were less than in 2020 (–5% and –28%, respectively), while the minimum daily average was 31% greater. Particle number concentrations followed a seasonal cycle similar to that of PM mass concentrations, with maxima in winter and minima in summer (Fig. 28). Episodes of local contamination were flagged during the data analysis process. Excluding the data points affected by local contamination (1.6% of the data), the annual mean particle number drops by 1%.

The mean mode diameter at RH < 40 % ranged between 30 and 120 nm (average = 70 nm) in 2021. These metrics are rather constant from year to year (2020 and 2021 included). However, the variations in these particle size distribution characteristics (Fig. 29) show seasonal patterns: the mean geometric diameter is generally larger in winter (about 50–110 nm) than in summer (about 40– 80 nm), whereas the standard deviation of the distribution follows an opposite trend (with generally a larger variability in summer compared to winter).

The size distribution of particles larger than 500 nm was measured using an Aerodynamic Particle Sizer almost continuously in 2021, resulting in a data coverage of 99.5%. Aerodynamic diameters were converted to geometric diameter assuming a particle density of 1.5. As previously observed, particles larger than 500 nm generally (90th percentile) accounted for 0.03% of the total particle number only (Fig. 28), but for 29 % of the total particle volume on average (Fig. 30). The seasonal variations in particle volume concentration reflect the changes in particle number and mean geometric diameter, with larger concentrations in winter than in summer.

Fig. 31. Monthly mean particle number (left) and volume (right) size distributions measured in 2021 with a DMPS (10-800 nm, solid lines) and an APS (0.85-10 µm, dashed lines). Particle densities of **1.0 g cm**$^{-3}$ and **1.3 g cm**$^{-3}$ were used to convert aerodynamic to geometric diameters for cold and warm months, respectively.
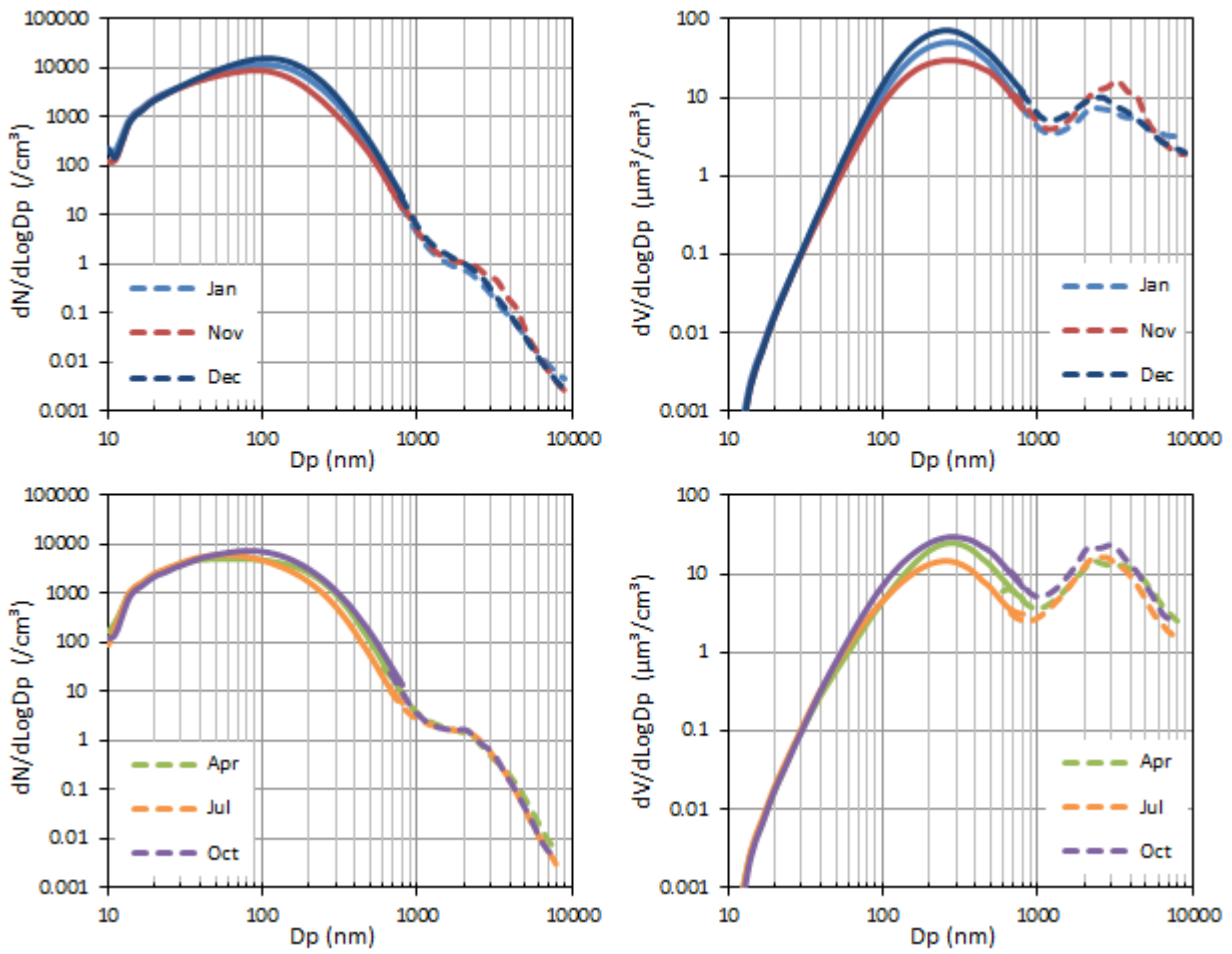
Source: JRC, 2022

Fig. 32. 2021 regressions between (left) PM$_{2.5}$ mass concentrations determined from gravimetric measurements at 20% RH and particle volume (Dp < 2.5 µm) calculated from DMPS and APS measurements (<40% RH), and (right) between PM$_{10}$ mass concentrations measured with the TEOM-FDMS at 30 % RH and particle volume (Dp < 10 µm) at <40% RH. Orange diamonds refer to desert dust outbreaks.

Source: JRC, 2022

47
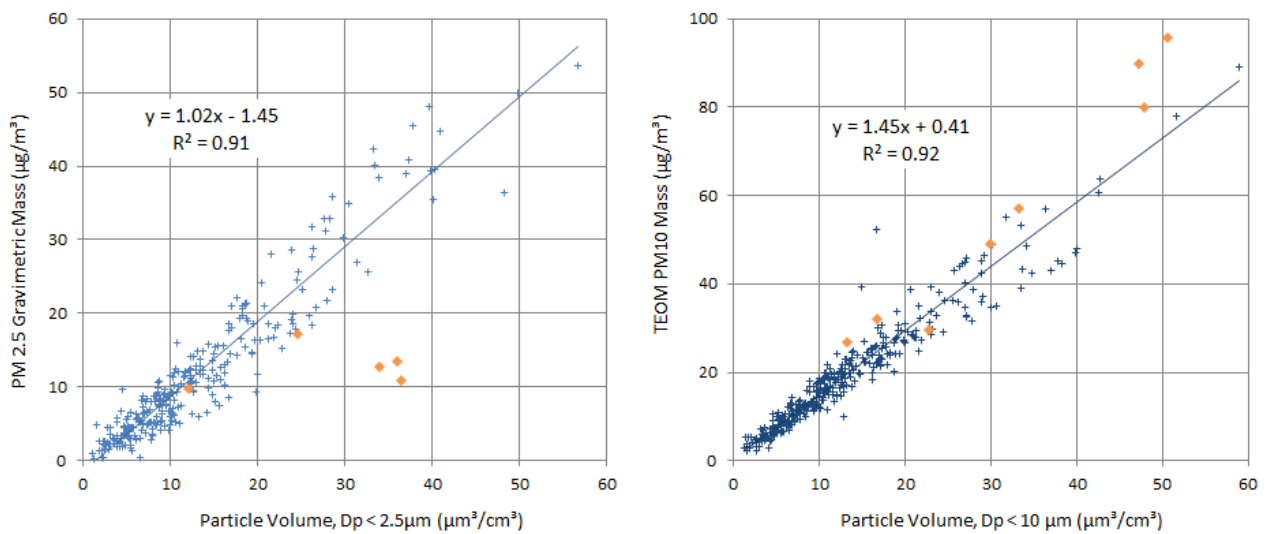
Fig. 31 illustrates the large predominance of sub-µm particles in the particle number size distribution. Even particle volume (and therefore PM mass) is dominated by sub-µm particles (almost half of the particle volume actually sits in particles < 300 nm). A good agreement between particle number size distributions measured with the DMPS and the APS (Fig. 31) could be obtained by using aerosol density values ranging between 0.9 and 2.0 g cm^{-3} to convert aerodynamic diameters (measured by the APS) to mobility diameters (measured by the DMPS), to be compared with the density derived from PM$_{2.5}$ and PM$_{10}$ mass and volume concentration measurements performed at the Observatory in 2021 (1.02 – 1.45, Fig. 32) and the range (1.6 ± 0.1 g cm^{-3}) expected for atmospheric particles (McMurry et al., 2002). Assuming that the DMSP is as accurate as it was during the calibration workshop in June 2019 at the WCCAP (see report-MPSS-2019-3-4) and since the APS sizing accuracy is checked regularly, low aerosol density values needed to reconcile DMPS and APS measurements could be explained only by a decrease in the APS counting efficiency.

Both comparisons between PM mass and aerosol particle volume concentrations show a good correlation (Fig. 32), considering that possible variations in the aerosol density play a role in such regressions. The slope of the regression between PM$_{2.5}$ at 20 % RH and particle volume suggests a mean aerosol density of 1.02, i.e., a regular decrease across the past decade (from 1.38 in 2011). The regression between PM$_{10}$ mass and aerosol volume concentration (for Dp < 10 µm) suggests a density of 1.45. The disagreement between these two aerosol density estimates suggest that PM$_{2.5}$ gravimetric measurements were probably underestimated in 2021.

Fig. 33. Daily mean atmospheric particle light scattering (top), backscattering (middle), and absorption (bottom) coefficients at three wavelengths, as derived from Nephelometer, Aethalometer and MAAP (red2) measurements (not corrected for RH) performed in 2021.
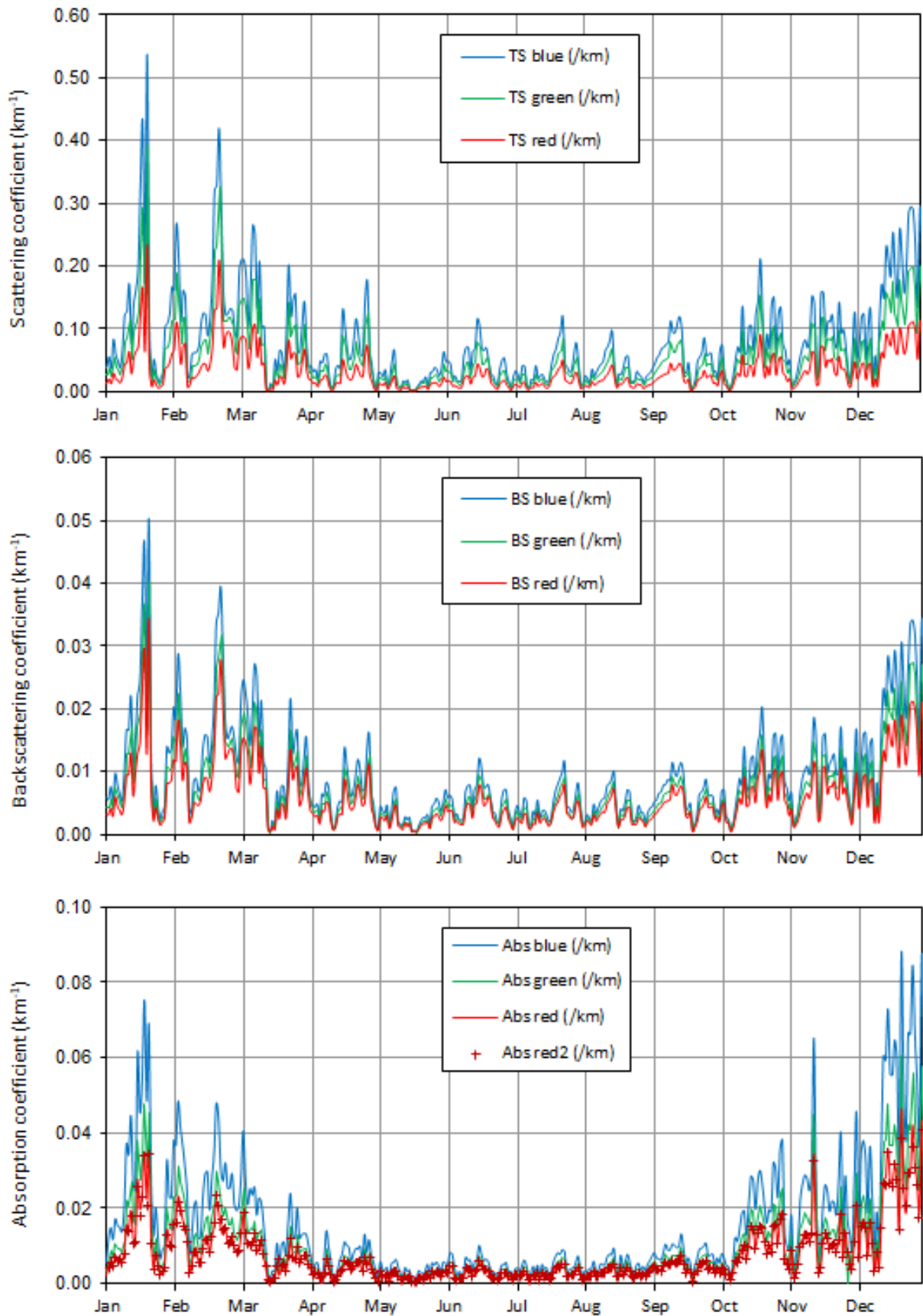
Source: JRC, 2022

4.4.3.5 Aerosol optical properties

Aerosol particle optical properties have been monitored continuously in 2021 except for 2 days in March and April (scattering and backscattering) resulting in a data coverage of 98.6% and 99.5% for aerosol light scattering and absorption measurements, respectively. Data from the Nephelometer (Fig. 33 a and b) have been corrected for angular non-idealities (truncation to 7 – 170°, slightly not cosine-weighted distribution of illumination) according to Anderson and Ogren (1998), but not for RH effects. Thanks to the use of a Nafion dryer and the reduction of the sampling flow rate (6 L min^{-1}), the Nephelometer internal RH was maintained below 40% at all time, except for 270 hours in July and August (40<RH<52%). At 40% RH, aerosol scattering is on average increased by about 20 % compared to 0% RH in Ispra (Adam et al., 2012).

Atmospheric particle absorption coefficients at 7 wavelengths were derived from the Aethalometer AE-31 data corrected for the shadowing and multiple scattering effects when Nephelometer data were available, according to Weingartner et al. (2003), making use of coefficients derived from Schmid et al. (2006), i.e. 3.60, 3.65 and 3.95 at 470, 520, and 660 nm, respectively (Fig. 33 c).

Both scattering and absorption coefficients follow seasonal variations (Fig. 33) in line with PM mass variations, mainly controlled by the dispersion rate of particulate pollution.

The uncertainty in the multiple scattering correction factor may introduce a quite large uncertainty in the aerosol absorption coefficient values, since correction factors ranging from 2 to 4 have been proposed (Weingartner et al., 2003; Arnott et al., 2005). The use of the correction factors listed above leads to aerosol absorption coefficients at 660 nm about 4% greater than absorption coefficients obtained from the Multi Angle Absorption Photometer (MAAP) at 637 nm (Fig. 34, left), whereas ~5% smaller values would be expected considering the wavelength difference. The aerosol light extinction coefficient values derived from the extinction cell (CAPS-SSA) measurements are in excellent agreement with the extinction coefficient calculated from the nephelometer and MAAP measurement data (Fig. 34, right), which suggest that aerosol light scattering and absorption measurements are very accurate.

NB: it has been recommended by ACTRIS since December 2015 that Aethalometer derived absorption data should be corrected using a constant coefficient (3.5) at all wavelengths, without any further correction for the filter loading. The ACTRIS correction technique is used to process the Aethalometer data submitted to the ACTRIS Data Centre.

Fig. 34. Comparison between (left) the AE-31 and MAAP derived light absorption coefficients at 660 and 637 nm, respectively, and (right) the extinction cell (CAPS) and the nephelometer + MAAP derived extinction coefficients at ~630 nm. Data points are daily averages from 2021.
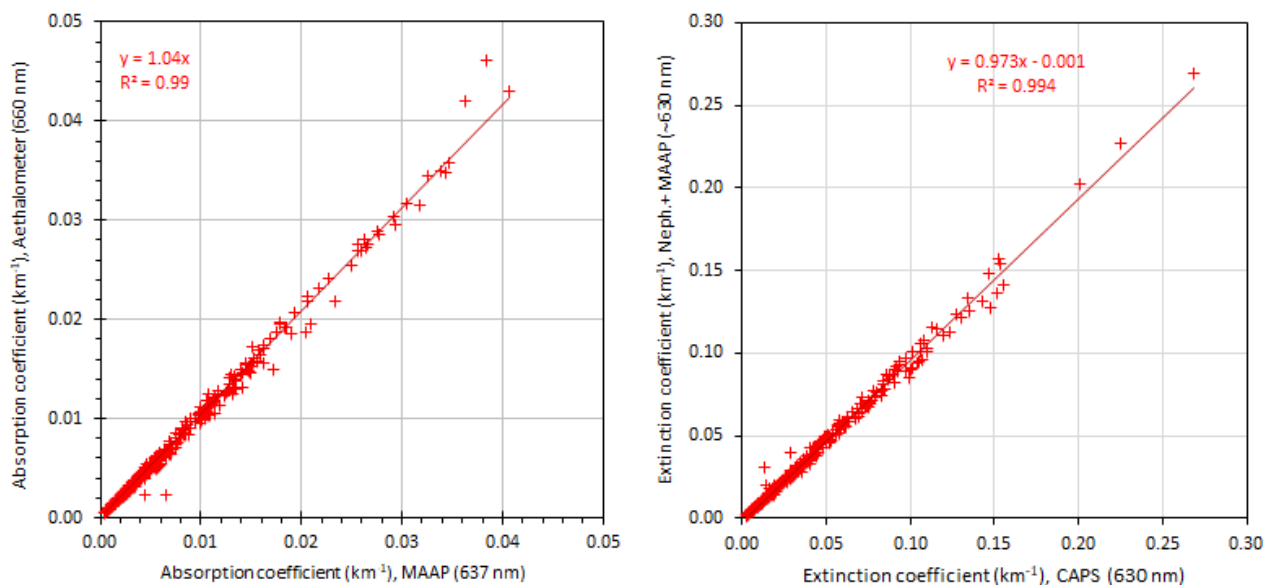
Source: JRC, 2022

Fig. 35. Aerosol 24-hr averaged single scattering albedo and backscatter to total scatter ratio at three wavelengths corresponding to blue, green and red light, as calculated for 2021 (RH < 40%).
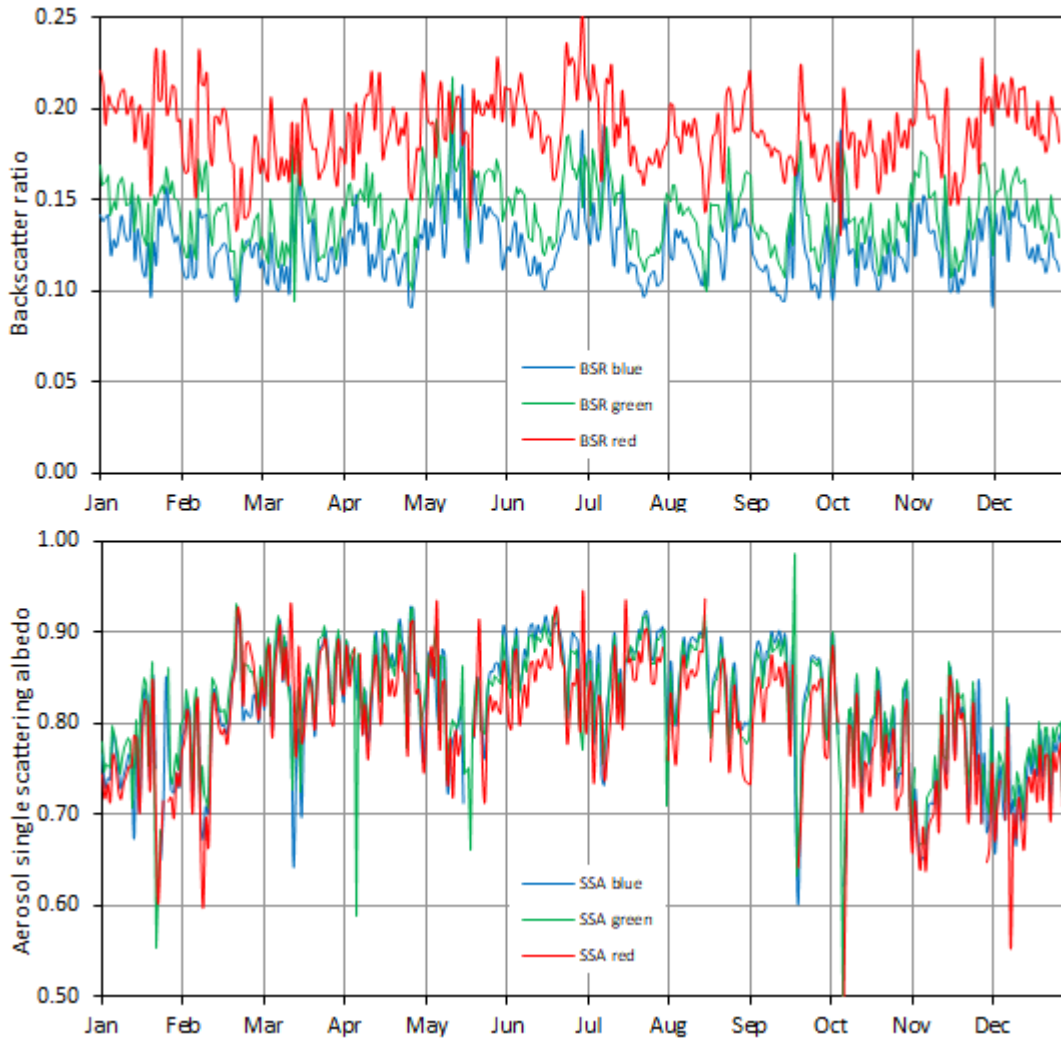
Source: JRC, 2022

Fig. 36. Regressions between the aerosol extinction coefficient at 550 nm (Nephelometer + Aethalometer) and PM$_{10}$ mass (FDMS-TEOM) and volume (DMPS + APS) concentrations in 2021. Diamonds refer to desert dust outbreaks.
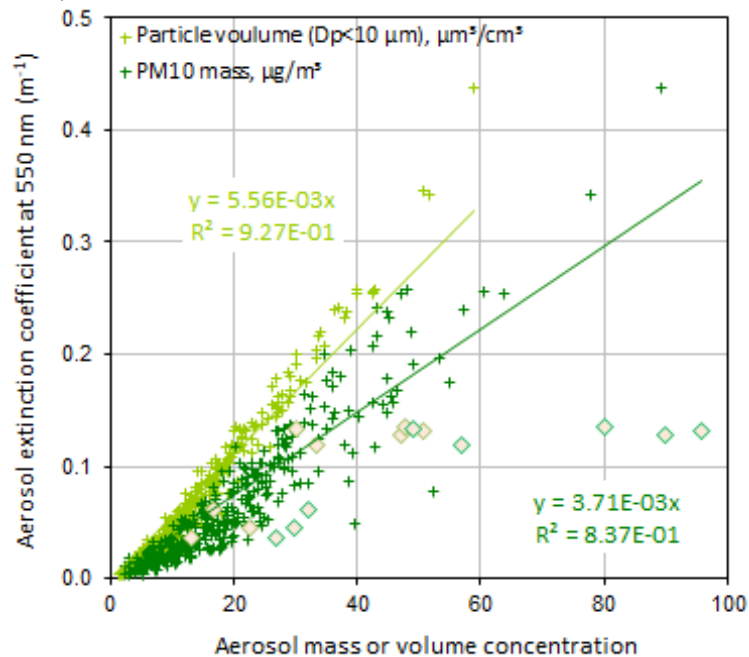
Source: JRC, 2022

The backscatter / total scatter ratio (Fig. 35, top) at λ = 550 nm (green) ranged from 0.09 to 0.22 (average 0.14), i.e., similar to 2018-2020 and about 10% greater than in 2017.

The 24 hr-averaged aerosol single scattering albedo at λ = 550 nm (at RH < 40 %) ranged from 0.50 to 0.99 (annual average 0.82), with generally lower values in autumn and winter compared to spring and summer (Fig. 35, top). The mean SSA was in 2021 slightly less than in 2020, but greater than the values observed between 2010 and 2019 (0.75-0.80), when measurements were performed at the same site (see Section 4.5.4). The absorption coefficients were flagged for local contamination before submission to the WDCA data bank (EBAS). Excluding the values clearly affected by local influences, the mean single scattering albedo was only 0.3% greater.

The aerosol light extinction coefficient and particle mass or volume concentrations were rather well correlated (Fig. 36), although most data points corresponding to extinction coefficients < 0.1 km^{-1} sit under the regression line. The slope of the regression between extinction and mass shows that the mass extinction cross section was 3.7 m^2 g^{-1}, greater than the range of the values observed earlier (2.5 – 3.4 m^2 g^{-1}), but still low compared with the estimate (4.3 – 4.6 m^2 g^{-1}) calculated from the aerosol mean chemical composition during 2021 and mass cross section coefficients of the various constituents found in the literature (see Table 6). Based on the particle volume determination, and assuming a mean aerosol density of 1.5 g cm^{-3}, the mass extinction cross section would be the same (3.7 m^2 g^{-1}). The agreement between these two estimates of the aerosol extinction cross section has deteriorated since 2010 – 2012. Extinction measurements performed with the CAPS instrument showed an excellent agreement (Fig. 34) with extinction values calculated as scattering (from the nephelometer) + absorption (from the MAAP). Therefore, the accuracy of PM$_{2.5}$ mass and particle volume measurements may be questionable.

Table 6. Mean aerosol chemical composition (PM$_{2.5}$) in 2021 and extinction cross section.

	2021 PM$_{2.5}$ comp. (%)	σ_{ext} (m^2/g)	Reference (for σ_{ext})
"sea salt"	3	1.3	Hess et al., 1998
NH$_4^+$, NO$_3^-$ and SO$_4^{2-}$	34	5.0	Kiehl et al., 2000
organic matter	48	3.6	Cooke et al., 1999
elemental carbon	7	11	Cooke et al., 1999
dust	1	0.6	Hess et al., 1998
unknown	7	1-5	
Total	**100**	**4.3 – 4.6**	

Source: JRC, 2022

Fig. 37. Aerosol vertical profile measurements performed daily with the aerosol Lidar in 2021.
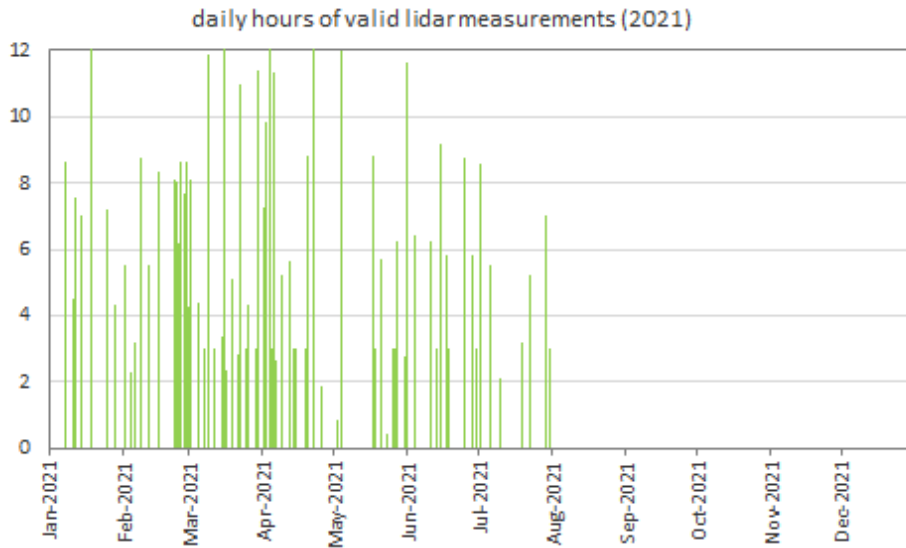
Fig. 38. Scheduled aerosol vertical profiling measurements performed monthly during the EARLINET climatology and Calipso overpass time slots in 2021.
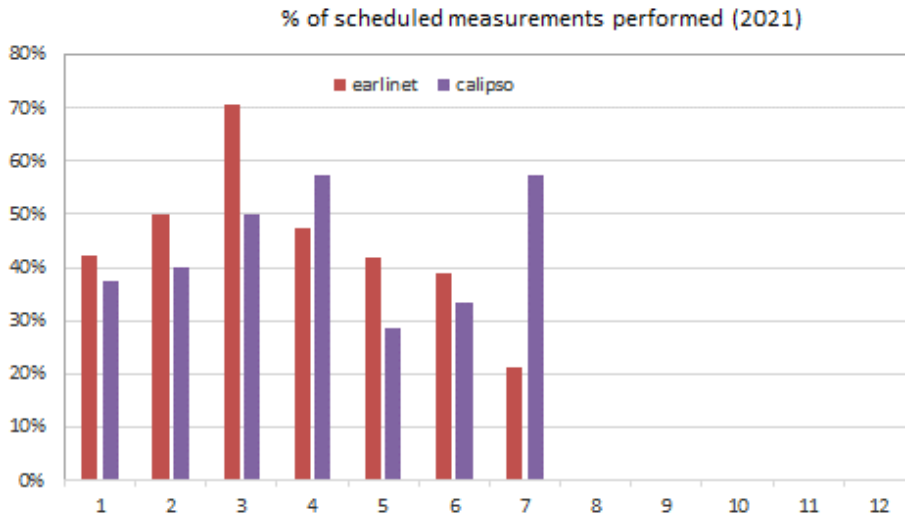
Fig. 39. Attenuated backscatter and depolarization ratio at 532 nm from Ispra (25 Feb. 2021) retrieved from the open access EARLINET Quicklook interface. These measurements show the desert dust outbreak which was also detected at the ground.

53

4.4.3.6 Aerosol vertical profiles

The Raman LiDAR from Raymetrics was operated for measuring aerosol vertical profiles from the Atmospheric Observatory until the end of July 2021, weather and staff availability permitting. LiDAR measurements were discontinued from August 2021 due to the laser power falling below the limit for obtaining valid data. The LiDAR had been running since 23 May 2017 with a new reception window, and since 28 May 2018 without emission window, being installed in a dedicated shelter.

In 2021, the LiDAR was operated for 458 hours (Fig. 37) to comply with ACTRIS requirements: measurements at noon (2 hr) and sunset (4-5 hr) on Mondays, at sunset only (4-5 hr) on Thursdays (EARLINET climatology), and during ESA satellite Calipso's overpasses ± 1 hr (every ~9 days at 02:00 and 13:00 UTC). The scheduled EARLINET and CALIPSO measurements were covered at 45% and 43% for the period January – July 2021, respectively (Fig. 38), to be compared with ACTRIS' target of 50% data coverage . This is a quite high time coverage since the LiDAR cannot be run automatically (meaning Calipso correlative measurements cannot always be covered during weekends) and only 1 operator is currently qualified to operate it.

From January 2020, LiDAR measurements have been taken with a 1 min time resolution. This makes it possible to use the automatic cloud screening provided by the ACTRIS-EARLINET Single Calculus Chain (SCC), as well as the automatic production of "quicklooks" (Fig. 39) in open access (https://quicklooks.earlinet.eu/). Shifting from 5 min to 1 min time resolution, together with directly converting raw binary LiDAR files to ACTRIS-SCC compliant NetCDF files, are two essential steps towards ACTRIS request to submit LiDAR profiles in real time in the near future. All data acquired in 2021 were processed using the SCC, and successfully submitted to the ACTRIS Data Centre via the EARLINET data base by December 2021. Further technical improvements would still be needed, especially regarding the accuracy of the Raman channels.

Fig. 40. (a) Precipitation amount, conductivity and (b) concentrations of 3 major ions in precipitation (bars), and pH (crosses) in 2021, and during the 1990-2010 period (line).
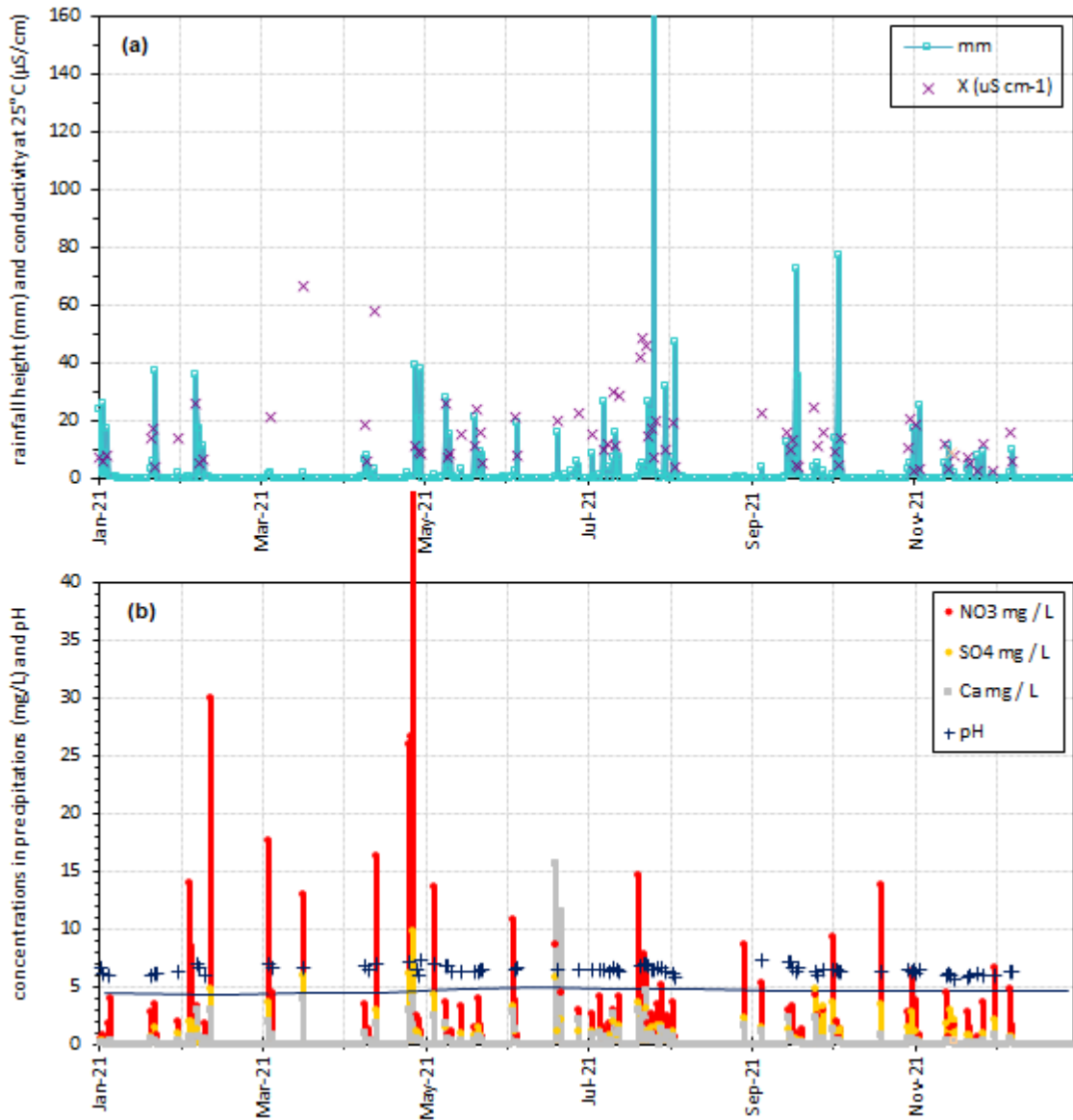
Source: JRC, 2022

Fig. 41. Wet deposition fluxes of 3 main ions measured in rain water in 2021.
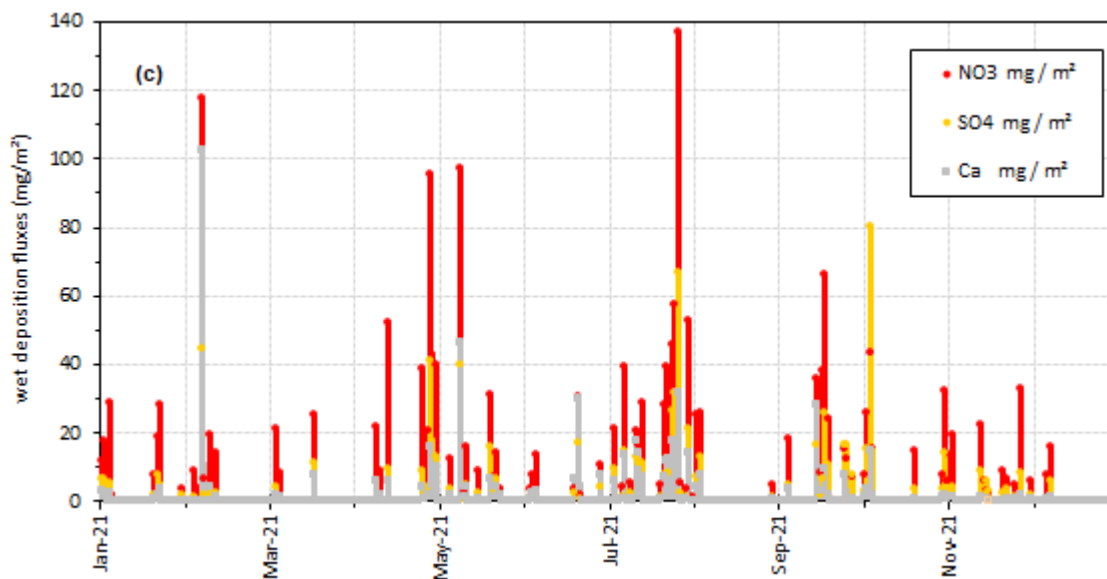
Source: JRC, 2022

4.4.3.7 Wet Aerosol deposition chemistry

In 2021, 111 precipitation samples were collected, i.e. in the range of the number of samples collected across 2017-2019 (83 – 135). The ionic content, acidity (pH) and conductivity were measured in 95, 81 and 74 of these samples (those for which water volume was sufficient). The precipitation height measured during the collected events ranged from 0.05 to 162 mm (Fig. 40a) for a total of 1199 mm (90% of the precipitation amount detected by the meteorological probe).

Rainfalls occurred mainly from the end of April to early November (Fig. 40). There were several drought periods across 2021.

The ranges of pH, conductivity, and concentrations measured in these samples are indicated in Table 7. In 2021, volume weighted mean concentrations of the anthropogenic species NO_3^-, SO_4^{2-}, and NH_4^+ were all lower than the 1990-2010 averages, while concentrations of all the marine and crustal components (Cl^-, Na^+, Mg^{2+}, Ca^{2+}) were greater than their long-term average. Considering our possible underestimation of rainwater acidity in 2021 (see section 4.3), pH values (Fig. 40b) will not be further commented..

In 2021, the annual wet deposition flux of the main acidifying and eutrophying species (Fig. 41) was 0.9, 2.1 and 1.3 g m^{-2} for SO_4^{2-}, NO_3^- and NH_4^+, respectively, i.e. very similar to 2020 values and about 30% less than the 2017-2019 average for SO_4^{2-} and NO_3^- (see also section 4.5.1 next page).

Table 7. Statistics relative to the precipitation samples collected in 2021 (averages are volume weighted), compared to long-term averages.

	pH	cond.	Cl^-	NO_3^-	SO_4^{2-}	Na^+	NH_4^+	K^+	Mg^{2+}	Ca^{2+}
		µS cm^{-1}	mg L^{-1}	mg L^{-1}	mg L^{-1}	mg L^{-1}	mg L^{-1}	mg L^{-1}	mg L^{-1}	mg L^{-1}
Average	6.24	11.34	0.46	2.56	0.94	0.40	1.19	0.05	0.08	0.68
Min	5.79	5.29	0.15	0.97	0.28	0.00	0.29	0.02	0.03	0.11
Max	6.69	33.73	1.41	10.95	3.43	1.07	3.03	0.13	0.38	2.22
1990-2010 av.	4.58	24.86	0.44	3.94	3.07	0.23	1.25	0.09	0.06	0.45

Source: JRC, 2022

Fig. 42. Oxidised sulphur species monthly mean concentrations and yearly wet deposition.
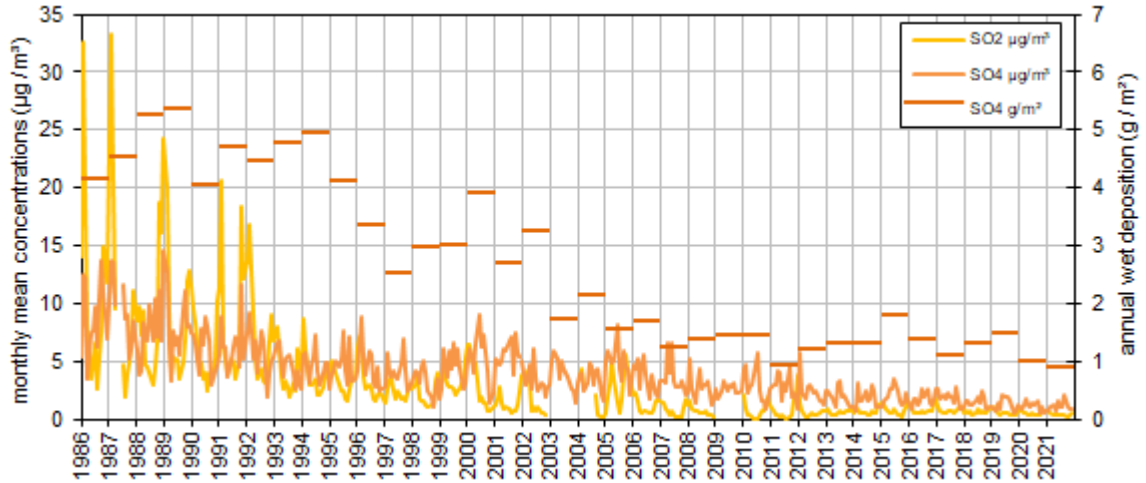
Fig. 43. Oxidised nitrogen species monthly mean concentrations and yearly wet deposition.
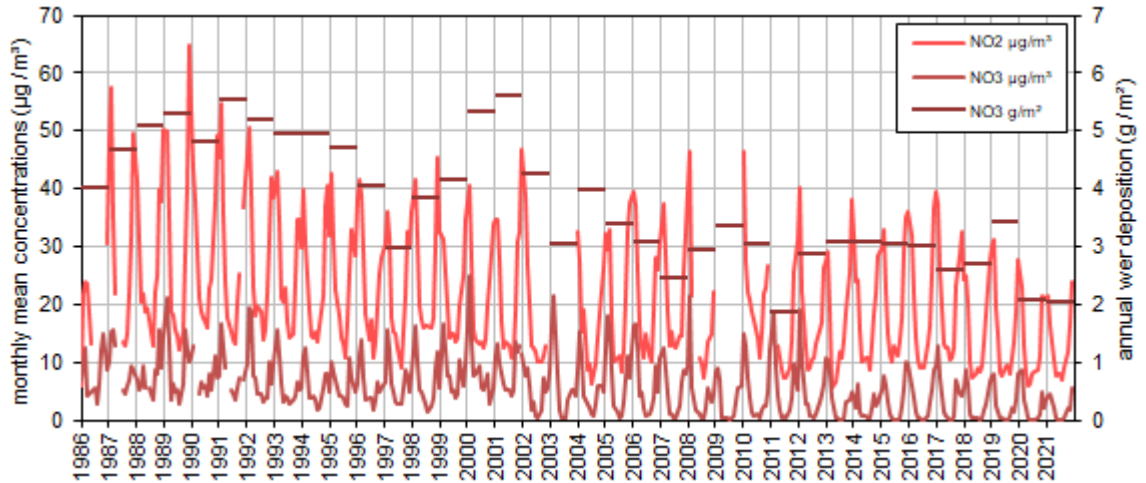
Fig. 44. Reduced nitrogen species monthly mean concentration and yearly wet deposition.
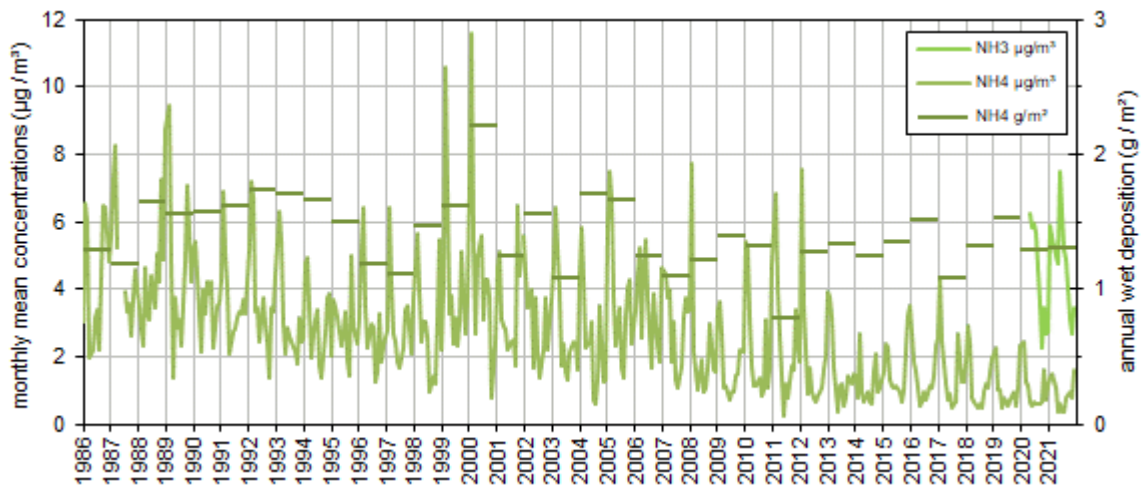
4.5 Results of year 2021 in relation to 35 years of measurements

Year 2021 was marked by several waves of COVID-19 epidemics in Italy, especially during the period ranging from January to April. Decreases in human mobility (Fig. 19) do undoubtedly lead to reduced pollutant emissions from transport, but possibly also to increased pollutant emissions from domestic heating. However, air pollutant concentrations are so greatly influenced by weather that 2021 cannot simply be compared to previous years to evaluate the impact of the COVID-19 epidemic waves on atmospheric pollution.

4.5.1 Sulphur and nitrogen compounds

The annual mean SO_2 concentration in 2021 (0.4 µg/m³) was 20% less than in 2020, 33% less than across 2017-2019, and reached the lowest value ever recorded at the Atmospheric Observatory of Ispra since 1886. In 2021, SO_2 concentrations were 11 times less than in the 90's, and more than 3 times less compared to the 2000's (Fig. 42). The annual mean particulate SO_4^{2-} concentration (1.1 µg/m³) also reached a historical minimum in 2021, 6% less than the previous record (2020), and 70% less compared to the 2000's. It should be kept in mind that SO_4^{2-} concentrations were measured in PM_{10} or in $PM_{2.5}$ from 2002 onwards, whereas it was measured in TSP (Total Suspended Particulate) from 1986 to 2001. However, simultaneous sampling of PM_{10} and TSP over 14 months showed that SO_4^{2-} in PM_{10} is generally less than 5 % lower than in TSP. SO_4^{2-} is mainly present in the $PM_{2.5}$ fraction at our site (see Fig. 24 of the ABC-IS annual report 2010). From 2005 onwards the calculations were as follows:

$$SO_4^{2-}(PM_{10}) = SO_4^{2-}(PM_{2.5}) \times <SO_4^{2-}(PM_{10})/ SO_4^{2-}(PM_{2.5})> \qquad \text{Eq. 3}$$

the average $<SO_4^{2-}(PM_{10})/ SO_4^{2-}(PM_{2.5})>$ being calculated based on the simultaneous PM_{10} and $PM_{2.5}$ samples collected in 2010-2012.

Particulate SO_4^{2-} concentrations decreased much less than SO_2 concentrations, which suggests that locally produced SO_2 decreased much more than possibly long-range transported SO_4^{2-} over the past 30-35 years. SO_4^{2-} wet deposition in 2021 was also 10% less than in 2020, 25% less than across the previous 3 years (Fig. 42), and less than half compared to values observed in the late 2000's.

In 2021, the annual mean NO_2 concentration (13 µg/m³) was also the lowest observed since 1986 (although only 1% less than in 2020), and 33% less compared to the 2000's (Fig. 43). Both wintertime maxima and summertime minimum were amongst the lowest measured over the past decade. However, monthly mean concentrations of nitrogen dioxide (NO_2) do not show as much of a pronounced decreasing trend as seen for SO_2 over the past 35 years (Fig. 42), and do not reflect the abatement in NO_x emissions reported in the emission inventories for this period. The particulate NO_3^- annual mean concentration observed in 2021 (2.0 µg/m³) was also the lowest record, 20% less than in 2020, 35% less than during the past 3 years, and 60% less than in the 2000's. It should be noted that since October 2000, NH_4^+ and NO_3^- have been measured from quartz fibre filters, which are known to lose NH_4NO_3 at temperatures > 20 °C, as demonstrated e.g. by the comparison with the ACSM measurements we performed in Ispra in 2013. This might contribute significantly to the low summertime minima NO_3^- seen since 2002. Furthermore, NO_3^- was measured from PM_{10} or in $PM_{2.5}$ from 2002, and no more from TSP, as over the 1986 to 2001 period. However, simultaneous sampling of PM_{10} and TSP over 14 months showed that NO_3^- in PM_{10} is generally less than 5 % lower than in TSP, like SO_4^{2-}. From 2005 and onwards the calculations were as follows:

$$NO_3^-(PM_{10}) = NO_3^-(PM_{2.5}) \times <NO_3^-(PM_{10})/ NO_3^- (PM_{2.5})> \qquad \text{Eq. 4}$$

the average $< NO_3^-(PM_{10})/ NO_3^-(PM_{2.5})>$ being calculated based on the simultaneous PM_{10} and $PM_{2.5}$ samples collected in 2010-2012. The NO_3^- wet deposition annual flux observed in 2021 was the second lowest ever observed, only 1% less than in 2020, but 30% less compared to the 3 previous years (Fig. 43), and compared to the previous decade.

The 2021 annual mean concentration of NH_4^+ in particulate matter (0.9 µg/m³) was the lowest record observed during the past 35 years (-20% compared to 2020), 30% less than the average across 2017-2019, and 3 times less compared to the 2000s and 2010s decades (Fig. 44).

Fig. 45. Particulate matter mass concentration monthly (grey) and annual (black) averages. The red line is the long term trend over annual averages. All values are gravimetric measurements or estimates from gravimetric measurements.
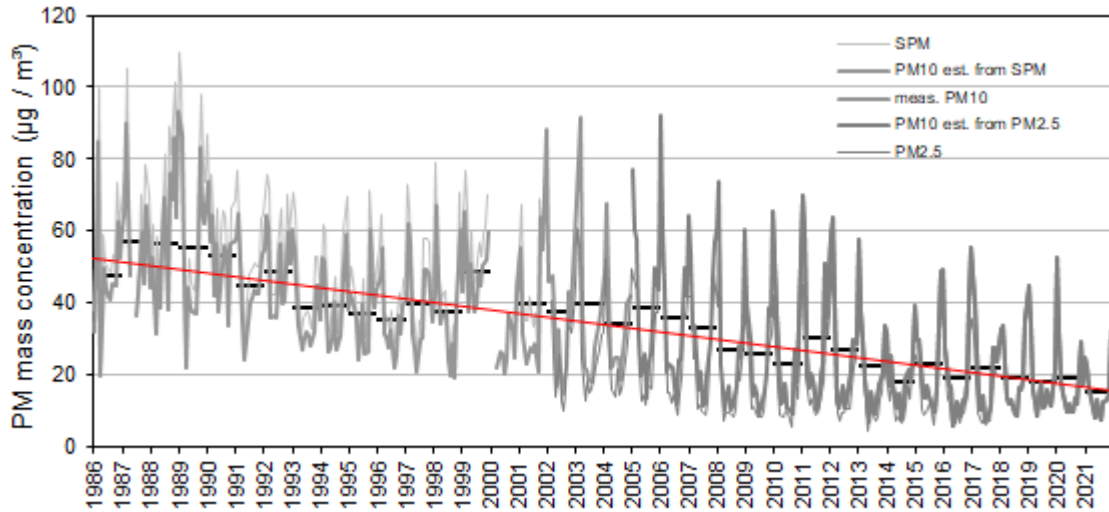
Source: JRC, 2022

Fig. 46. Ozone yearly and monthly mean concentrations.
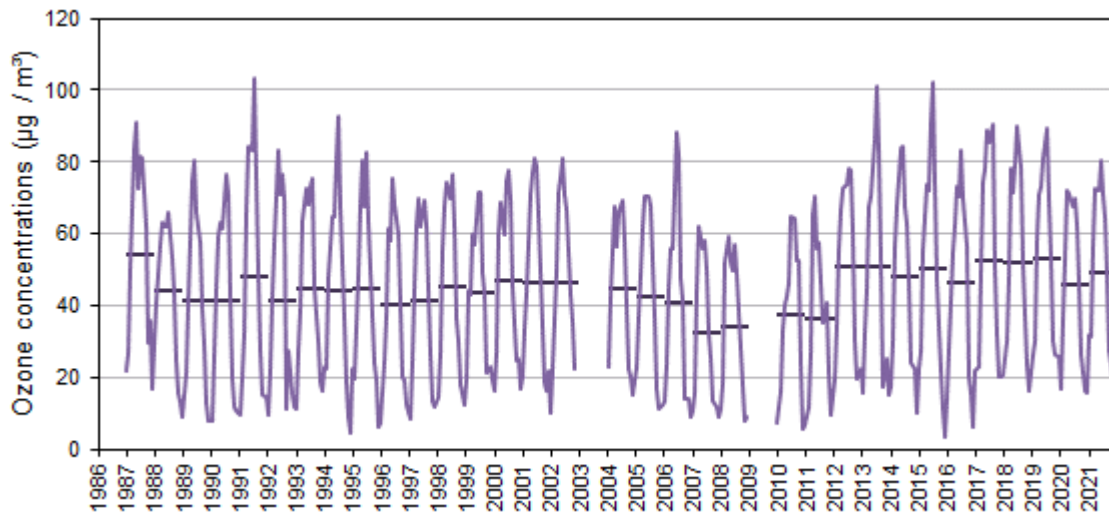
Source: JRC, 2022

Fig. 47. Number of O_3 limit value exceedances (days) and AOT40 and SOMO35 values.
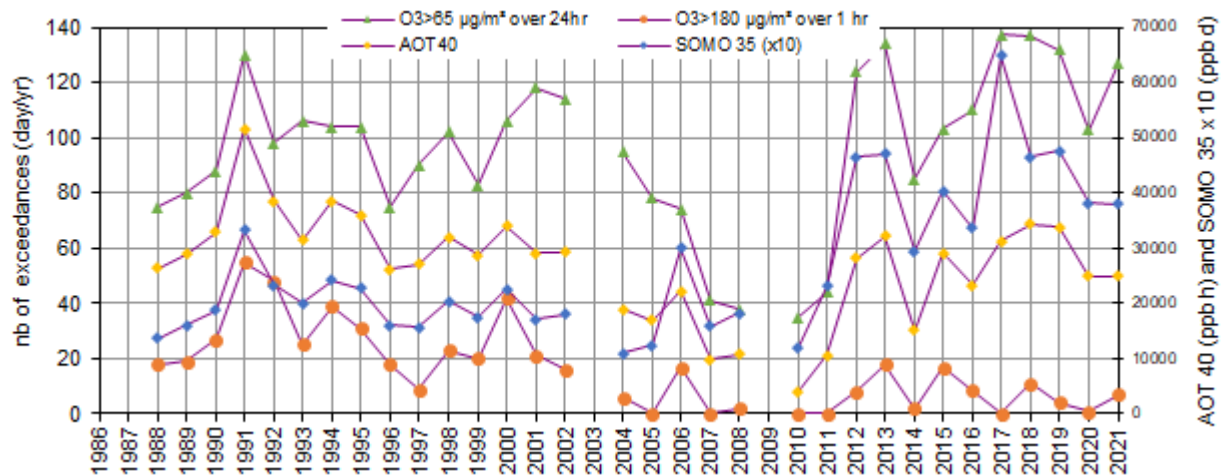
Source: JRC, 2022

It should be noted that from the year 2002, NH_4^+ was measured in the PM_{10} or in the $PM_{2.5}$ fraction. From 2005 and onwards, NH_4^+ concentrations in PM_{10} were calculated as follows:

$$NH_4^+(PM_{10}) = NH_4^+(PM_{2.5}) \times <NH_4^+(PM_{10})/ NH_4^+(PM_{2.5})> \hspace{4cm} \text{Eq. 5}$$

where the average $<NH_4^+(PM_{10})/ NH_4^+(PM_{2.5})>$ is calculated based on simultaneous PM_{10} and $PM_{2.5}$ measurements performed in 2010-2012. On average, NH_4^+ can neutralise nearly 100% of the acidity associated with NO_3^- and SO_4^{2-} in the particulate phase (see Fig. 26). NH_4^+ is also quite well correlated with $NO_3^- + SO_4^{2-}$ in rainwater. NH_4^+ annual wet deposition in 2021 was the same as in 2020 and during the previous 3 years, and only 10% less than during the previous decade (Fig. 44).

4.5.2 Particulate matter mass

The 2021 annual mean $PM_{2.5}$ concentration measured at 20% RH (11.6 µg/m³) was the lowest ever recorded, 17% less than in 2020, 20% less than across 2017 - 2019, and half of the 2000's average. The annual value for PM_{10} at 50% RH estimated from $PM_{2.5}$ measurements is therefore in line with the general decreasing trend of -1.0 µg m^{-3} yr^{-1} across the 3 last decades (Fig. 45). It should however be kept in mind that PM_{10} concentrations were estimated from TSP mass concentration measurements (carried out by weighing at 60 % RH and 20 °C cellulose acetate filters sampled without any particle size cut-off and "dried" at 60 °C before and after sampling) over 1986-2000, based on a comparison between TSP and PM_{10} over the Oct. 2000 - Dec. 2001 period (R^2 = 0.93, slope = 0.85), and derived from measured $PM_{2.5}$ values for years 2005-2020. Furthermore, technical issues occurred during filter weighing in 2021, due to an increased friability of the quartz fibre filters recently delivered by our supplier. The series of large winter concentrations observed between 2015 and 2020 (only interrupted in 2018) can be at least partly due to the exceptionally dry Dec. 2015, Jan. and Dec. 2016, Jan. 2017, and Jan.-Feb. 2019 and 2020. Summertime PM minima showed a clear decreasing trend over 1986 – 2013, but have remained fairly constant since then.

4.5.3 Ozone

Fig. 46 shows monthly and yearly mean O_3 concentrations observed since 1987. Ozone was not measured in 2009 and there was a major data acquisition breakdown in 2003. In 2021, the annual mean O_3 concentration (49 µg/m³) increased compared to 2020 (+7%) but remain lower than across 2017 – 2019, and in line the relatively high annual mean values observed since 2012 as compared to the previous 3 decades. AOT40 and SOMO35 indicators were very similar to 2020, while the number of exceedances of the 65 µg/m³ threshold and the number of days with extreme peak values (180 µg/m³ over 1hour) increased.

Both indicators for the vegetation protection (number of days with a 24-hour mean O_3 concentration > 65 µg/m³, vegetation protection limit, and the AOT40, Accumulated Ozone exposure over a Threshold of 40 ppb) have generally been increasing during the 2010's and remain similar to or greater than the values observed in the 1990's after the minimum observed in the 2000's (Fig. 47). They levelled off towards the end of the decade and decreased in 2020 but not consistently in 2021. The population exposure indicator SOMO 35 (Sum of Ozone Means Over 35 ppb, where means stands for maximum 8-hour mean over day) also decreased in 2020 compared to previous years, and remained as low in 2021, but still greater than across the 3 previous decades (Fig. 47).

Fig. 48. Particle number (left) and volume (right) monthly mean concentrations.
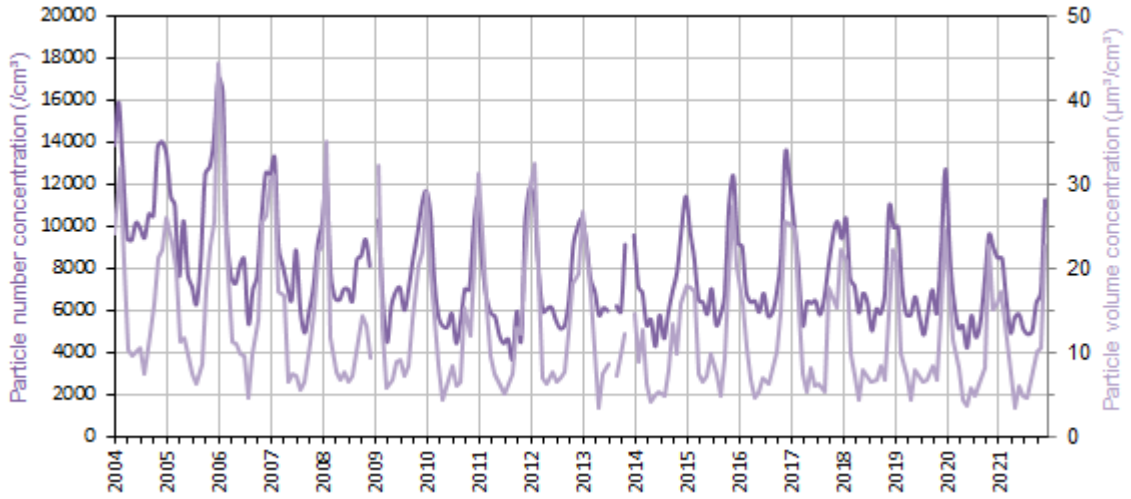
Source: JRC, 2022

Fig. 49. Aerosol green light scattering and absorption monthly mean coefficients
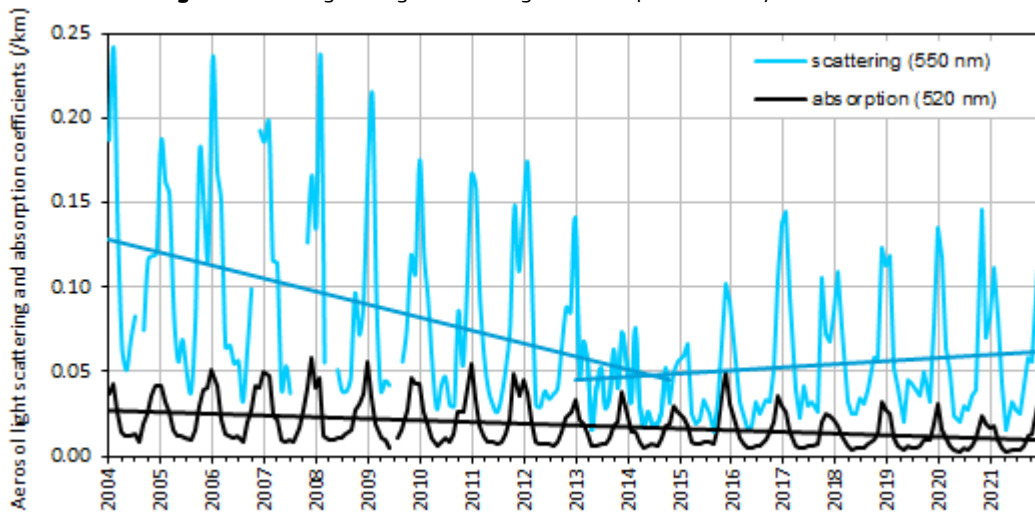
Source: JRC, 2022

Fig. 50. Aerosol optical characteristics at 550 nm (monthly means): single scattering albedo, backscatter ratio (left hand axis), and scattering Ångström exponent (right hand axis).

Source: JRC, 2022

61
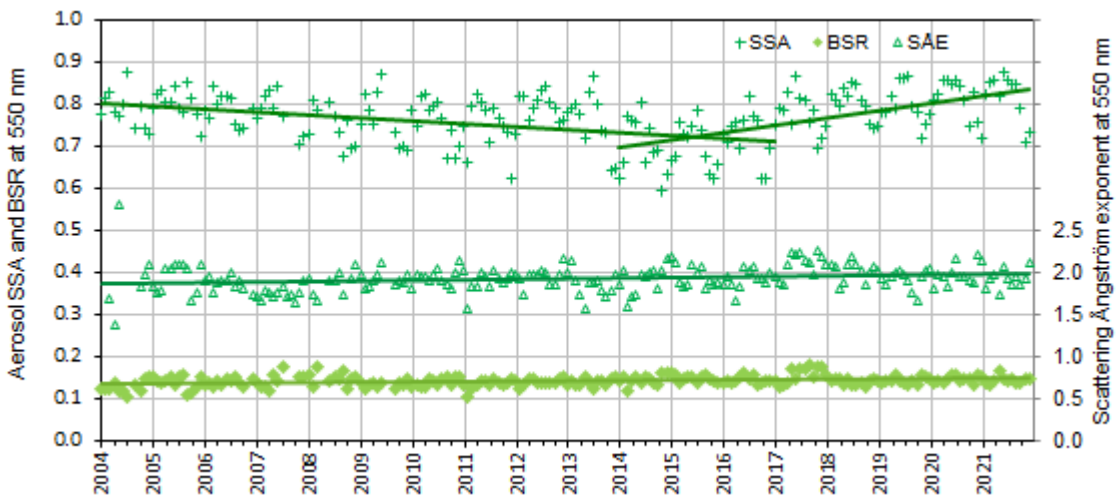
4.5.4　Aerosol micro-physical and optical properties

Measurements of aerosol microphysical properties started at the atmospheric research station of the JRC-Ispra in 2004, which gave birth to one of the longest time series for this kind of measurements across Europe.

After the decreasing trend in sub-µm aerosol particle number and volume concentrations observed between 2004 and 2011, the annual average of both variables had started to increase since 2014, but concentrations dropped again from 2018 (despite the peak in particle number concentration in January 2020) and particle number annual concentration average reached its historical minimum (6600 cm^{-3}) in 2021 (Fig. 48), unlike the particle volume concentration.

These trends are to some extent reflected in the long-term variations of the aerosol light scattering coefficient (Fig. 49), which is sensitive to both the number and size of atmospheric particles. In contrast, the aerosol light absorption coefficient has been generally decreasing across the past 2 decades, both in summer and winter. As a consequence, the aerosol single scattering albedo (SSA = scattering/(scattering + absorption)) significantly decreased between 2004 and 2015, and seems to be increasing again since then. This is good for climate change mitigation since this increases the direct cooling effect by atmospheric particles at the top of the atmosphere, in contrast to what was observed between 2004 and 2012 (Putaud et al., 2014). Simple regression analyses suggest that both the scattering Ångström exponent and the aerosol backscatter ratio have been increasing (about +0.5%/year) on the long term (Fig. 50), which indicates decreasing particle diameters with time.

4.6　Conclusions

In-situ measurements of short-lived pollutants and climate forcers were carried out almost continuously in 2021 (data coverage ≥99%) at 9 m agl from the terrace of the Atmospheric Observatory (Fig. 1), despite the COVID-19 epidemic waves between January and April, with the exception of NMHC measurements which were discontinued due to a serious technical issue. Remote sensing of aerosol vertical profiles was stopped from August 2021 due to a drop of the laser power below the limit permitting the acquisition of good quality data.

COVID-19 epidemic waves are expected to lead to decreases air pollutant emissions from e.g. traffic. They can also induce increases in emissions from domestic heating during cold months (e.g. Putaud et al, 2021). However, air pollution being strongly influenced by weather conditions, changes in air pollution metrics observed in 2020 and 2021 compared to previous years cannot simply be interpreted as direct consequences of reduced human mobility during COVID-19 waves before direct cause-and-effect relationships are demonstrated.

Year 2021 as a whole was warmer compared to the reference period (1990 – 2010), but rather cooler than the 3 previous years. Solar radiation was in general significantly greater than the climatological average (1990 – 2010) in spring and summer. Although annual rainfalls were ~20% less than average (1990-2010) with several dry periods, July was particularly wet.

2021 annual mean concentrations of SO_2 and NO_2 were the lowest ever observed since 1986, beating (by little) the lowest records observed in 2020. This confirms the general trend of improvement in these air quality indicators over the last 3 decades, although a temporal impact of reduced activities due to COVID-19 epidemic waves cannot be ruled out. Annual mean O_3 concentrations and exposure indicators all indicate no significant improvement regarding O_3 pollution compared to 2020. Except for the number of acute O_3 pollution events (1 hr average O_3 > 180 µg/m³), O_3 pollution metrics remain high in 2021 compared to 10 – 30 years ago. This could be partly due to a decrease of O_3 titration by NO on the regional scale. There were no benzene data from year 2021 (due to technical problems), but benzene data from years 2018/2019/2020 show that benzene values are well below the European annual average limit value of 1.5 ppb (European Directive 2008/50/EC).

Daily $PM_{2.5}$ aerosol analyses showed that the concentration of $PM_{2.5}$ and of all its major components (SO_4^{2-}, NO_3^-, NH_4^+, POM and EC) reached a lowest record in 2021, unlike 2020 during which particulate air pollution was not particularly low. However, sampling and analytical issues may have biased downwards these measurements. $PM_{2.5}$ average chemical composition was dominated by carbonaceous species (POM: 48%, EC: 7%), followed by secondary inorganics (NH_4^+: 8%, NO_3^-: 14%, SO_4^{2-}: 12%). In 2021 the unaccounted mass average was 7%. As previously observed, there was a clear increase of NO_3^- contribution to $PM_{2.5}$ when shifting from cleaner ($PM_{2.5}$ < 10 µg/m³) to more polluted periods ($PM_{2.5}$ > 15 µg/m³) during cold and months. The long-term time series of PM concentrations still suggests a decreasing trend of - 1.0 µg m^{-3} yr^{-1} across the last 35 years.

Mean particle number size distributions were in 2021, as usual, generally bimodal, with a submicron mode at ca. 100 nm (dry) and a less pronounced coarse mode around 2 μm. The annual mean particle number concentration (average: 6600 cm^{-3}) was slightly less than in 2020 (-5%), and 10% less than during the 3 previous years. The increase in particle number concentration observed since 2014 (following a net decrease till 2011) therefore stopped. However, the aerosol light scattering coefficient stopped to decrease since 2015, while the aerosol light absorption coefficient did not. As a consequence, the aerosol single scattering albedo, which had been clearly decreasing since 2004, increased again across the 6 last years.

All aerosol extensive variables measured at the Atmospheric Observatory of Ispra (a few meters above ground level) have similar seasonal variations with summer minima. These variables are generally well correlated and lead to variable degrees of chemical, physical, and optical closure. In 2021, a reasonable overlap between the particle size distributions as measured with the DMPS and the APS was obtained for a particle density ranging between 1.0 and 1.9 g/cm³. This value is reasonably consistent with the average aerosol density of 1.02 g/cm³ and 1.45 g/cm³ determined for PM$_{2.5}$ and PM$_{10}$, respectively, from the regression between mass and volume concentrations in these two size fractions. However, it is quite unlikely that the density of PM$_{10}$ and PM$_{2.5}$ are so different from each other. Similarly, the mean mass extinction cross section (i.e., the extinction-to-mass ratio) of 3.7 m^2 g^{-1} obtained in 2021 is low compared to the value that can be estimated from the mean PM$_{2.5}$ chemical composition (4.3 – 4.6 m^2 g^{-1}). Nevertheless, direct measurement of the aerosol light extinction performed with the Cavity Attenuated Phase Shift (CAPS) monitor in 2021 are in excellent agreement with the light extinction values calculated from the light scattering and absorption measurements.

Aerosol vertical profiles were measured with the Raymetrics Raman LiDAR with a 1-minute resolution in 2021 until the end of July, and were discontinued since then due to low signal to noise ratio asking for the replacement of the laser. Before this, aerosol vertical profiles were obtained with a time coverage never reached so far.

The concentrations of the anthropogenic ions measured in rainwater (NO$_3^-$, SO$_4^{2-}$, and NH$_4^+$) in 2021 were all slightly less than in 2020, but the annual wet deposition fluxes of these main acidifying and eutrophying species (0.9, 2.1, and 1.3 g m^{-2} for SO$_4^{2-}$, NO$_3^-$, and NH$_4^+$, respectively) were almost the same as in both years, and less than across the 2000's (-42% and -55% for NO$_3^-$, and SO$_4^{2-}$, respectively, but -10% only for NH$_4^+$).

In-situ and remote sensing 2021 data listed by ACTRIS and EMEP as core variables have all been reported to EBAS within deadlines. They may be freely downloaded from these data centres (open access).

Fig. 51. The flux tower of 24 m at the Pinus pinea site in San Rossore

Source: JRC, 2022

5 Atmosphere – Biosphere flux monitoring at the forest station of San Rossore (IT-SR2)

5.1 Location and site description

The measurement site 'San Rossore' (43°43.9205'N, 10°17.45817E, 4 m a.s.l.), operated by the EC-JRC Air and Climate Unit (C5), is located in the Tenuta di San Rossore, inside the Parco Regionale Migliarino San Rossore Massaciuccoli (www.parcosanrossore.org), approximately 8 km west of Pisa and 1200 m east of the Tyrrhenian coast, in a Mediterranean forest ecosystem. The Climate Change and Air Quality Unit began to operate the predecessor site in the Parco San Rossore in 1999; the present location is running since 2013 in the same area, few hundreds of meters northeastward compared to the initial location.

The measurement site is located in an almost flat area with a morphology characterised by the presence of sandy dunes. The vegetation in the close proximity of the station is a pinewood plantation established in 1921 following artificial seeding. It is dominated by the evergreen species stone pine (*Pinus pinea* L.), with very sparse presence of black alder (*Alnus glutinosa* L.), white poplar (*Populus alba* L.), field helm (*Ulmus minor* Mill.), narrow-leaved ash (*Fraxinus angustifolia* L.) and holm oak (*Quercus ilex* L.), also known as evergreen oak. The average canopy height is approximately 19 m, whereas the needles start at about 16.5 m. The tree density in the proximity of the measurement station is on the order of 100 trees/ha for the dominant *Pinus pinea* L., with higher values for the secondary species of *Alnus glutinosa* L. found in few measurement plots. The understory vegetation is confined to the forest edges or canopy gaps and is very sparse. A remarkable feature of the plantation is the presence of narrow and long bands of soils with well-watered conditions, mostly stretched from North to South and at their very far end heading southwestward, toward the shore. These so-called "lame" are markedly different from the rest of the pinewood forest for flora, fauna and edaphic properties. Almost all the secondary species are indeed confined in these relatively quite small portions of the forest.

The green area index (GAI) of the forest, as estimated via digital hemispherical pictures (DHP) during 2019, is lying between 2.6 and 3.1 m^2 m^{-2} within the target area of the station.

The area has a Mediterranean – type climate within the sub-humid zone, with a mean annual rainfall of 876 mm yr^{-1} and a range of 534 – 1270 mm for the period 1980 – 2005. The long-term data were obtained from a meteorological station located at a distance of approximately 10 km and managed by the Regional Hydrologic Service of Tuscany. Rain falls mainly during autumn and winter with about 50% occurring between September and November, while the driest months are July and August. Water table is normally shallow compared to most of the ecosystems in the same climatic zone, which, together with the presence of the above mentioned "lame", makes the water availability to the tree roots higher than in common Mediterranean forests. The average annual temperature is 14.2 °C with the average temperature of the coldest month (January) being 7 °C and that one of the warmest month (August) being 25 °C. The wind regime is characterized by a sea – land breeze circulation, i.e. the air flows quite predictably from the west (sea) during the day and from east (land) during the night.

The scientific activities at the site are embedded into the ICOS initiative. ICOS (Integrated Carbon Observation System, www.icos-ri.eu) is one of the pan-European research infrastructure projects identified by the European Strategy Forum on Research Infrastructures (ESFRI) for implementation. After its preparatory phase planned for 2008 until 2013 with an extension towards 2015, during which monitoring infrastructure and technical procedures have been developed, it entered its operational phase with first stations officially labelled in 2019.

The San Rossore station has been labelled as ICOS Class 2 Ecosystem Station during the ICOS general assembly of November 2019 (Fig. 52), following the long term commitment initiated by the JRC Air and Climate Unit in 2013.

Two collaboration agreements (CA) have been concluded and signed or became operational in 2021. One with the Parco Migliarino San Rossore Massaciuccoli (CA Number 35609) and one with CNR-IRET (Consiglio Nazionale delle Ricerche - Istituto di Ricerca sugli Ecosistemi Terrestri) and SSSA-ISV (Scuola Superiore Sant'Anna – Istituto di Science della Vita) in the framework of a wide collaboration between the EC-JRC and the whole Pisa Research network (CA Number 35638). Both collaborations are aiming at further developing the scientific activity at the site and promoting the use of the JRC managed infrastructure by a wider range of users.

Table 8. ICOS class 2 Ecosystem Station core variables.

Core variables continuous	Core variables daily to monthly	Core variables yearly
CO_2, H_2O and energy fluxes	leaf area index	biomass (above ground)
wind speed and direction		soil carbon
CO_2 concentration vertical profile		
net radiation: • incoming/reflected global radiation • incoming/outgoing longwave radiation • albedo		
incoming / reflected Photosynthetic Active Radiation (PAR)		
		land-use history
temperature and relative humidity vertical profile		managements and natural disturbances
air pressure		C and N import and export on managed sites
precipitation, through-fall, snow depth		
soil heat flux		
ground water level		
soil temperature profile		
water content profile		

Source: JRC, 2022

Table 9. ICOS variables measured continuously during 2021 in San Rossore

FLUXES	CO_2, latent heat, sensible heat
METEOROLOGY	3D wind speed, temperature, relative humidity, pressure, precipitation
RADIATION	short & long wave incoming & outgoing, direct & reflected photosynthetic active radiation
SOIL	temperature profile, water content profile, heat flux, water table depth

Source: JRC, 2022

Fig. 52. ICOS Ecosystem Station Class 2 Certificate
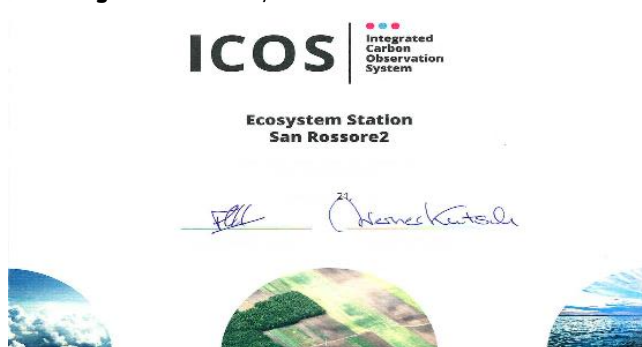
Source: ICOS, 2019

5.2   Measurements performed in 2021

During the course of 2021, all the core and mandatory measurements have been implemented in compliance with ICOS requirements and sent in near real time (NRT) mode to the corresponding database at ICOS Carbon Portal. The main variables measured in 2021 are summarised in Table 9.

During the year 2021 the station has fulfilled all ICOS requirements and standards, providing an almost seamless series of micrometeorological measurements to the ICOS database, jointly operated by the ICOS Carbon Portal and the ICOS Ecosystem Thematic Centre. In order to be fully compliant with ICOS requirements, also a regularly time spaced series of six field campaigns with digital hemispherical pictures (DHP) shooting has been implemented, to provide ICOS ETC with standardized indirect and non destructive measurements of green / leaf area index (GAI/LAI).

Having been fully operational and ICOS compliant during the whole year 2021, the San Rossore measurement dataset has been processed and released according to ICOS standard within the first ICOS Level2 Ecosystem data release and is freely available, previous registration, for preview and download at the following page through the ICOS Carbon Portal:

https://data.icos-cp.eu/portal/#%7B%22filterCategories%22%3A%7B%22project%22%3A%5B%22icos%22%5D%2C%22station%22%3A%5B%22iES_IT-SR2%22%5D%2C%22type%22%3A%5B%22etcArchiveProduct%22%5D%7D%7D.

Moreover, the collaboration with other partners of the flux monitoring network, initiated but not limited to ICOS stations in 2020, led to the data release Warm Winter 2020 by ICOS Carbon Portal, where all historical data for 73 ecosystem flux stations up to the end of 2020, including San Rossore, have been made openly available through the CC-BY licence at the following URL repository and with the specific DOI, respectively:

https://www.icos-cp.eu/data-products/2G60-ZHAK

https://doi.org/10.18160/2G60-ZHAK

The implementation of the CNR-IRET collaboration agreement resulted in the installation of a set of automatic dendrometers, provided by CNR-IRET, on six representative trees around the flux measurement system. This set of new instrumentation and measurements is helping the whole station in getting a more detailed characterization of the ecosystem, adding a variable that is part of the ICOS measurements suite, despite not mandatory for Class2 forest stations like San Rossore. Data are shared according to the well-defined data policy specified in the CA and collaboration is still active on the scientific exploitation and dissemination of the resulting dataset.

Finally, two new water table monitoring dwells have been made because of sand infiltration in the previous ones. Installations have been done following ICOS protocols and replacing the old sensors, corroded by time and prolonged exposure to direct contact with sand, other than simply to belowground water.

In the following sections, the instruments used are described and basic plots and analysis of the main variables measured during the course of 2021 are presented.

5.3   Description of the instruments

5.3.1   Infrastructural

5.3.1.1 Sensor location

The instruments for eddy covariance flux system, i.e. sonic anemometer and fast gas analyser, solar radiation and meteorological parameters are mounted on the top of the guided wire tower at a height of 24 m above ground, 5 m above the canopy top at 19 m.

Soil parameters are measured at an undisturbed soil plot approximately 20 m west of the tower.

A wooden hut complements the installation, hosting IT and communication equipment, a UPS system and is also used for storage.

5.3.1.2 Data acquisition

Eddy covariance flux data are stored with high frequency, i.e. 10 Hz, as chunks of 30 minutes on a local laptop connected to the sonic anemometer. In October this data acquisition system has been replaced by a Smartflux2 system from Licor (www.licor.com) that acquires all eddy covariance data digitally.

Data from the sensors located on the tower top are read every 10 s and averaged and stored every 30 minutes by a CR3000 data logger from Campbell (www.campbellsci.co.uk) also installed on the tower top. Soil measurements are handled the very same way by a CR1000 installed on the ground.

For eddy covariance flux data, the start time of every 30 minute measurement period is saved as the reference time, whereas for all other data, the end of the 30 minute measuring period is used. The time reference used for all San Rossore measurements is local solar time (UTC+1) to comply with ICOS requirements.

5.3.1.3 Power supply, IT & communication infrastructure

The fixed line power supply of 4 kW is locally backed up by an UPS system MSM 10 from Riello (www.riello-ups.de) to protect the system from transient power outages and provide an autonomous running time of approx. 19 hours for the installation. Computers and data loggers are connected via a local TCP/IP network. In addition, two cellular routers, one OnCell G3470A-LTE from Moxa and (www.moxa.com) one TK704U from Welotec as backup(www.welotec.com) provides internet access via the mobile 3G / 4G network. For safety reason at the remote site, a 3G repeater provides mobile phone coverage also on the forest ground in the vicinity of the site.

Measurement data is automatically transferred from San Rossore via ftp to a server in Ispra at 06:00 local solar time. Remote connection to a computer at the site can be established as well.

5.3.2   Ecosystem fluxes

5.3.2.1 Sonic Anemometer for 3D wind direction Gill HS-50

Sonic anemometers determine the three dimensional wind vectors at high frequency using the speed of sound. The Gill HS-50 (www.gill.co.uk) emits ultrasonic pulses between its pairs of transducers, measures the flight time of the pulses to the paired transducer and calculates the wind speed in the direction of the transducer pair (Fig. 53). Combining the results from the three transducer pairs, the 3 dimensional wind speed is calculated at a frequency of 10 Hz. After a rotation of the coordinate system during the data processing to align it to north, horizontal and vertical wind speeds and the wind direction are calculated besides their use for flux calculations. As the speed of sound measured with the anemometer depends on the temperature, the so-called sonic temperature is reported by the instrument as well.

Due to the absence of moving parts and the fact that no calibration is required, the instrument is very robust and reliable. Instrument servicing is done at the manufacturer's.

Fig. 53. Measurement principle of sonic anemometers (T: travelling time of sound pulses, L: distance between transducers, C: speed of sound, V: wind speed in direction of transducers)

$$T_2 = \frac{L}{C - V} \quad \text{and} \quad T_1 = \frac{L}{C + V}$$

therefore

$$V = \frac{L}{2}\left\{ \frac{1}{T_1} - \frac{1}{T_2} \right\} \qquad C = \frac{L}{2}\left\{ \frac{1}{T_1} + \frac{1}{T_2} \right\}$$
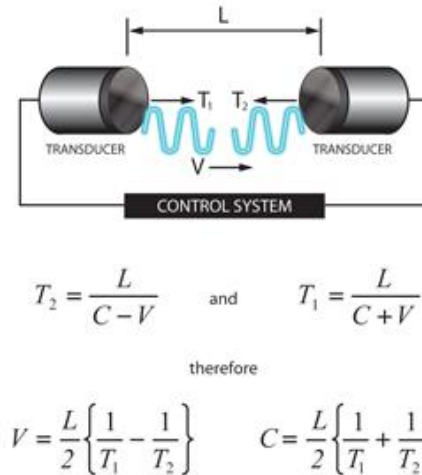
Source: www.gill.co.uk

5.3.2.2 Fast infrared gas analyser (IRGA) for CO_2 and H_2O concentration LI-7200 FM from Li-Cor

For the determination of CO_2 and H_2O fluxes with the eddy covariance technique, fast analysers (10 to 20 Hertz) for concentration measurements of the gases of interest are obligatory. At the San Rossore forest flux tower, a LI-7200 FM system from LI-COR (www.licor.com) has been installed, consisting of the LI-7200 enclosed CO_2 and H_2O analyser, the LI-7550 analyser interface unit, and the LI-7200-101 flow module. In October 2017 the system has been upgraded with a 2 µm pore size stainless steel particle filter and a heated tube at the inlet.

The LI-7200 is a high performance, non-dispersive, enclosed open path infrared CO_2 and H_2O analyser based on the infrared absorption of CO_2 and H_2O at ambient conditions that provides concentration measurements at a frequency of up to 20 Hz. With the flow module, ambient air is drawn into to analyser through the sample inlet at a set flow rate of 15 L/min. In the sample volume of 16.09 cm^3 (Fig. 54), light from the infrared source is absorbed at characteristic wavelengths for CO_2 and H_2O. This specific absorption is a function of the gas concentration in the sample volume. Using the absorption measurements at the CO_2 and H_2O wavelengths, at a non-absorbing wavelength, plus calibration factors and measured temperature and pressure, the LI-7200 reports molar densities, mass densities or mole fraction of the two gases.

Zero and span checks and calibrations are done regularly using zero gas from a cylinder plus a dew point generator (RH CAL from EdgeTech) and a CO_2 standard from a cylinder.

Fig. 54. LI-7200 analyser (red arrow indicates sampling volume)
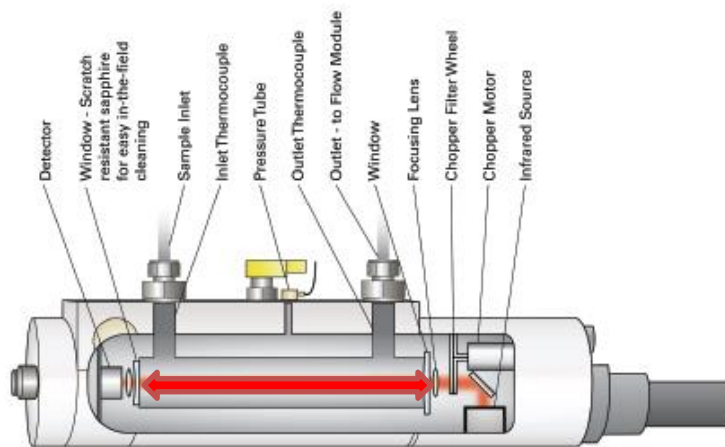
Source: www.licor.com

5.3.3 Radiation measurements

5.3.3.1 Net radiometer Kipp & Zonen CNR4

The net radiometer CNR 4 from Kipp & Zonen (www.kippzonen.com) measures the energy balance between incoming and reflected radiation in the short (305 – 2800 nm) and long (5-50 µm) wavelength range to obtain the net radiation at the earth's surface. The short wavelength range is measured with two CM3 pyranometers, one facing upwards and one downwards. For the long range, two CG3 pyrgeometers facing opposite directions are used. The design of the instrument ensures a field of view of 180° upwards and downwards for the respective sensors. The CNR 4 features a blower and heating system to minimise the influence of dew and frost on the radiation measurements.

The energy E_{short} of the short wave or so-called global (solar) radiation is calculated from the voltages provided by the CM3's using their sensitivity C_{CM3}:
$$E_{short} = V/C_{CM3} \qquad \text{Eq. 6}$$

To calculate the energy E_{long} of the long wave radiation from the reported voltages V, besides the sensitivities of the CG3's C_{CG3}, also the sensor temperature T measured with a PT-100 is needed:
$$E_{long} = V/C_{CG3} + 5.67 \cdot 10^{-8} \cdot T^4 \qquad \text{Eq. 7}$$

The net radiation E_{net} over all wavelengths is then easily calculated by adding the net radiation ($E^{up} - E^{down}$) for short and long wavelengths:
$$E_{net} = E_{short}^{up} + E_{long}^{up} - E_{short}^{down} - E_{long}^{down} \qquad \text{Eq. 8}$$

In addition, the albedo of the earth's surface defined as the ratio of outgoing to incoming solar radiation can be obtained with the instrument as well:
$$Albedo = E_{short}^{down} \Big/ E_{short}^{up} \qquad \text{Eq. 9}$$

Calibration and instrument checks at the factory are recommended every two years according to the manufacturer.

5.3.3.2 Photosynthetic active radiation LI-COR LI-190/R

The photosynthetic active radiation (PAR), i.e. the 400-700 nm range of the solar spectrum, is measured by a set of two LI-COR LI-190/R quantum sensors. The sensor facing upwards and downwards measure the incoming and reflected PAR components, respectively.

5.3.4 Meteorological sensors

5.3.4.1 Temperature & relative humidity Vaisala HMP 155

To measure ambient temperature and relative humidity, a combined thermohygrometer (Vaisala model HMP155, [www.vaisala.com)](www.vaisala.com) is installed into an aspirated radiation shield and mounted on top of the tower at an height of 24.3 from the soil surface, well above the tree canopy top.

5.3.4.2 Ambient air pressure Keller Druckmesstechnik PAA-41 & Vaisala PTB110

Ambient air pressure used to be measured with a PAA-41 capacitive pressure sensor from Keller Druckmesstechnik [(www.keller-druck.com)](www.keller-druck.com) using a ceramic measurement cell for enhanced reliability. It has been replaced in October 2020 by a PTB110 pressure sensor from Vaisala (www.vaisala.com).

5.3.4.3 Rain sensor UMS ARG 100/std

The ARG 100/std from UMS ([www.ums-muc.de)](www.ums-muc.de) is a tipping bucket type of rain gauge. It features a collecting funnel with a surface area of 500 cm² and a resulting resolution of 0.2 mm of rain fall per tip.

5.3.5 Soil instruments

5.3.5.1 Soil heat flux sensors HFP01 from Hukseflux

Three thermal sensors HFP01-SC from Hukseflux (www.hukseflux.com) have been buried ten centimetres underground in the undisturbed soil around the tower to obtain a good spatial averaging of the soil heat flux. The determination of the heat flux is based on measuring the temperature difference of two sides of a plate that is exposed to a heat flow using a number of thermocouples connected in series (Fig. 55), with the convention that positive values indicate a heat flux into the soil, a negative one heat flux out of the soil. Ignoring possible errors, the temperature difference between the hot and cold side of the sensor is proportional to the heat flow. As the thermocouples provide a voltage proportional to the temperature, the voltage output of the sensor is proportional to the heat flow across the sensor. The sensors used are "self-calibrating", hence once per day and always at

different time of the day they are calibrated through a short excitation of known voltage, following ICOS requirements. Corresponding data are calibrated and flagged, before being sent to ICOS database. This feature has been implemented by the end of 2021, while before it was not activated.

Fig. 55. Sketch of a soil heat flux sensor
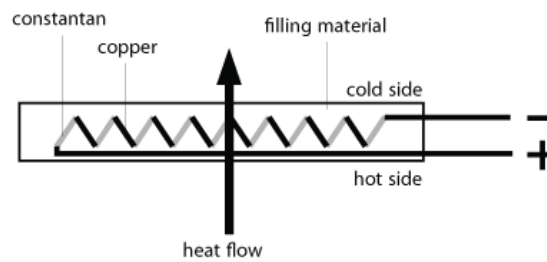
Source: www.wikipedia.org

5.3.5.2 Soil water content vertical profile with TRIME-TDR from IMKO

Profile measurements of soil water content are performed using the TRIME-TDR (Time domain Reflectometry with Intelligent MicroElements with) from IMKO (www.imko.de). Based on Time-Domain-Reflectometry, the sensor generates high frequency electromagnetic pulses that propagate along a wave guide and are reflected back into the sensor. Depending on the dielectric constant of the material surrounding the waveguide, the round-trip time of the hf-pulses varies between some tens and thousand picoseconds. As the dielectric constant of soil and thus the round-trip time strongly depends on the soil moisture content, measuring this time gives the water content of the soil surrounding the sensor. Burying several sensors at depths of 5, 15, 25, 45, 90 cm below ground provides the soil humidity profile.

5.3.5.3 Soil temperature profile with Th3-v probe from UMS

For the measurement of soil temperatures at different depths, a Th3-v probe from UMS (www.ums-muc.de) is used. This probe features a convenient set of 6 temperature probes in a profile system buried at 0, 5, 15, 25, 45, and 95 cm below the transition of organic and mineral soil at approx. 5 cm below the surface.

5.3.5.4 Ground water level CS456-SA from Campbell Scientific

The ground water level is monitored with a Diver from Campbell Scientific (www.campbellsci.co.uk). The device is placed in a water filled hole, 2.6 m below ground, and measures directly the difference between water and atmospheric pressure ($p_{Diff} = p_{Diver} - p_{baro}$). This gives the water column above the sensor *WC*, and together with the known sensor depth below ground *CL* and the top of the container level (*TOC*), the water table height *WL* can be easily calculated (see also Fig. 56):

$$WL = TOC - CL - WC \text{ with } WC = 9806.65 \cdot \frac{(p_{Diver} - p_{baro})}{\rho \cdot g} \qquad \text{Eq. 10}$$

where g = 9.81 m/s², ρ = 1000 kg/m³

Fig. 56. Principle of water level calculation using the Diver (CL: cable length, TOC: top of container, WC: water column, WL: water level relative to a reference, p: pressure).
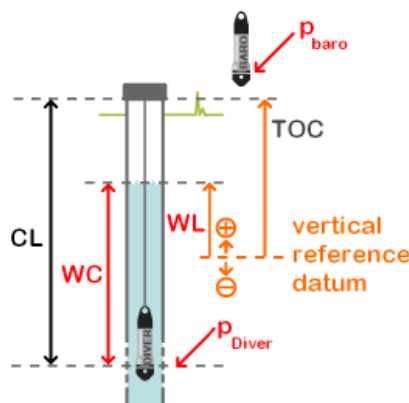
Source: www.swstechnology.com.

Fig. 57. Time series of the daily averaged air temperature (red) and daily total precipitation (blue) records at the San Rossore forest station in 2021.
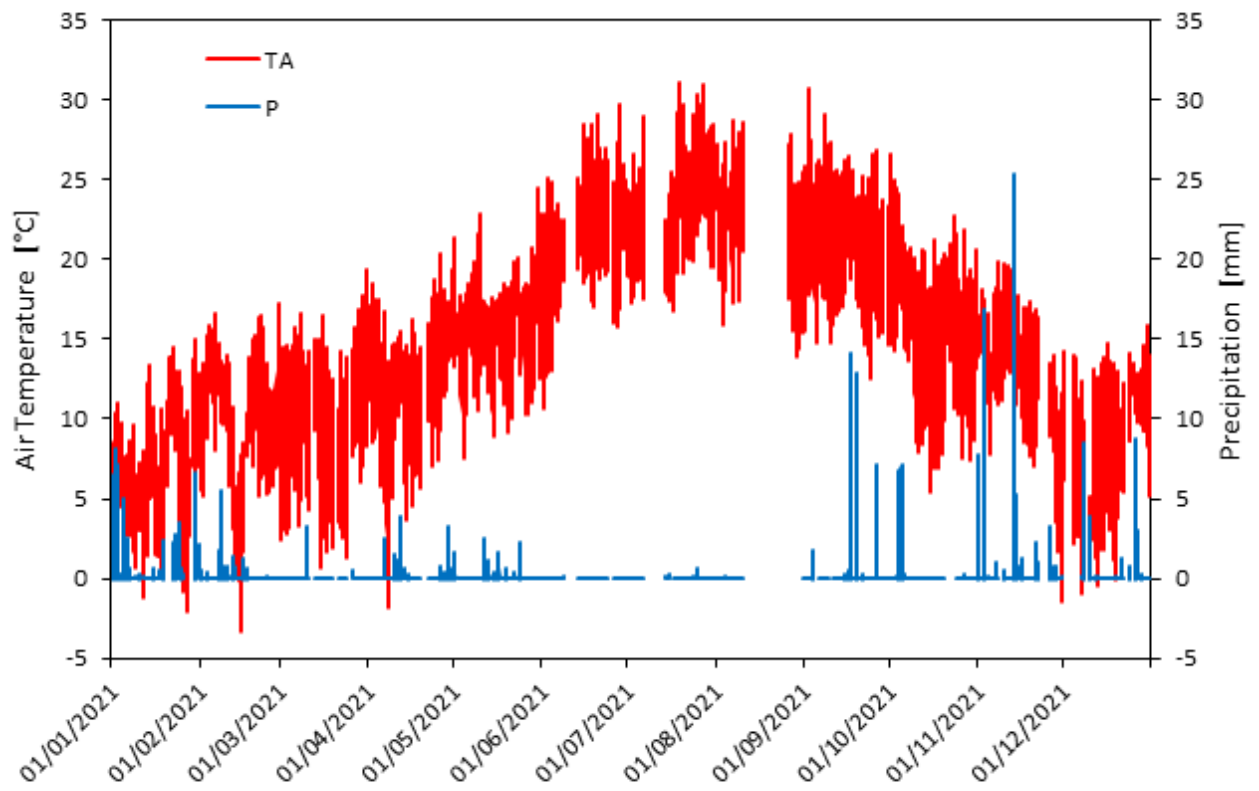
Source: JRC, 2022

5.4 Results of the year 2021

5.4.1 Meteorology

Annual air temperature averages and precipitation cumulative are reported for the period 2013-2021 in Table 10.

Hydrometeorological records for 2021 are not significantly different from other years, confirming a typical Mediterranean climate, with a warm and dry summer (days 170 – 255), mild winter (days 1-60 and 335-366), and very wet fall months (days 270 – 350) as shown in Fig. 57. The remarkable features are the amount of precipitation in the whole year (803 mm), which is the lowest record since measurements are performed, and in particular the very low precipitation amount over June, July and August (see also section 5.4.2).

Table 10. Yearly mean air temperature and cumulative precipitation at the San Rossore ICOS Ecosystem station.

Year	2013	2014	2015	2016	2017	2018	2019	2020	2021
Air Temperature (°C)	15.02	15.92	15.87	15.61	15.43	16.05	15.76	15.59	15.28
Precipitation (mm)	1132	1525	924	1123	853	914	1230	1115	803

Source: JRC, 2022

Fig. 58. Measurements of soil temperature at six different depths in the ground of San Rossore forest during 2021.
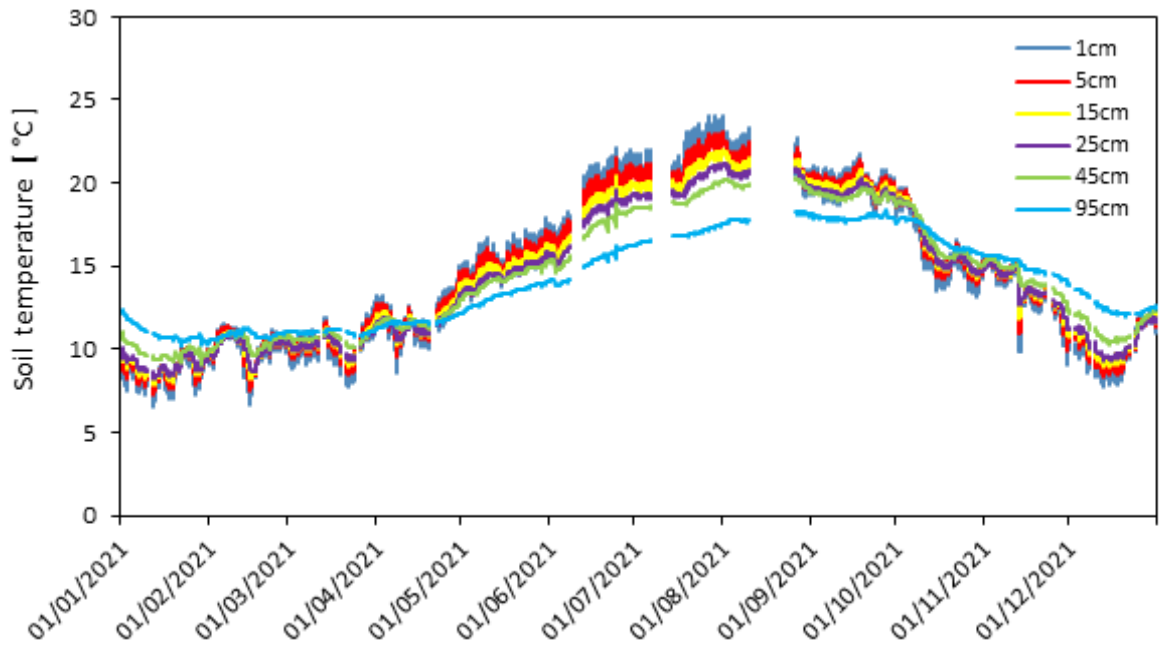
Source: JRC, 2022

Fig. 59. Measurements of soil water content at five different depths in the ground of San Rossore forest during 2021.
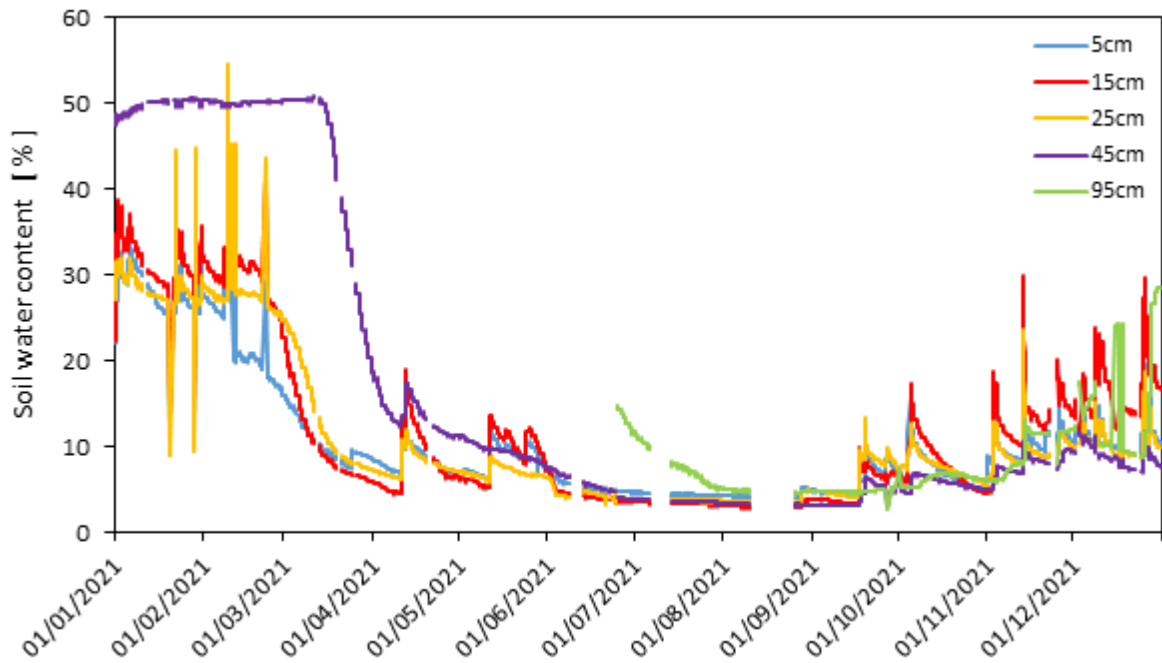
Source: JRC, 2022

5.4.2 Soil meteo-climatic variables

All the measurements collected in the soil pits by the instrumentation described in the section 3 above, have been analysed and briefly reported hereafter. Measurements of soil temperature (TS) at six depths are shown in Fig. 58, while soil water content (SWC) and water table depth (WTD) records are plotted in Fig. 59 and Fig. 60, respectively. Annual variations are consistent with the hydrometeorological cycle of the Mediterranean summer: of particular relevance is the length of the dry period, that in summer of 2021 lasted for more than four months, without detectable rain events from the beginning of June until the middle of September.

The very low amount of precipitation during the summer determined a scarce water availability during this season, as is perhaps frequently the case in Mediterranean climates, but also a limited recharge during the autumn, as can be seen by the level of SWC that remained substantially lower in the final part of 2021 compared to the winter months (Fig. 59). Similarly, the WTD remained substantially deeper than the level attained in the winter months at the beginning of the year (Fig. 60). This low level of soil water recharge could have carry-over effects on the 2022 ecosystem functionality and suggest further investigations.

Fig. 60. Measurements of the water table depth in the ground of San Rossore forest (averages of two distinct spatial locations) during 2021.
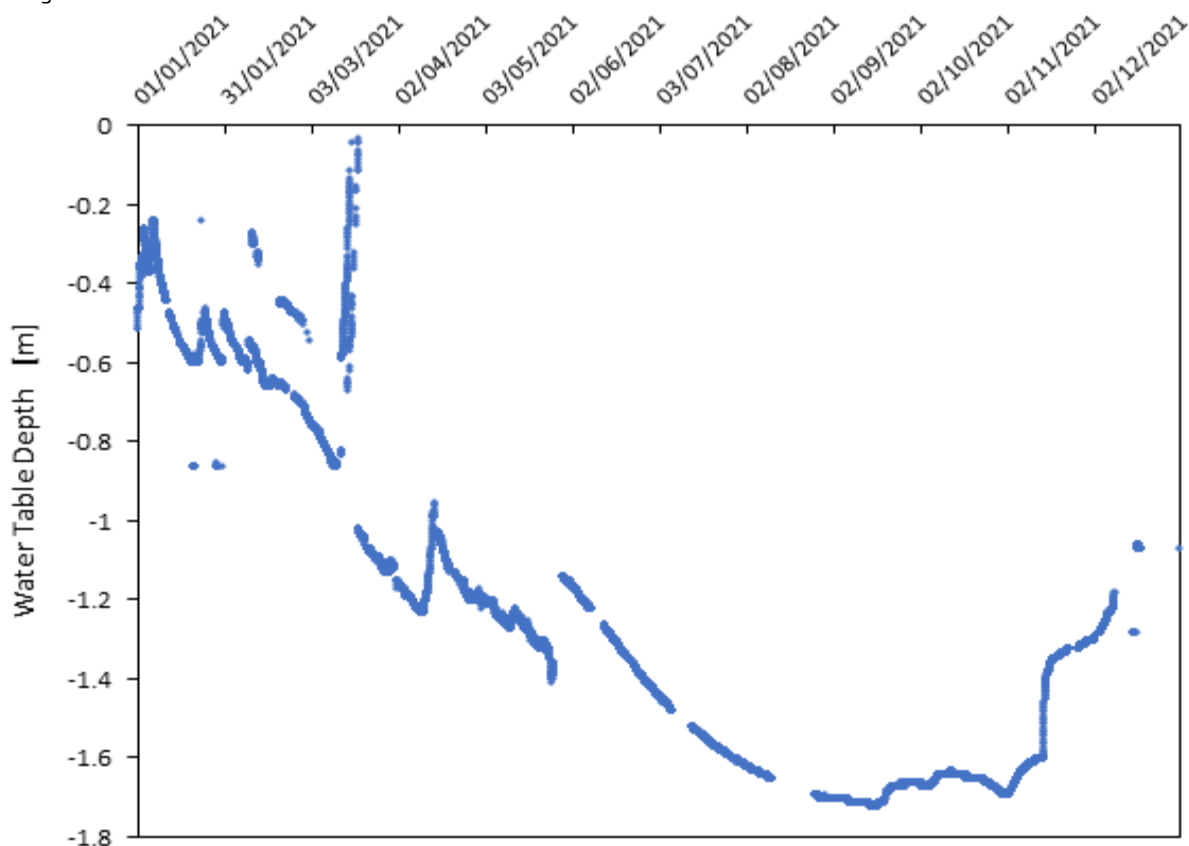
Source: JRC, 2022

Fig. 61. Cumulative sum of the Net Ecosystem Exchange (NEE) of carbon from the San Rossore forest during the whole 2021.
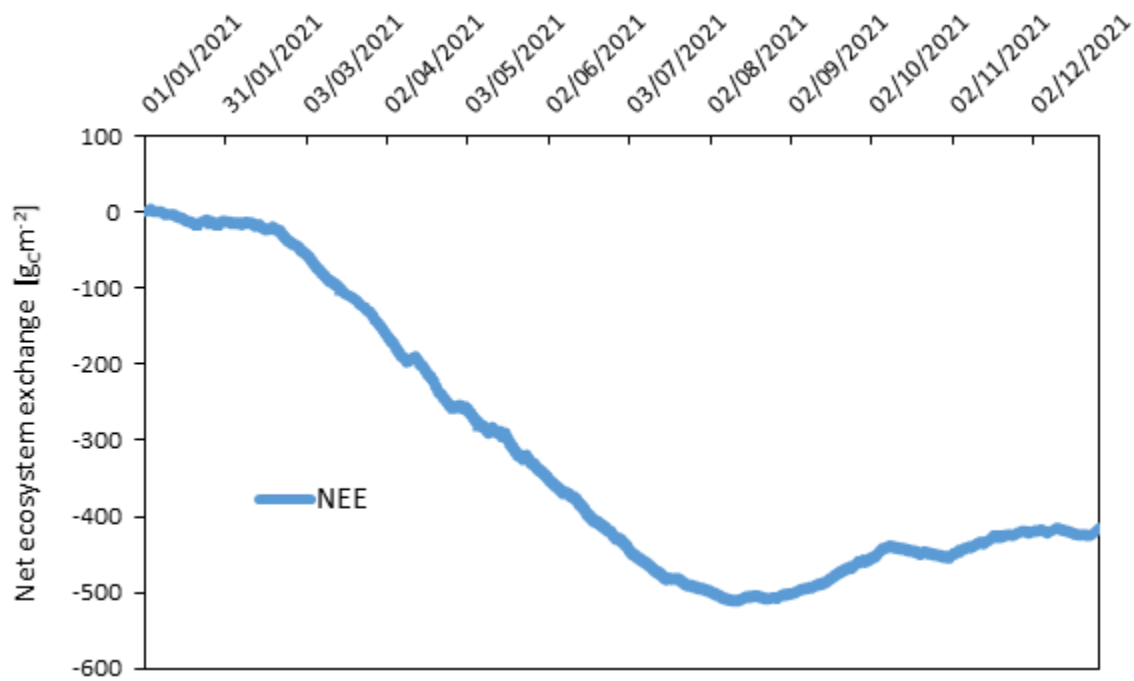
Source: JRC, 2022

Fig. 62. Cumulative sum of the three major components of the carbon cycle in the forest of San Rossore during 2021: Net Ecosystem Exchange (NEE) of carbon, Ecosystem respiration (Reco) and Gross Primary Production (GPP)/Photosynthesis, as resulting from the ICOS-L2 processed data. The NEE is directly measured, while Reco and GPP are derived through partitioning.

Source: JRC, 2022

76
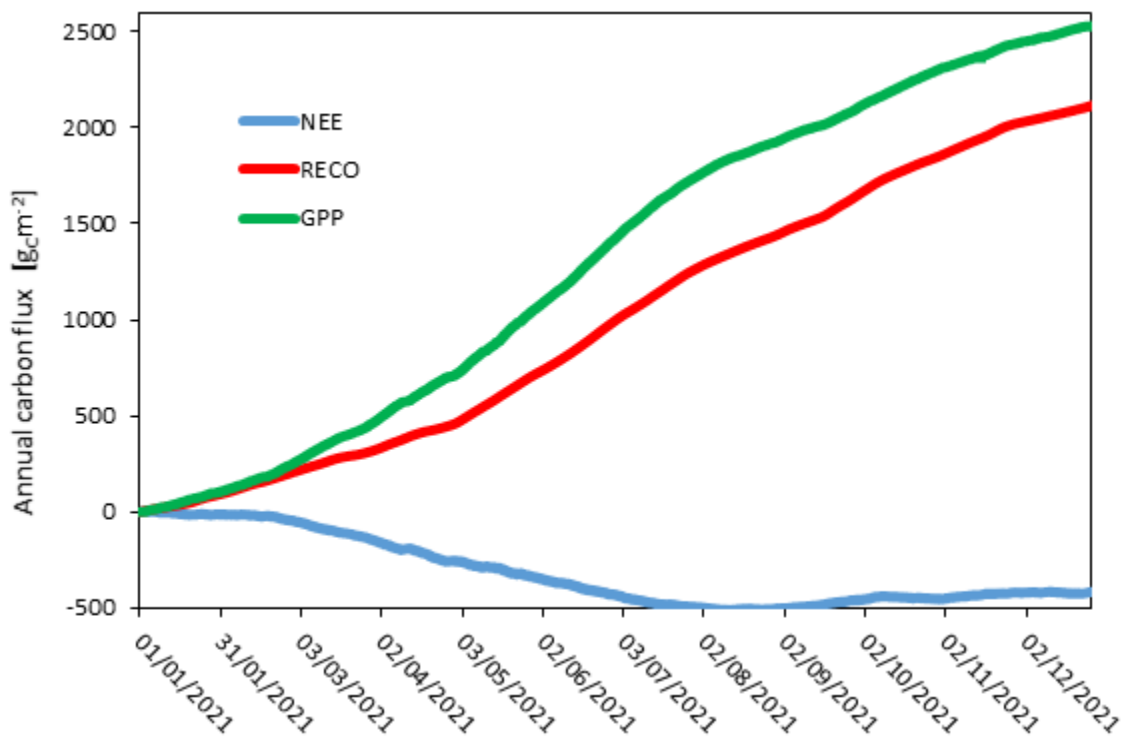
5.4.3   Flux measurements

In Fig. 61 and Fig. 62, the cumulative sums of Net Ecosystem Exchange of carbon (NEE) is plotted, alone or alongside with the two components in which it is partitioned, i.e. photosynthesis (GPP) and total ecosystem respiration (RECO), respectively.

The trend of the three variables follows the expected behaviour for a Mediterranean dry and lowland forest, with a sustained growth in the spring and early summer months, while two distinct dormancies can be usually detected: one in the colder winter months and a second one in the extremely hot and dry late summer. Nonetheless, the final annual budget of carbon exchanged between the forest and the atmosphere, i.e. -413 $g_cm^{-2}y^{-1}$ (where the minus sign denotes uptake by the ecosystem) represents a substantially high carbon sink, larger than any other year since the beginning of measurements in San Rossore. Further analysis will be needed to assess the actual drivers of such large uptake, perhaps similar to what has been estimated for 2020.

Table 11. Yearly net ecosystem exchange of carbon at the San Rossore ICOS Ecosystem station since the start of measurements. The two rows correspond to slightly different processing methods, since the official ICOS L2 data release is only available since 2020, i.e. after the labelling of the station (December 2019).

Variable/Year	2013	2014	2015	2016	2017	2018	2019	2020	2021
NEE ICOS (WW2020) ($g_cm^{-2}y^{-1}$)	394.5	-68.8	-281.2	-149.8	-145.4	-233.4	-201.2	-317.3	na
NEE ICOS L2 ($g_cm^{-2}y^{-1}$)	na	na	na	na	na	na	na	-382.4	-413.0

Source: JRC, 2022

5.4.4   Ancillary measurements

Finally, it is worth to mention that a series of additional biometric measurements have been collected on a campaign mode, the so-called "ancillary" measurements that constitute a fundamental complement to the set of continuously sampled and recorded micrometeorological measurements, for the correct interpretation of ecosystem behaviour. In particular, at San Rossore the following ancillary measurements have been collected during 2021:

- six different field surveys for collection of Digital Hemispherical Pictures in order to provide a time course non-destructive measurement series of the leaf area index (LAI)
- One assessment of the above ground wood biomass (AGB) and of the herbaceous biomass in the understorey of the forest at the peak of the growing season
- One collection of leaf samples during the winter for elemental and nutrient analysis (C, N, P, K, Fe, Cu, Mg, …) and leaf to mass area ratio determination
- One complete soil sampling according to ICOS prescription, performed by specifically hired subcontractors expert in the field, who were already working for the ICOS-Italy network of ecosystem station. EC-JRC staff participated to the field survey to coordinate the sampling performers, assisting them with the necessary knowledge of the site and ensuring the full compliance with ICOS stringent requirements. This huge and demanding field surveys was required by ICOS Instructions and protocols and it is mandatory once every 10 years to characterize the carbon pool of the soil. Samples are still under treatment and preparation and will be sent to the responsible ICOS ETC laboratory as soon as it will re-open after logistic renovation

All the above mentioned ancillary measurements and samples have been collected following the most updated ICOS instructions and made available to the ICOS-ETC (Ecosystem Thematic Center) distributed in Italy (Universitá degli Studi della Tuscia, Viterbo), Belgium (Universiteit Antwerpen, Antwerpen) and France (INRA, Bordeaux) for an initial forest description and characterization and for long term repository.

6 Conclusions

A comprehensive set of essential atmospheric variables has been measured in 2021 at the European Commission Atmospheric Observatory (JRC-Ispra site) to continue the assessment of the impact of European policies and international conventions on air pollution and climate forcing that started in 1985. The variables measured in 2021 included greenhouse gas concentrations (CO_2, CH_4), radon (^{222}Rn) activity concentration, short-lived gaseous and particulate pollutant concentrations (CO, SO_2, NO, NO_2, O_3, NH_3, $PM_{2.5}$ and its main ionic and carbonaceous constituents), atmospheric particle micro-physical characteristics (number concentration and size distribution) and optical properties (light scattering absorption and extinction in-situ, light scattering and extinction vertical profiles remotely), and eutrophying and acidifying species (SO_4^{2-}, NO_3^-, NH_4^+) wet deposition. On-line measurements data are visible in real time at http://abc-is.jrc.ec.europa.eu/.

Vegetation ⇆ atmosphere exchanges (CO_2, H_2O and heat) were measured at our Mediterranean Forest Flux Station of San Rossore, backed up by meteorological and pedological measurements.

All measurements have been performed under international projects and programmes including ICOS (Integrated Carbon Observation System), ACTRIS (Aerosols, Clouds and Trace gases Research Infra-Structure), EMEP (co-operative Programme for Monitoring and Evaluation of the long range transmission of air pollutants in Europe) and GAW (Global Atmosphere Watch), each of which requires the use of standard methods and scales, and the participation in quality assurance activities. The JRC has a leading role in ACTRIS and EMEP regarding the quality assurance for carbonaceous aerosol measurements. Data obtained at the Atmospheric Observatory are submitted to international open data bases (ICOS Data Portal, www.ingos-infrastructure.eu, ACTRIS Data Portal, www.europe-fluxdata.eu, fluxnet.ornl.gov) and can be freely downloaded (partly in real-time) from these web sites. The data we produce are used in European wide assessments, for model inputs and validation, and for calibrating satellite airborne sensors. The European Commission Atmospheric Observatory 2021 report presents the data produced during the past year in light of the measurements data obtained for previous years.

Greenhouse gas (GHG) concentrations have been measured at the JRC Ispra site since October 2007, and at the current Atmospheric Observatory tall tower since December 2016. GHG measurements have been since then performed in compliance with ICOS recommendations and the GHG Observatory received the ICOS certificate on 30 November 2018. CO_2 concentrations show a typical seasonal pattern largely controlled by fossil fuel emissions and seasonal fluxes of CO_2 between the atmosphere and terrestrial ecosystems. CH_4 concentrations do not show any obvious seasonal cycles. However, deviations from baseline concentrations provide information about regional and larger scale European CH_4 sources. From selected daytime measurements, we derived mean increasing trends between 2017 and 2021 of +2.1 ppm yr^{-1} for CO_2 (to be compared with the global trend of 2.4 ppm yr^{-1}) and +7.2 ppb yr^{-1} for CH_4 (vs. global trend = 11.7 ppb yr^{-1}).

Atmospheric pollution has been characterised at the JRC-Ispra site since 1986. In 2021, SO_2, NO, NO_2 and PM annual mean concentrations reached their lowest records, in line with the improvement in these air quality indicators observed across the last 3 decades. In contrast, O_3 exposure indicators did not improve in 2021 compared to the previous years, and remained high compared to 10 – 30 years ago. Several COVID-19 epidemic waves impacted human mobility between January and April 2021. This could have affected pollutant emissions during this period, but changes in air pollutant concentrations observed in 2021 cannot be directly attributed to COVID without support from modelling. $PM_{2.5}$ average chemical composition was dominated by carbonaceous species (POM: 48%, EC: 7%), followed by secondary inorganics (NH_4^+: 8%, NO_3^-: 14%, SO_4^{2-}: 12%). As previously observed, there was a clear increase of NO_3^- contribution to $PM_{2.5}$ when shifting from cleaner ($PM_{2.5} < 10$ µg m^{-3}) to more polluted periods ($PM_{2.5} > 15$ µg m^{-3}) during cold months. $PM_{2.5}$ (from gravimetric analyses at 20% RH) annual mean mass concentration (12 µg m^{-3}) was well below the EU annual limit value (25 µg m^{-3}). The long-term time series of PM concentrations still suggests a decreasing trend of -1.0 µg m^{-3} yr^{-1} over the past 35 years. The increase in particle number concentration observed since 2014 stopped after winter 2017, and the annual average (6600 cm^{-3}) was in 2021 5% less than in 2020, and 10% less than during the 3 previous years. The trends in aerosol physics and chemistry are reflected in the trends of aerosol optical properties: The aerosol single scattering albedo (0.82 in 2021) has been increasing since 2014. The 2021 annual wet deposition fluxes of the main acidifying and eutrophying species NH_4^+, NO_3^-, and SO_4^{2-} (0.9, 2.1, and 1.3 g m^{-2}, respectively) were very similar to 2020 values, and 26 – 28% less than during the 2010's for both NO_3^- and SO_4^{2-}. In contrast, there is no clear decreasing trend in NH_4^+ wet deposition across the last 2 decades.

The forest flux station in San Rossore has been operated according to ICOS recommendations since 2013 and obtained the official label of ICOS Class 2 Ecosystem Station in November 2019. Preliminary atmosphere ⇆ vegetation net ecosystem exchange (NEE) data obtained in 2021 suggest that the pine tree forest was a larger net sink for CO_2 in 2021 (-410 gC m^{-2}) compared to previous years.

References

Adam, M., Putaud, J. P., Martins dos Santos, S., Dell'Acqua, A., and Gruening, C., Aerosol hygroscopicity at a regional background site (Ispra) in Northern Italy, *Atmos. Chem. Phys.*, 12, 5703–5717, 2012.

Anderson, T.L., and Ogren, J.A., Determining aerosol radiative properties using the TSI3563 integrating nephelometer, *Aerosol Sci. Technol.*, 29, 57-69, 1998.

Arnott, W.P., Hamasha, K., Moosmüller, H., Sheridan, P.J., and Ogren, J.A., Towards aerosol light-absorption measurements with a 7-wavelength Aethalometer: Evaluation with a photoacoustic instrument and a 3 wavelength nephelometer, *Aerosol Sci. Technol.*, 39, 17-29, 2005.

Bergamaschi, P., and Brunner, D., Analysis of the sensitivity of atmospheric measurements at the JRC Ispra Atmosphere - Biosphere - Climate Integrated monitoring Station, Footprint analysis based on FLEXPART-COSMO model, EUR 27131, Publications Office of the European Union, Luxembourg 2015.

Cavalli, F., Putaud, J.P., Toward a standardised thermal-optical protocol for measuring atmospheric organic and elemental carbon: the EUSAAR protocol, *Atmos. Meas. Tech.*, 3, 79-89, 2010.

Cavalli, F., Alastuey, A., Areskoug, H., Cech, J., Ceburnis, D., Genberg, J., Harrison, R.M., Jaffrezo, J.L., Kiss, G., Mihalopoulos, N., Perez, N., Quincey, P., Schwarz, J., Sellegri, K., Spindler, G., Theodosi, C., Yttri, K.E., Aas, W., Putaud, J.P., A European aerosol phenomenology -4: harmonized concentrations of carbonaceous aerosol at 10 regional background sites across Europe. *Atmos. Environ.*, 144, 133-145, 2016.

Cooke, W.F., Liousse, C., Cachier, H., and Feichter, J., Construction of a 1x1°fossil fuel emission data set for carbonaceous aerosol and implementation and radiative impact in the ECHAM4 model, *J Geophys. Res.*, 104; 22,137-22, 1999.

EMEP manual for sampling and chemical analysis (1995). *EMEP/CCC-Report 1/95.* (*Revised 1996; 2001; 2002),* 1995.

European Directive 2008/50/EC, On ambient air quality and cleaner air for Europe, 2008.

Gruening C., et al., JRC Ispra EMEP-GAW regional station for atmospheric research: 2008 report, EUR 24088 EN, 2009.

Hess, M., Koepke, P., Schult, I., Optical Properties of Aerosols and Clouds: The Software Package OPAC, *Bull. of Am. Meteorol. Soc.*, 79; 831-844, 1998.

Jensen, N. R., Gruening, C., Adams, M., Cavalli, F., Cavalli, P., Grassi, F., Dell'Acqua, A., Martins Dos Santos, S., Roux, D., Putaud, J.-P. JRC Ispra EMEP – GAW regional station for atmospheric research, 2009 report, EUR 24678 EN, 2010.

Kalabokas, P., Jensen, N. R., Roveri, M., Hjorth, J., Eremenko, M., Cuesta, J., Dufour, G., Foret, G., and Beekmann, M.: A study of the influence of tropospheric subsidence on spring and summer surface ozone concentrations at the JRC Ispra station in northern Italy, *Atmos. Chem. Phys.*, 20, 1861–1885, doi.org/10.5194/acp-20-1861-2020, 2020.

Kiehl, J. T., Schneider, T. L., Rasch, P. J., Barth, M. C., Wong, J., Radiative forcing due to sulfate aerosols from simulations with the National Center for Atmospheric Research Community Climate Model, Version 3 (Paper 1999JD900495), *J. Geophys. Res.,* 105; 1441-1458, 2000.

Koffi, E. N., Bergamaschi, P., Karstens, U., Krol, M., Segers, A., Schmidt, M., Levin, I., Vermeulen, A. T., Fisher, R. E., Kazan, V., Klein Baltink, H., Lowry, D., Manca, G., Meijer, H. A. J., Moncrieff, J., Pal, S., Ramonet, M., Scheeren, H. A., and Williams, A. G.: Evaluation of the boundary layer dynamics of the TM5 model over Europe, *Geosci. Model Dev.*, 9, 3137-3160, doi.org/10.5194/gmd-9-3137-2016, 2016.

Lan, X., Dlugokencky, E.J., Mund, J.W., Crotwell, A.M., Crotwell, M.J., Moglia, E., Madronich, M., Neff, D. and Thoning, K.W., Atmospheric Methane Dry Air Mole Fractions from the NOAA GML Carbon Cycle Cooperative Global Air Sampling Network, 1983-2021, Version: 2022-07-28, doi.org/10.15138/VNCZ-M766, 2022.

Lan, X., Dlugokencky, E.J., Mund, J.W., Crotwell, A.M., Crotwell, M.J., Moglia, E., Madronich, M., Neff, D. and Thoning, K.W., Atmospheric Carbon Dioxide Dry Air Mole Fractions from the NOAA GML Carbon Cycle Cooperative Global Air Sampling Network, 1968-2021, Version: 2022-07-28, doi.org/10.15138/wkgj-f215, 2022.

McMurry, P., Wang, X., Park, K., and Ehara, K. The relationship between mass and mobility for atmospheric particles: A new technique for measuring particle density, *Aerosol Sci. Tech.*, 36, 227–238, 2002.

Mira-Salama, D., Van Dingenen, R., Gruening, C., Putaud, J.-P., Cavalli, F., Cavalli, P., Erdmann, N., Dell'Acqua, A., Dos Santos, S., Hjorth, J., Raes, F., Jensen, N.R., Using Föhn conditions to characterize urban and regional sources of particles, *Atmospheric Research* 90, 159–16, 2008.

Mueller, T., *Development of correction factors for Aethalometers AE31 and AE33, ACTRIS-2 workshop*, Athens, http://wmo-gaw-wcc-aerosol-physics.org, 2015.

Petron, G., Crotwell, A.M., Crotwell, M.J., Dlugokencky, E.J., Madronich, M., Moglia, E., Neff, D., Thoning, K.W., Wolter, S., Mund, J.W., Atmospheric Carbon Monoxide Dry Air Mole Fractions from the NOAA GML Carbon Cycle Cooperative Global Air Sampling Network, 1988-2021, Version: 2022-07-28, doi.org/10.15138/33bv-s284, 2022.

Petzold, A., H., Schönlinner, M., Multi-angle absorption photometry - A new method for the measurement of aerosol light absorption and atmospheric black carbon, *Journal of Aerosol Science*, 35 (4), 421-441, 2004.

Putaud, J.-P., et al. (21 authors), A European aerosol phenomenology—2: chemical characteristics of particulate matter at kerbside, urban, rural and background sites in Europe. *Atmospheric Environment*, 38, 2579-2595, doi:10.1016/j.atmosenv.2004.01.041, 2004.

Putaud, J.-P., et al. (39 authors), A European aerosol phenomenology—3: Physical and chemical characteristics of particulate matter from 60 rural, urban, and kerbside sites across Europe. *Atmospheric Environment*, 44, 1308-1320, doi.org/10.1016/j.atmosenv.2009.12.011, 2010.

Putaud, J.P., Cavalli, F., Martins dos Santos, S., Dell'Acqua, A., Long-term trends in aerosol optical characteristics in the Po Valley, Italy, *Atmos. Chem. Phys.*, 14, 9129–9136, 2014.

Putaud, J.P., Arriga, N., Cavalli, F., Dell'Acqua, A., Duerr, M., Goded, I., Grassi, F., Jensen, N.R., Lagler, F., Manca, G., Martins Dos Santos, S., Matteucci, M., Passarella, R., Pedroni, V., The European Commission Atmospheric Observatory: 2020 report, EUR 31078 EN, Publications Office of the European Union, Luxembourg, doi:10.2760/6061, 2022.

Putaud, J.-P., Pozzoli, L., Pisoni, E., Martins Dos Santos, S., Lagler, F., Lanzani, G., Dal Santo, U., and Colette, A.: Impacts of the COVID-19 lockdown on air pollution at regional and urban background sites in northern Italy, *Atmos. Chem. Phys.*, 21, 7597–7609, doi.org/10.5194/acp-21-7597-2021, 2021.

Russell, L.M.: Aerosol organic-mass-to-organic carbon ratio measurements, *Environ. Sci. Technol.*, 37, 2982-2987, 2003.

Schmid, O., et al., Spectral light absorption by ambient aerosols influenced by biomass burning in the Amazon Basin I: comparison and field calibration of absorption measurements techniques, *Atmos. Chem. Phys.*, 6, 3443-3462, 2006.

Stratmann, F., Wiedensohler, A., A new data inversion algorithm for DMPS-measurements. *J. Aerosol Sci.*, 27 (Suppl 1), 339-340, 1996.

Thoning, K.W., Tans, P.P., Komhyr, W.D., Atmospheric carbon dioxide at Mauna Loa Observatory, 2. Analysis of the NOAA/GMCC data, 1974-1985., *J. Geophys. Res.*, 94, 8549-8565, 1989.

Van Dingenen, R., et al. (28 authors), A European aerosol phenomenology –1: Physical characterization of particulate matter at kerbside, urban, rural and background sites in Europe, *Atmospheric Environment*, 38, 2561-2577, doi:10.1016/j.atmosenv.2004.01.040, 2004.

Weingartner, E., Saathoff, H., Schnaiter, M., Streit, N., Bitnar, B., and Baltensperger, U., Absorption of light by soot particles: determination of the absorption coefficient by means of aethalometers, *J. Aerosol Sci.*, 34, 1445-1463, 2003.

Weitkamp, C. (editor), LIDAR Range-Resolved Optical Remote Sensing of the Atmosphere, *Springer*, New York, 2005.

WHO, Health risks of ozone from long-range transboundary air pollution, 2008.

Zahorowski, W., Chambers, S. D., Henderson-Sellers, A., Ground based radon-222 observations and their application to atmospheric studies, *J. Environ. Radioact.*, 76, 3-33, 2004.

List of abbreviations and definitions

ACTRIS: Aerosol Cloud and Trace gas Reseach Infrastructure, *www.actris.net*

Aeolus: European Space Agency's wind mission, *www.esa.int/Applications/Observing_the_Earth/Aeolus*

ARPA Lombardia: Agenzia Regionale per la Protezione dell'Ambiante, *www.arpalombardia.it*

Calipso: Cloud-Aerosol Lidar and Infrared Pathfinder Satellite Observation, *www.nasa.gov/mission_pages/calipso/main*

CCC: Chemical Co-ordinating Centre of EMEP, *www.nilu.no/projects/ccc*

CEN: European Committee for Standardisation, *www.cen.eu/cen/pages/default.aspx*

CLRTAP: Convention on Long-range Transboundary Air Pollution, *www.unece.org/env/lrtap/welcome.html*

D_p: particle aerodynamic, mobility or volume equivalent (according to context) diameter.

EARLINET, European Aerosol Research Lidar Network, *www.earlinet.org*

EBAS: EMEP data base, ebas.nilu.no

EBC: light absorption Equivalent Black Carbon

EC: Elemental Carbon

ECAC: European Centre for Aerosol Calibration), *www.actris-ecac.eu*

EMEP: co-operative programme for monitoring and evaluation of the long-range transmission of air pollutants in Europe, *www.emep.int*

EIEP: European Industrial Emissions Portal*, industry.eea.europa.eu*

ESA: European Space Agency, *www.esa.int*

EUSAAR: European Supersites for Atmospheric Aerosol Research, *www.eusaar.net*

GAW: Global Atmosphere Watch, *www.wmo.int/pages/prog/arep/gaw*

GHG: Greenhouse Gas

ICOS: Integrated Carbon Observation System, *www.icos-ri.eu*

InGOS: Integrated non CO2 Greenhouse gas Observing System, *www.ingos-infrastructure.eu*

JRC: Joint Research Centre, *ec.europa.eu/info/departments/joint-research-centre_en*

NEE: Net Ecosystem Exchange

NEP: Net Ecosystem Productivity

NMHC: Non-Methane HydroCarbons

OC: Organic Carbon

PM: Particulate Matter

POM: Particulate Organic Matter

QA/QC: Quality Assurance / Quality Control

Reco: Ecosystem Respiration

WDCA: World Data Centre for Aerosol, *www.gaw-wdca.org*

WMO: World Meteorological Organization, *public.wmo.int/en.*

List of figures

List of tables